Managing Wind Risk on Long Span Roofs

Dissertation

submitted to and approved by the

Faculty of Architecture, Civil Engineering and Environmental Sciences
University of Braunschweig - Institute of Technology

and the

Faculty of Engineering
University of Florence

in candidacy for the degree of a

Doktor-Ingenieur (Dr.-Ing.) /
Dottore di Ricerca in "Riduzione del Rischio da Catastrofi Naturali su Strutture ed Infrastrutture" *)

by

Giuseppe Olivato
born 10 November 1981
from Selvazzano Dentro (PD), Italy

Submitted on	18 March 2010
Oral examination on	06 May 2010
Professorial advisors	Prof. A. Saetta
	Prof. D. Dinkler

2010

*) Either the German or the Italian form of the title may be used.

“The man who can smile when things go wrong
has thought of someone he can blame it on”
Jones' law

Risk transfer on the Murphy's Law

ABSTRACT

A number of modern structures characterized by a relevant impact and elegance often coupled with lightness and irregular shapes are dramatically exposed to the wind aerodynamic action, which becomes a key factor in their safety assessment. These structures are involved into a global and complex design process in which players like the environment and social sciences join engineering in order to guarantee an optimal result under several aspects, not the last the economical aspect. In this background, it is not possible trusting into unreliable deterministic considerations, where the over-engineering would assure the result. The attention is now shifted to overall frameworks of Performance-Based Design aimed to specific performance targets and their optimization. In particular, the criteria to ensure the achievement of the results are expressed in terms of risk of failure.

This work of thesis presents a general framework for calculating all the possible structural damages and subsequently economic losses after a natural catastrophic event. The framework is adjusted and applied to the specific case study of the covering of the Stadium of Braga in Portugal, where the hazard of a windstorm, the loads that the latter enforces on the covering, the structural response, the resulting damages and other consequences are hierarchically calculated. Particular emphasis, and original contribution of the work, is paid on the evaluation of the dynamic response of the structure. Pressure fluctuations on buildings produced by storms have a complex temporal and spatial organization and their study, keeping under control the whole physical phenomena, is quite difficult. Accordingly, some suitable tools like the orthogonal decomposition are adopted in order to handle the huge amount of data. Moreover a consistent and operative procedure aimed at enhancing the assessment of the aerodynamic wind pressure on the covering is provided.

This work addresses a fundamental topic for the risk assessment; the results achieved by the duly application of the framework can be successfully transferred to other actors involved in the management and the governmental processes devoted to natural hazards.

ACKNOWLEDGMENTS

In a very funny comic strip on graduate students, a brave girl ventures on a perilous journey looking for the legendary *lost dissertation*, just to find out that it was only a white parchment paper. Suddenly the voice of her advisor explains her that the treasure she was looking for lies not into the dissertation but in the journey itself.

During the last three years I have focussed all my energies on the drawing up of this study, but only now that I have finished and I am going to write these words, I recognize myself in completely agreement with the comics. I have spent a lot of time and a lot of efforts to reach this goal and now I realize what I have really gained during my journey: the great many people who have helped me, who have worked with me, who have simply talked to me, all of them have left something I will bring with me independently from my research, from the dissertation.

For this precious treasure I found, I would like to thank my two tutors, Prof. Anna Saetta and Prof. Dieter Dinkler; they supervised my work and supported me during these years of academic research. I owe my thanks to Dr. Lazzari and Dr. Pontow, with whom I shared stimulating and profitable discussions on the field of wind engineering and finite elements. I would also like to express my sincere gratitude to the two coordinators of the Doctoral School, Prof. Borri and Prof. Peil, as they give me the opportunity to live this enriching experience within the international doctoral course.

Now the list starts growing fast because all my colleagues and friends, all the people from whom I had the opportunity to learn a lot, both form scientific and personal point of view, all the people that have shared experiences with me in these three years are integral part of my treasure and I beg all of them to feel included in my huge thank I devote to them. Thank you.

CONTENTS

LIST OF FIGURES

LIST OF TABLES

CHAPTER 1

RISK ASSESSMENT FRAMEWORK

1.1 INTRODUCTION

During the last decade, we have witness an increasing societal concern on sustainable development, focused on the conservation of the environment, the welfare and safety of the individual and the optimal allocation of natural and economical resources (Faber and Stewart 2003). The strategic action plans and the related policies developed by EU, USA and Japanese governments are based on a policy aimed to support Research-Technologic & Developments for the Sustainable improving of the performances and enhancing the quality of researches and application, not only in emerging sectors like renewable energy and CLIMTECH (Korhonen, Savolainen and Ohlstrom 2004), but also in maturing area like structural engineering and ICT as well.

The adjective *sustainable* assumes a wide meaning, due to the many aspects it can be applied to. Firstly, the impact on the environment in short and long time courses. Secondly, the implications in the improving of the life quality of the human individual, in a long list of issues, like the implementation of its performance and health, its life style and economic environment with a safe and responsible approach.

This tough problem may easily be realized to be a complex decision problem highly influenced by the possible consequences of our actions and the probabilities that these consequences will occur, the product of which is known as *risk*.

Every innovative process or, in a more general view, every new input gives back a certain degree of risk in contrast to the expected benefits. It is not always possible to predict them with a considerable advance. Even the delay in reaching some benefit results could be unpredictable and could bring negative consequences. However taking into account

the existence of risks becomes an intrinsic issue in each action a policy maker, a researcher, an engineer, a taxi driver etc. have to deal with.

In daily conversation *risk* is a rather common notion used interchangeably with words like *chance*, *likelihood* and *probability* to indicate an uncertainty about the state of activity, item or issue under discussion (Faber 2007). For example talks are made about the risk of getting cancer due to cigarette smoking, the chance of succeeding in developing a vaccine against the HIV virus, likelihood of getting a "Royal Flush" in a Poker game and the probability of a major earthquake occurring in Italy within the next decade, behind the recent events or the risk of another economic crisis.

Even though it may be understandable from the context of discussion what is meant by the different words, in engineering decision making risk has to be specifically addressed and understood as the expected consequences of an event associated with a given activity, e.g. the construction, operation and decommissioning of a power plant.

Considering an activity with only one event with potential consequences C, the risk R is the probability P that this event will occur multiplied with the consequences given the event occurs i.e.:

$$\mathrm{R} = P \times C \tag{1.1}$$

If n events with consequences C_i and occurrence probabilities P_i may result from the activity, the total risk associated with the activity is simply assessed through the sum of the risks from the individual events:

$$\mathrm{R} = \sum_{i=1}^{n} P_i \times C_i \tag{1.2}$$

This definition of risk is consistent with the interpretation of risk used in the insurance industry and from the socio-economic and socio-politic points of view.

Risk may be given in a *currency*, or in amount of *human fatalities*. Most of the risk values could be converted into the amount of money to be spent to recover a failure or to reach a result in delay. Unwanted events, as well, such as an environmental or human health impact, can be expressed by an amount of resources that need to be allocated to recover the environmental damage, or to heal the people involved. The value of a risk is the starting point to develop a strategy for managing.

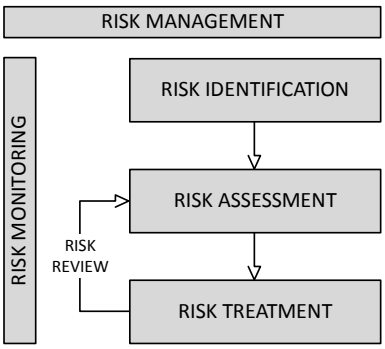

Figure 1.1: The general risk management framework (Pliefke, Sperbeck, et al. 2007).

According to (Pliefke, Sperbeck, et al. 2007), the risk assessment may be structured in main areas as depicted in Figure 1.1. Firstly, the research where a model to identify the risk is developed; secondly, the calculation of a risk considering specific assumptions and, eventually, the risk treatment. The latter is the part with the strongest impact on the society and could be divided in: risk communication; risk remediation and risk recovery. A relevant aspect is the study of the risk perception due to an action. The perception of people of an input could be very different among them and has to be considered.

Risk assessment and the related risk management process can be established with a definite degree of acceptance. How decisions are taken and the general precautions for a given risk influence the way the society deals with any event of the everyday life.

1.2 NATURAL DISASTERS

Today, the world is facing disasters and other humanitarian emergencies on an unprecedented scale. These include natural and human-made disasters, such as earthquakes, windstorms, transport and industrial accidents; longer-term disasters, such as famines and droughts; and situations creating mass displacement of people such as civil strife and conflicts.

According to (CRED 2004), more than 9'000 *natural disasters* have been registered since 1900. Of these, about 80% have occurred over the last 30 years. More than 255 million people were affected by natural disasters globally each year, on average, between 1994 and 2003, ranging from of 68 million to 618 million. During the same period, these disasters claimed an average of 58'000 lives annually, with a range of 10'000 to 123'000. During the last decade disasters caused damage of an estimated US$ 67 billion per year on aver-

age, with a maximum of US$ 230 billion and a minimum of US$ 28 billion. The economic cost associated with natural disasters has increased 14-fold since the 1950s.

The human and economic losses caused by natural disasters in 2008 were devastating. More than 235'000 people were killed, 214 million people were affected and economic costs were over US$ 190 billion. The CRED's Emergency Database (EM-DAT) recorded 354 natural disasters in 2008, which is less than the 2000-2007 yearly average number of 397. However, the death toll was three times higher than the annual average of 66’813 for 2000-2007, mainly caused by two major events: cyclone Nargis which killed 138'366 people in Myanmar and the Sichuan earthquake in China which caused the deaths of 87'476 people. Disaster costs in 2008 were more than twice the US$ 82 billion annual average for 2000-2007 and were mainly attributed to the Sichuan earthquake in China (US$ 85 billion) and hurricane Ike in the U.S. (US$ 30 billion).

Scientific predictions and evidence indicates that global climate change will increase the number of extreme events, creating more frequent and intensified natural hazards such as floods and *windstorms*. Population growth, urbanization and the inability of poor populations to escape from the vicious cycle of poverty contribute to an increase in the number of people who are vulnerable to natural hazards, with a resulting increase of natural disasters and environmental emergencies.

In the past, the major fraction of disaster management funding was generally assigned to disaster relief, instead of reduction or prevention. Calculations of *risks* and *vulnerability assessments* were a lower priority than response. With the increase in magnitude of disaster impacts, especially in the last decades, concern is mounting over inadequate awareness and prevention. It has become increasingly apparent that a relatively small investment in disaster preparedness can save lives, reduce the number of people requiring emergency assistance and preserve vital economic assets, as well as reducing the cost of overall relief assistance to disaster-stricken countries. Nowadays, most decision makers agree that the integration of disaster preparedness, *mitigation* and *prevention* measures into policy development is fundamental to reducing the vulnerability of human populations to natural hazards.

In accordance with CRED terminology, a disaster is:

> *“A situation or event which overwhelms local capacity, necessitating a request to the national or international level for external assistance, or is recognized as such by a multilateral agency or by at least two sources, such as national, regional or international assistance groups and the media”.*

The classification of disasters is a controversial and complex issue. A specific event can be catastrophic for an individual, but not for the community or for the society at large. In addition, categorizations also depend on whether economic impact, mortality or the geographic scope is considered as the determining factor.

In EM-DAT four main natural disaster types and their related disasters are considered, namely *floods*, *droughts*, *windstorms* and *geological disasters*. Floods and related disasters include floods (84%), landslides and mudflows (13%) and avalanches (3%). Windstorms include storms (31%), typhoons (20%), cyclones (16%), hurricanes (13%), winter storms (9%), tornadoes (7%) and tropical storms (4%). Geological disasters include earthquakes (83%), volcanic eruptions (16%) and tidal waves (1%). Droughts and related disasters include droughts (58%), extreme temperatures (21%) and wildfires (21%).

1.2.1 Windstorms

Windstorms are among the most destructive disasters. They often cover very wide areas and can cause significant deaths, injuries, agricultural or property loss.

Over the 1974-2003 period, a total of 1'864 windstorms caused the death of 294'000 individuals and affected[1] more than 557 million. The ratio of affected to killed was of 1'899, significantly less than for floods but over 10 times more than for earthquakes or volcanoes.

The most lethal windstorm of the last 30 years was in Bangladesh in 1991 with about 140'000 people killed (Jonkman 2005). On average, each windstorm affected close to 300'000 people, although a windstorm in China in 2002 affected 100 million (Stoltman, Lidstone and Dechano 2008).

In many cases, flooding from heavy rains and wind surges has a greater impact on mortality than that of the wind itself. However, collapsing buildings and wind-strewn debris can account for many of the injuries experienced during windstorms.

As shown in Table 1.1, richer countries tend to rank frequently in a listing of the most expensive disasters, because of higher insured values of property linked to higher labour costs for reconstruction. On the contrary, when expressing the losses by disaster category as a proportion of the previous year's GDP, the top ranking countries are all developing

[1] People requiring immediate assistance during a period of emergency; it can also include displaced or evacuated people.

nations and no industrialized country figures in the top 10 of any disaster category. In this respect, windstorms represent the disaster category with the highest relative costs.

Table 1.1: Top 10 most expensive wind-induced disaster: 1974-2003 (CRED 2004)

Windstorm		Year	2003 US$ billion
United States	Hurricane Andrew	1992	39.43
France	Winter storm	1999	12.24
United States	Tornado	1995	12.10
Japan	Typhoon Mireille	1991	7.04
Korea, DPR	Typhoon Prapiroon	2000	6.58
United States	Hurricane Iniki	1992	6.57
Western Europe		1990	6.49
United States	Hurricane Frederic	1979	5.84
Caribbean	Hurricane Hugo	1989	5.32
United States	Hurricane Isabel	2003	5.00
Western Europe	Hurricane Vivian	1990	4.51
Germany	Capella Gale	1976	4.21

An overview of the worldwide number of wind-induced disasters in the period 1976 – 2005 and the related number of victims is shown in Figure 1.2 and Figure 1.3 respectively. The most affected regions are northern America, eastern Asia, western Europe and Australia.

1.3 RISK FRAMEWORK

1.3.1 Catastrophe modelling

Several researchers from all the countries in the world spend a lot of energy trying to model natural and manmade disasters on ways they can be managed. Catastrophe modelling is not embedded in one field or discipline. The science of assessing and managing catastrophe risk originates from the field of property insurance and the science of natural hazards. Initially, tracking the events on a map in order to indicate their concentration of exposure, nowadays with Geographic Information Systems (GIS) software.

In their risk management approach, Grossi and Kunreuther (2005) indentify four basic components of a catastrophe model, namely *hazard inventory vulnerability* and *loss* (Figure 1.4). According to this general framework, the first step is to characterize the natural hazard phenomena: for instance, a hurricane is mainly characterized by its projected path and wind speed. The physical quantity needs also to be related with the frequency of certain value or frequencies of events.

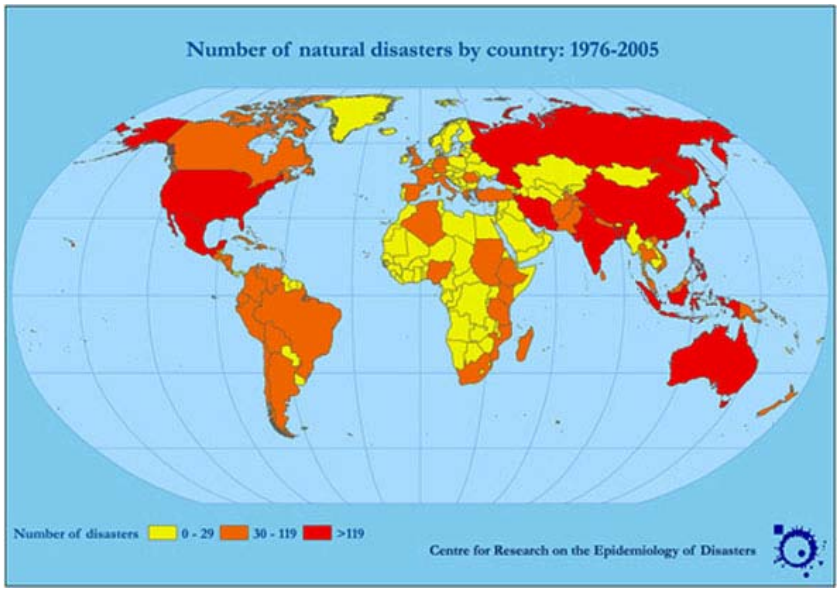

Figure 1.2: Number of occurrences of windstorm disasters: 1976-2005 (EM-DAT).

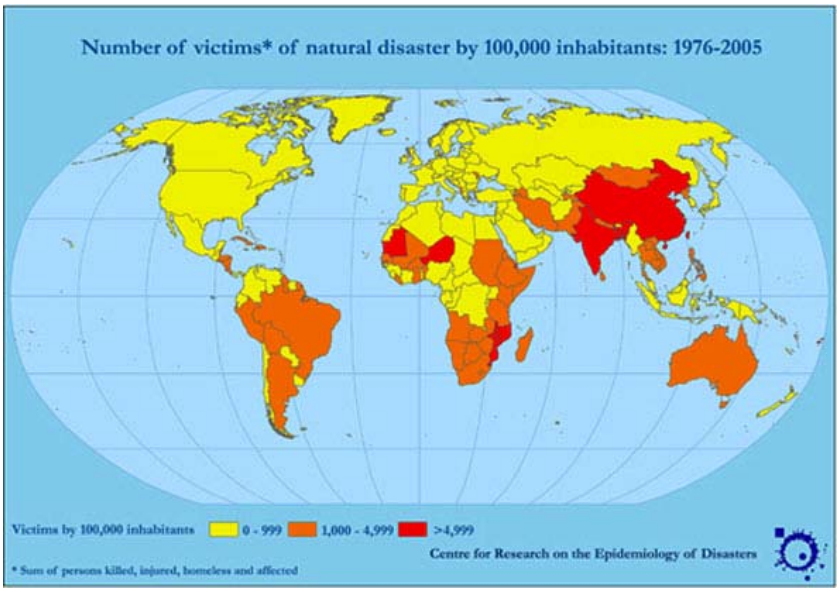

Figure 1.3: Number of victims of windstorm and related disasters per 100'000 inhabitants: 1976-2005 (EM-DAT).

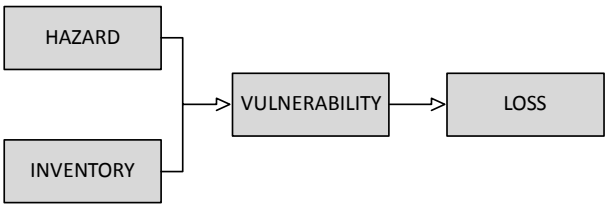

Figure 1.4: Catastrophe model (Grossi and Kunreuther 2005)

Next, the model requires to collect data in the inventory or portfolio of *elements at risk*[2] (EaR) as accurately as possible. One of the most important parameters used to characterize the inventory is the location of each element at risk. In addition to the element's location, all the other factors that could help in estimating the vulnerability should be included. For a building, these parameters include its construction type, its age, the number of stories, etc.

The hazard and inventory modules enable the calculation of the vulnerability or *susceptibility of damage* of the elements at risk. Practically, this step quantifies the physical impact of the natural hazard phenomenon on the system. The vulnerability quantification is the key factor of a catastrophe model. Some models use damage curves and relate structural damage to a severity parameter, such as peak gust wind speed or spectral acceleration. Others allocate the buildings into damage-state brackets, for example slight, moderate, extensive or complete damage.

The last step is the evaluation of losses based on the measure of vulnerability. In Risk Management it is used to refer to losses as *direct*, that can be directly related to the disaster, and *indirect*, which occur with a time shift. Indirect losses, or consequences, can be interpreted as the cost of missing in functionality of an EaR after the disaster has occurred.

Furthermore, the losses are classified into economic, humanitarian, ecological and CSH (cultural, social, historical) consequences. As it is possible to assign a monetary value only to economic consequences in a direct way, they will be referred to as tangible. All other classes of consequences are termed intangible (Pliefke, Sperbeck and Urban 2006).

1.3.2 Decision process criteria

Given the assumption that every *action* implies determined *consequences*, this thesis will focus its attention on a particular action as a *catastrophe*, whose consequences would in-

[2] A single or a group of persons or objects within the predefined System that are susceptible and exposed to the impact of a Hazard.

deed be *losses*. When considering such an issue, the need is to foresee and limit the entity of the losses.

Figure 1.4 presents a catastrophe model, where 4 key points are issued in loss management. Briefly, in the hazard component physical characteristics of the catastrophe are considered, in terms of intensity and return period. The inventory considers how and when the catastrophe acts on the system[3]; when the system is formed by a single EaR, the inventory is replaced by the hazard path. The last two milestones are the vulnerability and the consequent final losses.

The vulnerability is certainly the key point in the model. Even though vulnerability is not a quantifiable physical value, in Figure 1.4 it is considered at the same level of other terms, which on the contrary are identifiable as numerical values. Vulnerability can be also referred to as susceptibility to damage. When using this alternative definition, it becomes clearer the meaning of the vulnerability: the underlying physical value is the damage, while the susceptibility indicates the probabilistic value of its happening.

A simplified model of the risk framework can be shown as a chain whose starting and ending rings are, respectively:

CATASTROPHE → LOSSES

The Catastrophe is the specific event, with the intensity it has had in the past, e.g. the earthquake in Kobe, the Hurricane Katrina; to foresee future scenarios, it is necessary to collect information on the probability that a new catastrophe with the same intensity to happen again. The term Catastrophe is replaced by Hazard, which, in its definition, includes the hazard type (earthquake, flood, …), the intensity, the foreseen return period. The Losses, on the other end of the chain, are tangible, intangible, direct and indirect consequences due to the catastrophe.

The central rings of the chain specify the most significant values determining the final losses. Damage has already been cited, but other values can be explained in details: in the forthcoming sections, the loads acting on the structure/system, as well as its structural response.

[3] The object of investigation for which all sources of Hazard are identified and Risk Analysis is being performed. The System can be composed by a single building or infrastructure element, a suburb of a city, a whole urban region or even an entire country.

Terms such “susceptibility”, “vulnerability”, and “robustness”, which confer a probabilistic uncertainty[4] to the final result, need a dedicated consideration. In the risk schematization as “chain”, these terms define the relative mobility of the rings. When a deterministic relation binds two different values, the rings can be considered as welded, while if the relationship includes an uncertainty, the rings can show a relative sliding. In this case, the final configuration of the chain would be defined with a degree of probability, without an absolute certainty.

From this point of view, the model proposed by Grossi and Kunreuther (Figure 1.4), and applied to a single building, can be schematized with just two rings, Hazard and Loss, whilst the relative variability is defined only by the Vulnerability[5] of the system. Such a simplified model is at least as precise and reliable as more complex models, the missing information are related to the causes of the vulnerability, and how should it be calculated, issues that are left to the arbitrariness of the operator.

If the complete definition of risk on a given system is to be followed (1.2), an operator shall evaluate all the potential dangerous events, even with the lowest probability, and consider the potential damage. For instance, estimating the potential damages on a car travelling from home to the supermarket, both the risk of being hit by a pebble, or by a meteorite, should be considered. This approach can be valid in theoretical academic calculations, while in the common practice, a reasonable approach is to fix thresholds for very low probable events, and for very low harmful as well.

This approach, which seems perfectly reasonable, can be addressed as the major cause of the problems when calculating the risk. Even applying a scientific and “exact” method, indeed, there are still arbitrary and subjective decisions to be taken on how this “low” should be, or on what to be considered negligible.

Another key point to be taken into account, and that can be easily criticized, is the isolation of a system attacked by different catastrophic events. Isolating a system excludes indeed the effects on the calculation from the “rest of the world”, whose influence is considered negligible. Considering all the potential catastrophic events independently implies ignoring the possibility of different events to happen at the same instant. Of course, both these assumptions are incorrect. An easy solution is to extend the limits of the case study, and to include the combined probabilities of different catastrophes. Even though a theoretical mathematical model have been developed, its practical application is far to be the easiest choice.

[4] A potential deficiency in any phase or activity of the modeling process that is due to the lack of knowledge.
[5] Indicates the total potential of a Hazard of a given intensity.

A key choice for the decision maker is to define a specific objective, to apply the simplest mathematical model in accordance with the available data, and to control the reliability of the results.

1.3.3

Proposed risk assessment chain

To calculate in details and accuracy the risk of a catastrophic event, it is necessary to define precisely a system, namely a detailed case study, and progressively defining the most accurate rings of the chain, with their interdependencies.

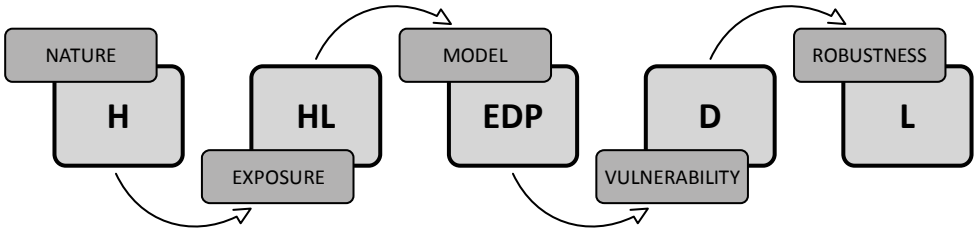

Figure 1.5: Proposed risk chain.

Focusing the attention on severe meteorological events, we can identify *the Nature* as the promoter of catastrophic events, and thus rely on meteorology for Hazard (H) identification on the system.

The second step is to understand how the harmful event may act on the system, or in other terms, which is the exposure of the system in respect of the event. The physical size to determine is the load (forces, pressures, accelerations) generated by the event, defined as Hazard Load (HL). As defined by Grossi et al (2005), in simplified contexts the Hazard Load can be determined starting from the Exposure, whilst in complex systems it is necessary to consider the Inventory. In other works, with different purposes and considering other aspects, the terminology can differ. In the present work, the “exposure” is defined as the pathway followed by the catastrophic event when reaching the system. Hence, a possible solution to reduce the risk of natural catastrophes is to add an obstacle, or a barrier, in the expected pathway. If such a barrier is applied as a modification of the given system, in the risk calculation the Hazard remains unchanged, while the Hazard Load varies, with a consequent change of the effects on the structure. If the barrier is outside of the system, as a different scenario, the exposure remains unchanged, whilst the reduction is applied as a reduction of the Hazard Intensity entering the system.

Once defined the loads applied to the structure, the second step is to calculate the structural response to the event under examination. Following PEER, the structural response is defined as *engineering demand parameter* (EDP). Several methods are available to calculate the structural response, each with different advantages and precision levels: numerical models, physical scale models, non destructive tests on the existing structures. Nowadays, the gold standard, or at least the starting and support method, is the preparation of a numerical model (FEM for civil structures) which reproduces in details the structure and the binding conditions. This model would serve as a base on which to apply the load condition of the event under examination.

The connection between the chain rings HL → EDP is here reported as the numerical model FEM, which is described in details in chapter 4. FEM models, normally, do not support any uncertainty in the results: starting from the initial data, an unambiguous result is achieved, following a deterministic relationship. Probabilistic numerical models are available as well, but their complexity is normally extremely high even with a limited number of parameters.

After the structural response, the next step is the calculation of the structural damage. The evaluation of Damage (D) is a crucial step in risk assessment, as it quantifies the physical effect of the catastrophic event, in terms commonly understood from people without a decidedly engineering training. While the EPD gives technical information as stress-resultants, displacements, vibrations, the damage gives a more tangible and comprehensive information, normally expressed with a scale of percentages: 0% no damage; 100% totally destroyed.

In the risk chain, the step between EDP and D contains some levels of uncertainty, and it is suggested to the operator to express this parameter in damage-stage brackets, as: slight, moderate, extensive, or complete damage. In this point of the procedure, the term “vulnerability”, as proposed by Grossi et al (2005), is considered. The term here is meant as susceptibility to the damage, and can be considered starting from technical and detailed information, first of all the structural response.

The last ring of the chain is the calculation of the robustness of a system, related as the ability of a considered system to sustain a given damage state subject to the prevailing exposure conditions, and thereby limit the consequences of exposure events to the direct consequences (Faber 2007).

Robustness is meant in generic terms, namely the system’s reaction to the given damage. It is possible, then, to evaluate direct and indirect losses (L), and it becomes easier to facilitate the post-catastrophe period.

1.3.4

Computation of risk

In several situations, in the common life, probability is evaluated according the frequency probability definition, tallying the number times the event occurs divided by the number of experiments that is carried out. This approach is normally used in quality tests in the industry. When considering larger scales, e.g. when studying buildings, infrastructures, dams, in engineering, but also when characterizing the financial situations of different countries, of migrations, in economy and social sciences, it is impossible to statistically estimate the probability of a given event. A statistically significant number of comparable events is indeed lacking. Modern structural reliability and risk analysis are based on the Bayesian interpretation of probability, where the lack of knowledge is treated by probabilistic reasoning like other type of uncertainties.

Applying the theorem of total probability and the Bayesian theory (see Appendix A), when assigning the conditional probabilities of the single events, it becomes possible to calculate the risk for the system as the sum of all possible loss levels, multiplied by their probability to happen.

$$\mathrm{R} = \sum_i \mathrm{L}_i \cdot P(\mathrm{L}_i) \tag{1.3}$$

Covering the risk chain (Figure 1.5) in the opposite direction, from right to left, it is further possible to write the probability of a loss level $P(L_i)$ after the determination of all the conditional probabilities $P(\cdot \mid \cdot)$ of the several chain rings, expliciting the mobility relationships yet hinted, multiplied by the probability of the hazard at the beginning of the chain.

$$P(\mathrm{L}_i) = \sum_j P\big(\mathrm{L}_i \cap \mathrm{D}_j\big) = \sum_j P\big(\mathrm{L}_i|\mathrm{D}_j\big) \cdot P\big(\mathrm{D}_j\big) \tag{1.4}$$

$$P\big(\mathrm{D}_j\big) = \sum_k P\big(\mathrm{D}_j \cap \mathrm{EDP}_k\big) = \sum_k P\big(\mathrm{D}_j|\mathrm{EDP}_k\big) \cdot P(\mathrm{EDP}_k) \tag{1.5}$$

$$P(\mathrm{EDP}_k) = \sum_m P(\mathrm{EDP}_k \cap \mathrm{HL}_m) = \sum_m P(\mathrm{EDP}_k|\mathrm{HL}_m) \cdot P(\mathrm{HL}_m) \tag{1.6}$$

$$P(\mathrm{HL}_m) = \sum_n P(\mathrm{HL}_m \cap \mathrm{H}_n) = \sum_n P(\mathrm{HL}_m|\mathrm{H}_n) \cdot P(\mathrm{H}_n) \tag{1.7}$$

Substituting (1.4)-(1.7) in (1.3), it is possible to obtain the complete formula for the calculation of the risk due to natural catastrophes in continuous terms:

$$\mathrm{R} = \int \mathrm{L} \cdot f(\mathrm{L}|\mathrm{D})\, f(\mathrm{D}|\mathrm{EDP})\, f(\mathrm{EDP}|\mathrm{HL})\, f(\mathrm{HL}|\mathrm{H})\, d\mathrm{H}\, d\mathrm{HL}\, d\mathrm{EDP}\, d\mathrm{D}\, d\mathrm{L} \tag{1.8}$$

Equation (1.8) is the integral formula of the risk, where all the conditional probabilities $P(\cdot \mid \cdot)$ have been substituted with the conditional probability density function $f(\cdot \mid \cdot)$. The formula, as here reported, with a multiple integral with the same number of values of the number of the chain rings, has been firstly reported by PEER, in the study of earthquakes' effects (Baker and Cornell 2003), but due to its general nature can be applied in other different fields (Paulotto, Ciampoli and Augusti 2004).

CHAPTER 2

HAZARD ON THE STADIUM OF BRAGA

In this chapter a specific case study of a building usually subjected to windstorm events is presented. This building is the municipal football stadium of the city of Braga in Portugal, renowned all over the world for its extraordinary suspension covering that is extremely flexible and interesting in this context because it is easily stressed by the dynamic effects of the wind action. These features, combined with the huge amount of data produced by several experimental tests yield the roof of the stadium as an excellent example for calculating the structural reliability through the application of the Risk Management Chain defined in chapter 1. All the ring chains of Figure 1.5 and their solution are described in this and in the following chapters.

As a first step the definition of the system is required. Here below the detailed geometrical and mechanical characteristics of the stadium are exposed highlighting the adopted technology during the construction process of the roof. Moreover, two experimental set of tests are presented and widely explained; the tests aim to characterize the effective dynamic properties of the built-up covering. Tests results offer the comparison checkpoint applied to validate the numerical models created and used within the present work (see chapter 4).

The last part of the chapter provides an extensively explanation of the real wind phenomena that affect the stadium of Braga. Merging together real data collected on-site with the results of a topographic scale model of the whole suburban area around the building, and conforming the outcomes to the same security level of the codes in force, it is possible to create a global wind speed profile variable with the point height and the wind direction. The *wind speeds* of the previous profile are considered the *hazard intensity* of events characterized by a return period of 100 years. All other events with different occurrence degrees are considered by using statistical relations and they are related to their *exceedance annual probability* (EAP) that will be named as *hazard probability*.

2.1 STADIUM DESCRIPTION

The Braga Municipal Stadium is located in Dume, the northern suburb of the city. It lays as in an amphitheatre inside the granite quarry of Monte Castro with a marvellous view on the city. The architect Eduardo Souto Moura imagined the complex made up with only two grandstands on both sides of the football pitch, one hollowed out in the rock (west stand), the other would rise up from the ground as the eastern space ending. Behind the goals nothing has to hide the quarry (south side) and the sight of Dume on the north side.

(a) (b)

(c) (d)

Figure 2.1: General views of the Stadium of Braga: a) panoramic view; b) excavation; c) Dume city's view; d) east grandstand.

The entire complex has been built for the Euro Football Championship in 2004 and it includes, besides the Stadium, a sports pavilion and an Olympic swimming pool. Builders' purpose was to create a stadium big enough for hosting 30.000 spectators but, at the same time, that must be as simpler and cleaner as possible in the way to merge everything inside the hill. To reach this aim the whole area of the pitch acts itself as a building with

two floors that include all the back services, the changing rooms and a parking garage. The rock excavation was one of the bigger problem come up against the engineers: in total 1.7 million of $m^3$of hard rock and gravel were excavated. But with any doubts the major challenge for the design team was the stadium's roof, identified as the most noticeable element in the whole complex.

To achieve the final design for the roof several hypothesis were be proposed (Furtado, Quinaz and Bastos 2005). Initially the idea was to build a continuous canopy-style roof inspired by ancient South American Inca bridges, with dozens of steel strings flying across the pitch. Afterwards this solution was modified due to illumination problem for the grass: the slab was divided in two pieces clamped directly to the stands and the stripes have been replaced by couples of full locked coil cables. The current construction holds 34 couples of cables which cover the total span of $202\ m$ anchored to the tops of the grandstands; over the wires there are two concrete slabs ($126 \times 57\ m$ each) with two transversal triangular trusses suspended from the inner border of each slab acting as a stiffness girder and also accommodating the floodlights and the loud speakers.

2.1.1

Construction process

The roof (Afassociados 2001) is sustained by a set of pairs of full locked coil cables at $0.30\ m$ distance with a centre axis spaced at $3.75\ m$. The cables are engaged for $5\ m$ inside the concrete beams at the top of the grandstands and anchored (Figure 2.2b). This configuration provides a sliding support on every two cables for each slab panel (Figure 2.2a). The cables are made by hot dip galvanized high strength steel wires built by an inner core made by round wires and by one or more external layers of Z shaped wires. The Z shape of the wires is specially made in order to have a self-locking of the wires, obtaining a compact section. The main properties of the cables, taken from the producer database, are reported in Table 2.1.

Table 2.1: Mechanical properties of the cables.

tensile strength	$f_u = 1570\ MPa$
proof stress	$f_{0.2k} = 1180\ MPa$
Young's modulus	$E = 163\ GPa$
elongation at break	$\varepsilon = 4\%$ on $250\ mm$ gauge length
nominal strand diameter	$D_n = 88\ mm$
effective area	$A_{eff} = 5274\ mm^2$
minimum break load	$AF_{max} = 7720\ kN$
working load	$N = 3000 \div 3500\ kN$
weight	$W = 43.5\ kg/m$

Special manifolds joint the strands to the concrete slabs, they ensure free slipping in the cable's axial direction while the displacements in other directions are fixed. On the central span's part ($88\ m$) without any restraints with the slabs, several devices are placed in order to avoid aeroelastic effects (Figure 2.2c).

(a) (b)

(c) (d)

Figure 2.2: Construction phases: a) slab element position; b) cable anchor; c) devices against the aeroelastic effects; d) overhanging aqueduct.

The cladding is made by several composite panels with dimensions of $7.5 \times 2.4\ m$. Each piece is linked to the previous one through bolts and they make them sliding along the cables by gravity. Afterward, when all the elements are correctly positioned, after full application of dead load, the panels were sealed together with a concrete bonding material. Each panel is made by a one-way ribbed plate (steel grad S355 J0) filled by reinforced concrete (C30/37, $E_d^{conc} = 32.8\ GPa$). The panels' thickness is $24.5\ cm$.

The stiffener girders placed on the slabs' border line have the double role of increasing the stiffness of the roof in the across-cable direction and of supporting the technological devices (Figure 2.1c). The girders are formed by triangular trusses with the base putted on the top side and with a service platform sited on middle height. The girders are $3.5\ m$

height and $2.5\ m$ depth; they are built with rectangular hollow section (steel grad S355 J0) with different sizes:

- upper rods $RHS\ 150 \times 150 \times 8\ mm$
- lower rods $RHS\ 200 \times 200 \times 10\ mm$
- diagonals $RHS\ 100 \times 100 \times 6\ mm$

The roof shape is established by the 34 pairs of cables with total span of $212\ m$ divided in $5 + 5\ m$ of anchor inside the border girders, $57 + 57\ m$ as a support for the two slabs and the central span of $88\ m$ without any other connection or dead load. The correct configuration, that is the displacement distribution, is determined by the self weight of cables and concrete panels, which do not improve the stiffness without the sealing, and are depended by the actual cable initial length. This length is variable so the maximum displacement is around $7.5\ m$ on the north side and $1\ m$ more on the other side, to permit the drainage of rainwater in the embankment direction with one percent grade. Two large spouts in stainless steel are suspended from the concrete slabs channel the water to the overhanging aqueducts (Figure 2.2d).

2.2 DYNAMIC CHARACTERIZATION

The outstanding characteristics of the stadium's roof has required a wide and complete monitoring of every construction phase in order to ensure the validity of the static design and assumptions about the dynamic. The static monitoring system is based on a series of load cells fitted up in the cables anchorages to control the strain/stress situation on the roof, while strain gauges, tilt meters and thermometers were installed in the concrete structures; other devices were placed in order to control the rock massif and the foundations (load cell in the anchors to the ground and in-place inclinometers). On the inner edges of the two slabs 6 accelerometers and pressure cells were also installed to observe the response of the roof to the wind action.

2.2.1 Full scale tests

The Design Office Afassociados commissioned the dynamic tests on the built-up stadium to Prof. Majowiecki's team (Majowiecky, Marini and Cosentino 2004) who divided the experiments in two different exciting systems. Firstly an impulse load test was performed releasing an heavy mass linked to the truss beam of the roof (Figure 2.3a) and, starting

from the obtained results, the team succeeded into extrapolating information for a second set of tests. In this part the structure was excited by an approximately harmonic load provided by an electric engine which drove the covering into a resonance condition highlighting its modal shapes and the natural frequencies.

(a) (b)

Figure 2.3: Full scale dynamic test phases: a) impulsive test setting; b) accelerometers and exciting system position.

During the impulsive test the structure was excited by a point load, by releasing an approximately 5 tons mass preliminary suspended to the roof. The impulsive force had to be relatively small for safety reasons. Hence the relative structural response was not sufficiently wide and clear to be used for the modal shapes and damping identification. The main purpose of the test was to roughly identify the main natural frequencies of the structure in order to focus the harmonic load on these values. Once the main natural frequencies of the roof were identified, in the second test series the main natural vibration modes were significantly excited by mean of resonant harmonic forces. For this purpose, different excitation frequencies were tested, close to the preliminary identified ones, til the best fitting of the resonance frequency was reached for each mode.

During the resonance test there were six accelerometers as part of the structural monitoring system installed in the stadium (Figure 2.3b). They were Tri-axial Force Balance type, consisting in a mass-spring oscillator with optical mass pickoff sensing, working within a frequency range of 0 to $60\ Hz$. Only the vertical acceleration component has been taken into account. It is enough to describe the behaviour of the most flexible vibration modes, which are substantially the wind excited ones, the vertical component being prevailing for these modes. The accelerations on the 6 sensors were simultaneously acquired and recorded during the tests at $250\ Hz$ frequency sampling.

Results of both impulsive and resonance experimental tests can be found in (Cosentino and Majowiecki 2004).

2.2.2

Natural frequencies and vibration modes

Starting from the previous outcomes, a second set of experimental tests based on ambient wind excitation were provided by the team of Prof Caetano based on the extensively numerical analysis of the stadium during the design process (Caetano and Cunha 2001).

The identification of natural frequencies and vibration modes were based on an ambient vibration test in which three strong motion recorders (seismographs) were used. Figure 2.4 shows a plan of the instrumentation consisting on a total of 42 measurement locations where the accelerations with respect a reference station (mark 7: central points on the west slab) were recorded in succession. The test collected a $16\ min$ time series sampled at $100\ Hz$ at each location under the ambient excitation. In terms of recorded amplitude, peak accelerations of the order of $4\ mg$ with associated root mean square lower than $1\ mg$ were recorded, indicating a very low level of oscillation during measurements (Caetano, Cunha and Magalhães, Numerical and experimental studies of Braga sports stadium suspended roof 2008).

Table 2.2: Natural frequencies of the roof structure calculated at design, constructed and identified

Mode	Frequency (Hz)			Mode	Frequency (Hz)		
	Design	Con-structed	Identified		Design	Con-structed	Identified
1	0.303	0.277	0.275	8	0.672	0.678	0.702
2	0.322	0.305	0.293	9	0.691	0.712	0.737
3	0.455	0.520	0.525	10	0.693	0.754	
4	0.470	0.532	0.537	11	0.712	0.844	
5	0.476	0.574	0.562	12	0.748	0.923	
6	0.516	0.610	0.635	13	0.802	1.045	
7	0.660	0.673	0.653	14	0.864	1.063	

Average power and cross-power spectrum density functions between the recorded response at each location and the simultaneous response at the reference section were estimated for the set of measurements, with a frequency resolution of 0.0061 Hz. These estimates were used to identify natural frequencies and modal shapes, based wither on the conventional peak picking, or on the *Frequency Domain Decomposition* methods (FDD) (Brincker, Andersen and Moller 2000). The two identification methods provided similar estimates. Figure 2.5 shows the *Average Normalized Power Spectral Density* (ANPSD) function estimate based on the set of 42 measurements along the vertical direction (Ljung 1987). Columns 4 and 8 of Table 2.2 show the identified natural frequencies, and some of the corresponding identified modal shapes based on the FDD method are represented in Figure 2.6.

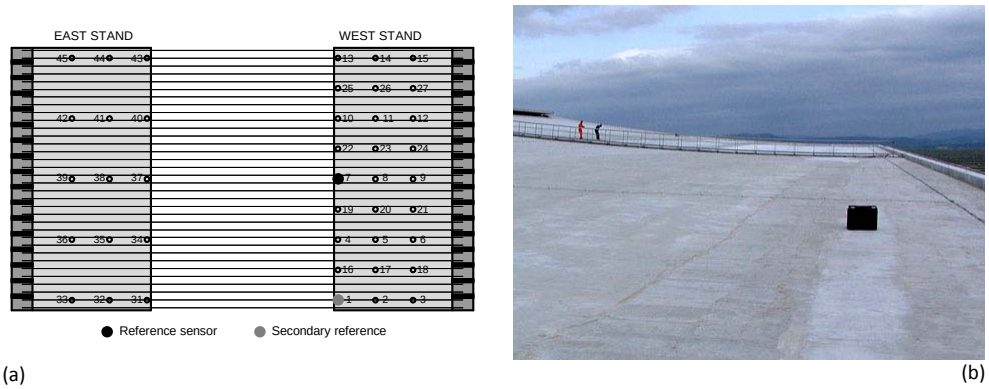

(a) (b)

Figure 2.4: Instrumentation plan for ambient vibration test: a) plan of locations; b) seismograph.

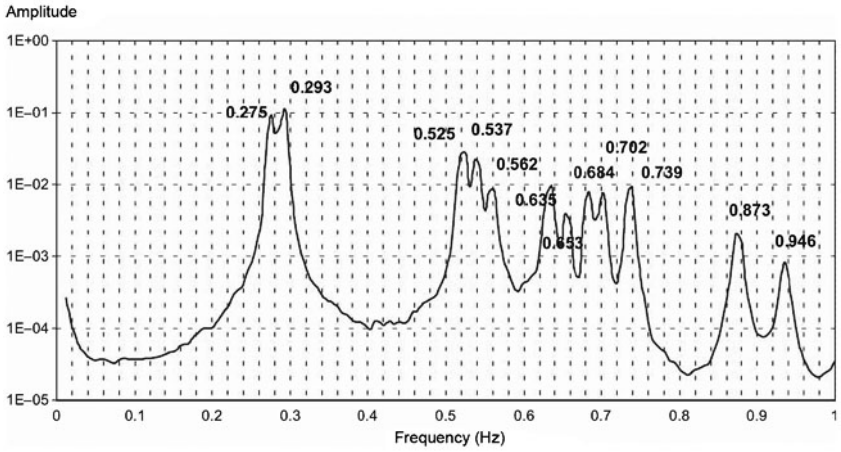

Figure 2.5: Average normalised power spectral density estimate for vertical direction (Caetano et al. 2008).

The results here presented (Magalhães, Caetano e Cunha 2006) were obtained in the Laboratory of Vibrations and Structural Monitoring of the Faculty of Engineering of the University of Porto (ViBest/FEUP Portugal). The staff performed the analysis with ARTeMIS Extractor Pro of the database created during the dynamic tests of the stadium's roof.

The analysis identifies the main frequencies of the structure and estimates the modal shape configurations. Figure 2.6 represents the configurations of the first 9 identified modal shapes. Due to the presence of the slope in the roof to drainage the rainwater, the structure is not perfectly symmetrical in relation to the middle axis parallel to the cables. This particular geometry justifies the existence of pairs of modes with close frequencies and almost symmetrical configurations.

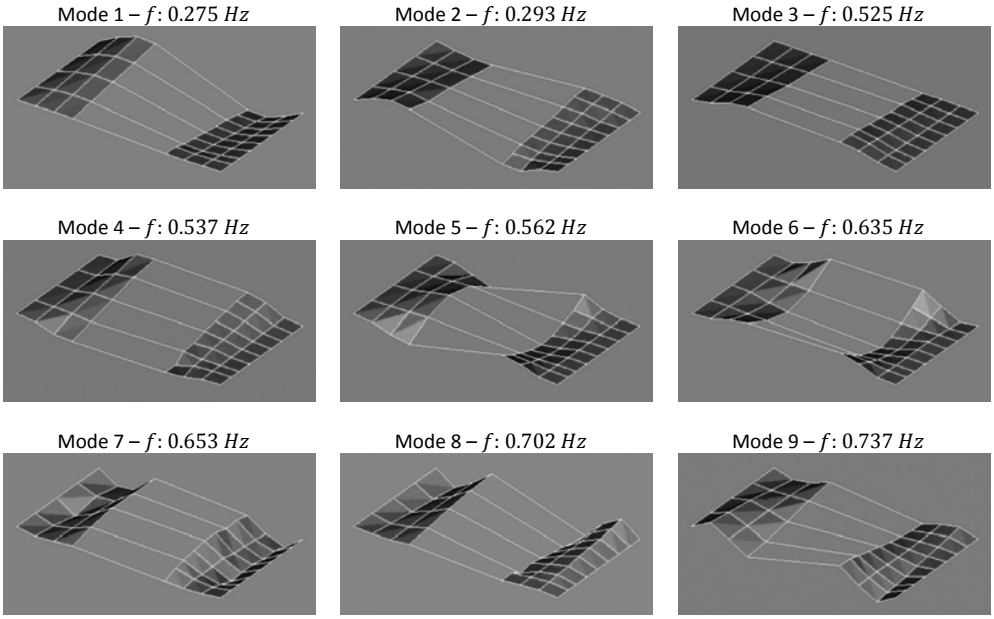

Figure 2.6: Identified modes based on the FDD method.

2.2.3

Modal damping ratios

The identification of modal damping ratios was developed as result of the preview three full scale tests on the structure. The results of those analyses are presented in the Table 2.3 (Magalhães, Caetano e Cunha 2006) (Caetano, Cunha and Magalhães, Numerical and experimental studies of Braga sports stadium suspended roof 2008). The damping extrapolations from the free vibration (impulse) test are reported in the second column. Given the small mass employed, relatively low levels of acceleration were measured, no greater than $15\ mg$, and the identification of damping ratios from the free decay associated with the first vibration modes was not possible using band pass filtering to isolate free vibration modal responses. The estimations achieved by the application of Stochastic Subspace Identification method SSI-COV (Peterson 2000) are also reported on the third column of this table. On the other side, the results obtained with the harmonic load test are sharper and more comprehensible. After that resonance was attained, the excitation was suppressed and the free vibration response was measured. The logarithmic decrement on the acceleration graphs determines the damping ratios reported on the fourth column.

Table 2.3: Identified modal damping coefficients (%)

Mode	Free Vibration		Harmonic	Ambient Vibration		
	Filter	SSI-COV	Filter	FDD	SSI-COV	SSI-DATA
1	–	0.29	0.28	0.58	0.50	0.51
2	–	0.37	0.27	0.52	0.42	0.48
3	0.28	0.32	0.22	0.47	0.44	0.39
4	0.25	0.22	–	–	0.40	0.33
5	–	0.44	–	–	0.47	0.53
6	0.34	0.36	0.43	0.35	0.54	0.47
7	–	0.29	–	–	0.28	0.73
8	–	0.11	0.20	–	0.27	0.30
9	–	0.18	–	–	0.26	0.32
10	0.20	0.18	–	0.25	0.26	0.29
11	–	–	–	0.36	0.41	0.38

Modal damping ratios were also identified on the series recorded under ambient excitation, by application of an enhanced version of the FDD method on the average power spectrum matrix formed from 12 records, 16 minute long, collected simultaneously at mark 1 and 7 of Figure 2.4a. The exponential fitting of the envelope of the autocorrelation function associated with the autopower spectrum extracted from the singular values follows. When the damping ratio is very small, very long time records are required. As a comparison, two different versions of the Stochastic Identification method were applied. All those results are summarized on the last three columns of Table 2.3.

It can be observed that the estimated modal damping based on ambient vibration tests are reasonably correlated with each other and they are, in general, of higher value than the corresponding estimates based on more conventional methods. This fact can be explained by the use of very long ambient vibration records that include particular periods in which the wind velocity was not negligible and which therefore added a part of aerodynamic damping.

2.3 WIND SPEED PROFILE

In order to determine the effects of the surrounding topography on the average speed and on the turbulence intensity arising from the airflow in the neighbourhood of the stadium, tests were undertaken in a wind tunnel on a *topographic* model in a scale 1:1500 (Figure 2.8) and on a rigid *aerodynamic* model in a scale 1:400. The collected data matching the meteorological information given by a nearby station have been approximated with a continuous function recreating the mean wind speed and the turbulence information in any point surrounding the stadium.

2.3.1

Meteorological data

A recent automatic meteorological station existed in Merelim, approximately $2.5\,km$ Northwest from the stadium location; however, at the date of the project, only two and a half years of data were available. To obtain a description of the design wind speed at the construction site for a 100-years return period, these few data were statistically processed and suitably corrected in order to align the maximum value to the codes prescriptions. The extreme value analysis of the anemometer data uses the Leiblen Method on independent gust velocities. The analysis for mode and dispersion was done on the square of the velocities as this provides a better fit to the Fisher Tippet type-1 distribution of extremes (RWDI, Wind tunnel study of a roof wind pressures, Braga Stadium 2001).

The Aeolian measures, reported in Table 2.4, are referred to 16 sectors each of them collecting data from a window of $22.5°$ from North in clockwise direction. The measured wind speeds are the average of 10 minutes sampling at $10\,m$ height starting from the ground level. The other columns explicit the adjustment to project the data into the appropriate design values, in particular the smoothing places a lower cut-off at 71% of the maximum value.

Table 2.4: Wind Speed (WS) information at anemometer site.

section	angle [° East]	dispersion	measured $[m/s]$	WS +15% $[m/s]$	adjusted $[m/s]$	smoothed $[m/s]$
1	0.0	5.8	19.1	21.9	27.3	28.8
2	22.5	6.0	18.7	21.5	26.8	28.8
3	45.0	5.5	17.4	20.0	24.9	28.8
4	67.5	5.6	17.5	20.1	25.1	28.8
5	90.0	6.5	19.4	22.3	27.8	28.8
6	112.5	7.0	21.0	24.1	30.0	30.0
7	135.0	7.7	23.3	26.8	33.4	33.4
8	157.5	8.7	26.5	30.5	38.0	38.0
9	180.0	8.3	27.8	32.0	39.0	39.9
10	202.5	9.6	28.3	32.5	40.6	40.6
11	225.0	9.1	27.5	31.6	39.4	40.2
12	247.5	8.8	26.7	30.7	38.3	38.3
13	270.0	8.0	24.4	28.1	35.0	35.0
14	292.5	8.8	21.9	25.2	31.4	31.4
15	315.0	8.1	20.1	23.1	28.8	28.8
16	337.5	8.9	19.5	22.4	28.0	28.8
all	360.0	8.4	26.7	30.7	38.2	38.2

On Figure 2.7 the measured, adjusted and smoothed wind speed record are shown in reference to the wind direction. The smoothed line (black dots) is now on considered as the measured gust wind speed at $10\,m$ height on the anemometer site. These values are used to calibrate the topographic scale model.

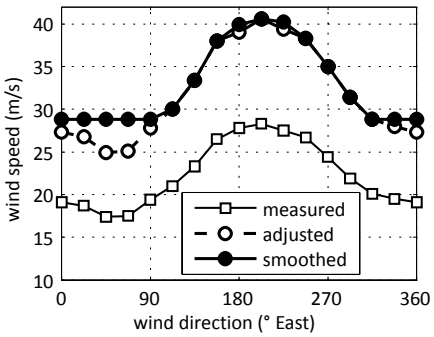

Figure 2.7: Wind speed measured at the meteorological station in Merelim.

2.3.2

Topographic model

All the collected information from the meteorological station, adjusted to comply with the standard in force (Eurocode_1-1-4 2005), were used as a reference in order to build a topographic model in a scale 1:1500 in RWDI laboratories in Canada. The model (Figure 2.8) reproduces the true terrain orography of the Stadium's neighbourhood for a radius of almost $3.6\ km$, including also the anemometer location.

(a) (b)

Figure 2.8: Topographic model: a) view of the model; b) satellite view of the area.

The main goals of the test are the determination of the gradient wind speed G and height δ that is the altitude over which there is no influence of the ground in the wind speed, and to give information of the wind speed profile in the stadium site.

As a first phase of the tests a set of sensors have been placed at different height in the anemometer site in order to compare and tune the results with the in-site measures. The founded *gradient height* is $\delta = 600\ m$ from the ground level, a quite high value but still

compatible with literature data (Dyrbye and Hansen 1996). Moreover, the *mean wind speed* $\overline{U}_{10}$ and the *turbulence intensity* I_u were also collected in the same place at $10\ m$ (true scale) height in 18 different directions: every 20°.

Table 2.5 shows the turbulence intensity as well as the ratio between the mean wind speed at the reference height ($10\ m$) and the gradient wind speed G.

Table 2.5: Anemometer height data – 1:1500 scale model.

section	angle [° East]	$\overline{U}_{10}/G$	I_u
1	20	0.55	0.16
2	40	0.48	0.21
3	60	0.49	0.20
4	80	0.53	0.20
5	100	0.55	0.17
6	120	0.55	0.18
7	140	0.51	0.20
8	160	0.49	0.20
9	180	0.49	0.20
10	200	0.46	0.17
11	220	0.55	0.14
12	240	0.50	0.19
13	260	0.50	0.18
14	280	0.47	0.21
15	300	0.46	0.19
16	320	0.47	0.21
17	340	0.47	0.22
18	360	0.57	0.19

In order to assist the alignment from the true wind speed profile and the simulated one, two simplifying assumptions have been made:

- the ratio between gust peak velocity at the reference height and the gradient wind speed is the same both in the model and the true scale;

$$\left(\frac{U_{10m}^{gust}}{G}\right)_{model} = \left(\frac{U_{10m}^{gust}}{G}\right)_{real} \tag{2.1}$$

- the turbulence intensities remain the same both in the model and the true scale.

$$(I_u)_{model} = (I_u)_{real} \tag{2.2}$$

Using these assumptions it is possible to calculate the gradient wind speed varying the angle where the wind blows from. All steps are reported in Table 2.6.

Table 2.6: Wind speed results from the topographic scale model.

section	angle [° East]	U_{10}^{gust} $[m/s]$	I_u	$\bar{U}_{10}$ $[m/s]$	$\bar{U}_{10}/G$	G $[m/s]$
1	20	28.8	0.16	18.5	0.55	33.6
2	40	28.8	0.21	16.6	0.48	34.6
3	60	28.8	0.20	16.9	0.49	34.6
4	80	28.8	0.20	16.9	0.53	32.0
5	100	29.3	0.17	18.4	0.55	33.5
6	120	31.2	0.18	19.1	0.55	34.7
7	140	34.4	0.20	20.2	0.51	39.7
8	160	38.2	0.20	22.5	0.49	45.9
9	180	39.9	0.20	23.5	0.49	47.9
10	200	40.5	0.17	25.4	0.46	55.2
11	220	40.3	0.14	27.0	0.55	49.2
12	240	38.9	0.19	23.4	0.50	46.8
13	260	36.5	0.18	22.4	0.50	44.7
14	280	33.4	0.21	19.3	0.47	41.0
15	300	30.5	0.19	18.3	0.46	39.9
16	320	28.8	0.21	16.6	0.47	35.3
17	340	28.8	0.22	16.3	0.47	34.6
18	360	28.8	0.19	17.3	0.57	30.3

Starting from the gust wind speed measured in-situ, the correct correlation between the different sections from Table 2.4 to Table 2.6 is obtained with linear interpolations. The mean velocities are computed by using the standard relation:

$$U^{gust} = \bar{U}(1 + g\, I_u) \tag{2.3}$$

where the turbulence indices have been measured in the scale model and the peak coefficient is $g = 3.5$. The last column reports the gradient wind speed as a simple division of the previous two columns.

The maximum found value is $55.2\ m/s$ when the wind blows from 200° East. This value is consistent with literature values, in particular (Simiu and Scanlan 1996), (Holmes 2001) propose the exponential equation:

$$\frac{\bar{U}(z_g)}{G} = \left(\frac{z_g}{\delta}\right)^{\alpha} \tag{2.4}$$

In the case of the Stadium of Braga, the reference height is $z_g = 10\ m$, to which it is possible to assign the mean wind speed $\bar{U}(z_g) = 25.0\ m/s$ according to the obtained values and the Portuguese and European Standards. The considered gradient height δ and the exponent α are written in Table 2.7 in the case of suburban terrain. The resultant values of

gradient wind speeds G are generic, based on studies in the United States; nevertheless they are suitable worldwide and they do not give any relation with the wind direction. These observations justify the great gap between the maximum and minimum value of G, but it is a big comfort that the values given from the *American National Standard* and from the *ASCE* are close to the obtained maximum and minimum values reported in Table 2.6.

Table 2.7: (Simiu and Scanlan 1996) table 2.2.2, suburban terrain.

(Davenport 1965)	$\alpha = 0.28$	$\delta = 400\,m$	$G = 70.2\,m/s$
(American National Standard A58.1 1982)	$\alpha = 0.22$	$\delta = 366\,m$	$G = 55.6\,m/s$
(ASCE 7-02 2002)	$\alpha = 0.14$	$\delta = 366\,m$	$G = 41.8\,m/s$

Concluding, the found peak wind gradient speed $G = 55.2\,m/s$ is considered reliable likewise the adopted procedure. Figure 2.9 shows the variation of that value changing the wind directions (*original*, dashed line); moreover a cut-off filter at $71\% \cdot G_{max}$ and a smoothing process have been also done following the same criteria used by OAP for the meteorological data (*adjusted*, continuous line).

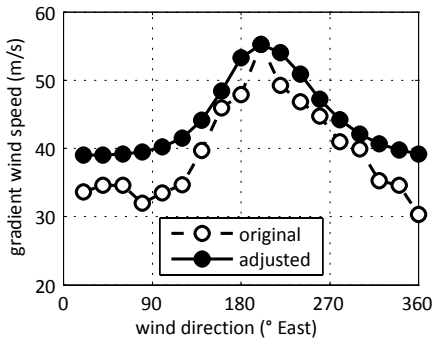

Figure 2.9: Gradient wind speed.

2.3.3

Characterization of the wind speed profile

The second goal of the wind tunnel tests is to find out some parameters in order to build the wind speed profile in the stadium location. To this aim, specific comparative tests have been made linking the *topographic scale model* (scale 1:1500) and a *aerodynamic scale model* (scale 1:400). In both the scale models, sensors gauge the wind speed in 18 different directions in four major heights: the reference height $10\,m$, the stadium's roof interval height $25 \div 50\,m$ and the gradient wind speed at $600\,m$. It should be borne in mind that the stadium itself was not inserted in the topographic scale model because at that time the project was not concluded yet. After a careful set-up, where the two models' output

have been aligned under the assumption that considers equal the gust peak velocities at the stadium's roof height, the complete wind speed information have been available. A resume of the final data is reported in Table 2.8, where for every direction, the mean velocities and the turbulence intensities are noted down. Obviously the turbulence intensity over the gradient height is zero.

Table 2.8: Measured wind speed profile.

section	angle [° East]	$\overline{U}_{10}$ $[m/s]$	I_u^{10}	$\overline{U}_{25}$ $[m/s]$	I_u^{25}	$\overline{U}_{50}$ $[m/s]$	I_u^{50}	G $[m/s]$
1	20	18.5	0.16	19.5	0.14	21.4	0.13	33.6
2	40	16.6	0.21	20.2	0.17	21.1	0.15	34.6
3	60	16.9	0.20	18.9	0.17	19.8	0.15	34.6
4	80	16.9	0.20	17.5	0.17	18.9	0.16	32.0
5	100	18.4	0.17	18.5	0.17	20.0	0.16	33.5
6	120	19.1	0.18	19.8	0.20	22.4	0.17	34.7
7	140	20.2	0.20	21.0	0.20	23.8	0.17	39.7
8	160	22.5	0.20	27.0	0.18	29.1	0.17	45.9
9	180	23.5	0.20	27.3	0.18	29.4	0.17	47.9
10	200	25.4	0.17	30.8	0.18	36.3	0.14	55.2
11	220	27.0	0.14	31.7	0.12	33.0	0.11	49.2
12	240	23.4	0.19	29.8	0.12	31.0	0.11	46.8
13	260	22.4	0.18	26.3	0.15	28.2	0.14	44.7
14	280	19.3	0.21	22.7	0.15	24.5	0.14	41.0
15	300	18.3	0.19	24.0	0.15	25.5	0.15	39.9
16	320	16.6	0.21	20.7	0.14	22.7	0.13	35.3
17	340	16.3	0.22	19.4	0.14	21.3	0.13	34.6
18	360	17.3	0.19	17.4	0.14	19.1	0.13	30.3

The complete set of data collected in the Wind Tunnel laboratories (RWDI) are useful for building a continuous wind speed profile with the mean velocities as a function of the wind direction θ and the altitude z. The wind speed has been approximated using the power low formulae, that is simpler and handy to be adapted to the available data, in which some special features are included through making variable the exponent α and the wind speed $\overline{U}_{ref}$ at reference height ($z_{ref} = 10\ m$).

$$\overline{U}(z,\theta) = \overline{U}_{ref}(\theta)\left(\frac{z}{z_{ref}}\right)^{\alpha(z)} \tag{2.5}$$

Using the best approximation, the equation's exponent is considered linearly variable with the altitude:

$$\alpha(z) = 0.235 - 0.00075\left(\frac{z}{z_{ref}}\right) \tag{2.6}$$

while the reference wind speed follows the angle dependence as it was pointed out in the experimental results. In this case the best interpolation function is the Gaussian-like equation, see Figure 2.9, through the relation:

$$\overline{U}_{ref}(\theta) = \overline{U}_0 + A \cdot e^{-b(\theta-\theta_0)^2} \tag{2.7}$$

where the coefficients are:

- $\overline{U}_0 = 18\, m/s$
- $A = 7.5\, m/s$
- $b = 0.000235$
- $\theta_0 = 210°$

Generally speaking, $\overline{U}_{ref}$ should be a cyclic function, that means it should be applicable for each positive or negative value of θ; by the way, the choice of a Gaussian-like function allows a very good fitting of peaks values, around $\theta \approx 210°$, even if it loses trustworthiness in the tails. Moreover the interpolation function (2.5) is suitable inside the gradient height specifically over a minimum height z_{ref}, actually $z \in \{10\,; 600\, m\}$. The boundary conditions of this kind of approximation can be written as:

$$30° \leq \theta < 390° \tag{2.8}$$

$$z_{ref} \leq z < \delta \tag{2.9}$$

If the angle overcomes these limits, a round angle translation have to be applied, while for heights lower to $10\, m$ the wind speed is considered constant, equal to the reference velocity.

Figure 2.10 shows the approximation on the four major heights. It can be seen the very good fitting, especially in the lower levels, for the South-West winds cause the peak values have been taken as high weighted constrains in the way to manage more accurate input data on the strongest events. On the contrary, the smaller wind speeds are not well fitted; this is due to the imposed threshold which fixes the minimum value to be not smaller than the 71% of the heaviest value. The enforced constrain, fixed from the design team *Ove Arup and Partners*, mean to give less confidence to very low values of measured wind speed, probably produced by a short testing period collecting data in the meteorological station in Merelim.

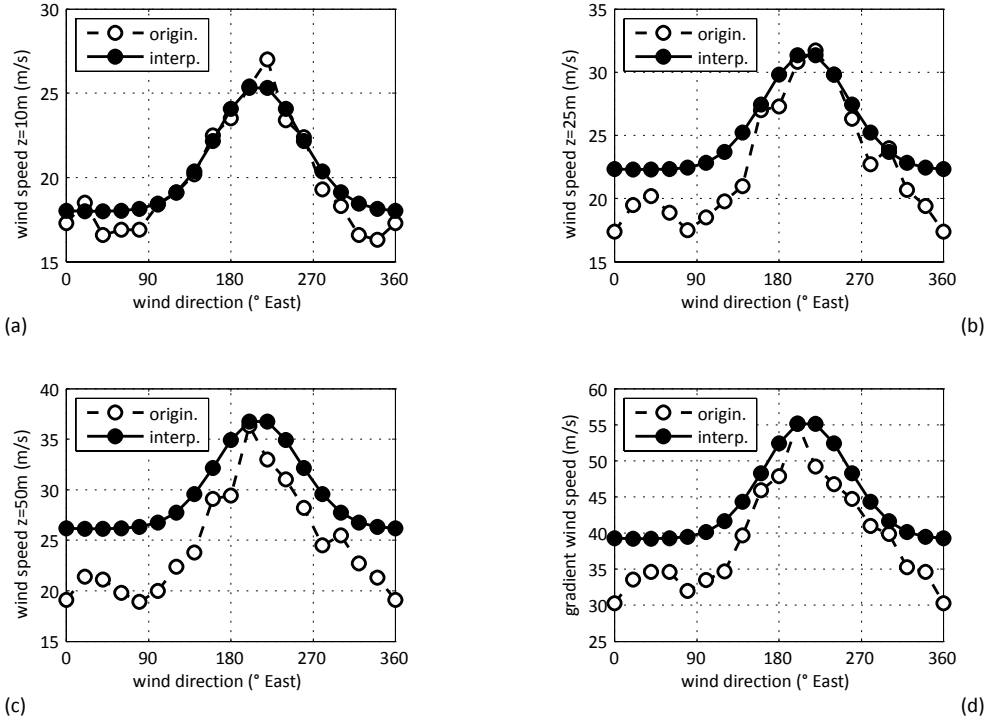

Figure 2.10: Mean wind speed interpolation: a) reference height; b, c) stadium roof $25 \div 50\,m$; d) gradient height.

Concerning the gust peak wind speed, the used simplified formula remains (2.3) (Simiu and Scanlan 1996), where any relation between the turbulence index I_u and the wind direction θ has been noted (see Table 2.8). In this case the interpolation function is the following exponential equation:

$$I_u(z) = 0.195 \cdot e^{-0.075\left(\frac{z}{z_{ref}}\right)} \tag{2.10}$$

which best fits the average of the I_u values in Table 2.8.

As a last comment, a resuming description of the wind intensity at the stadium's roof height is depicted in Figure 2.11 using a wind rose graph. In the picture, the blue triangles represent the mean wind speed through different directions, while the light blue parts correspond to the atmospheric turbulence. It can be easily noted that the strongest wind events come from South - Southwest, i.e. when the storms appear from the top of the quarry, and become slightly lower going toward West. Further analyses, aimed on the worst scenario and presented on chapter 6, are focused on these wind direction.

Figure 2.11: Wind Rose over the stadium.

2.4 WIND SPEED ANNUAL EXCEDANCE PROBABILITY

In general and specially in this case, the *reference wind speed* is based upon data collected during the recent past: usually years more than decades; by the way, using that term it is implied an expectation for the future values. The implicit condition is that the global climate conditions will not change in the future. In other words, estimating extreme wind events do not consider effects such the global warming or the greenhouse effects (Dyrbye and Hansen 1996). Due to that reason, the characterization of extreme winds should be always coupled with some statistical distribution of the presented values, giving a measure of the uncertainties taken into account.

The wind loads on almost every structure is related to the velocity pressure q and a good statistical representation, and normally adopted, for windstorms is the Type 1 extreme value distribution or Gumbel distribution taking q as random variable:

$$q = \frac{1}{2}\rho U^2 \tag{2.11}$$

in which ρ is the air density and U is the mean wind speed. The cumulative distribution function of the annual velocity pressure F_q^1 is given by:

$$F_q^1(q) = \exp\left[-\exp\left(-\frac{q-\alpha_q}{\beta_q}\right)\right] \tag{2.12}$$

where α_q and β_q are the location and scale parameters, respectively, that characterize the Type 1 extreme-value distribution (see appendix B). Typical values of these parameters lead to Eurocode's constant $K_q = \beta_q/\alpha_q = 0.2$.

The probability density function (pdf) and the main statistics like the mean value and the standard deviation, of (2.12) are:

$$f_q^1(q) = \frac{1}{\beta_q}\exp\left[-\frac{q-\alpha_q}{\beta_q} - \exp\left(-\frac{q-\alpha_q}{\beta_q}\right)\right] \tag{2.13}$$

$$\mu_q^1 = \alpha_q + 0.5772\,\beta_q \tag{2.14}$$

$$\sigma_q^1 = \frac{\pi}{\sqrt{6}}\beta_q \tag{2.15}$$

The cumulative density function referred to a N-years event, which fit the same distribution, is a simple shifting of (2.12); thus:

$$\mu_q^N = \mu_q^1 + \beta_q \ln(N) \tag{2.16}$$

$$\sigma_q^N = \sigma_q^1 \tag{2.17}$$

According to the previous relations, the velocity pressure $q(p)$, calculated with an *annual exceedance probability* equal to $p = 1 - F_q^1(q)$, can be calculated as:

$$q(p) = \alpha_q - \beta_q \ln(-\ln(1-p)) \tag{2.18}$$

In particular, dividing (2.18) by the 100-years velocity pressure q_{100}, a proportional coefficient between the unknown and known velocity pressure is obtained:

$$\frac{q(p)}{q_{100}} = \frac{1 - K_q \ln(-ln(1-p))}{1 - K_q \ln(-ln(0.99))} \tag{2.19}$$

According to Eurocode 1, the square root of the last equation is used to calculate the corrective coefficient C_q that transform a reference wind speed U_{100} into a generic velocity $U(p)$ related to a different annual exceedance probability p and consistent return period $T_r = 1/p$; the latter simplified relation is effective only for small probabilities.

$$U(p) = C_q U_{100} = \sqrt{\frac{1 - K_q \ln(-\ln(1-p))}{1 - K_q \ln(-\ln(0.99))}}\, U_{100} \tag{2.20}$$

Turning the problem around, given a reference wind speed U_{100} related to its annual probability of exceedance $p^{100} = 1/T_r = 0.01$, it is possible to calculate the annual probability of exceedance p of any other wind speed $U(p)$:

$$p = 1 - \exp\left[-\exp\left(\frac{1 - A^{100} C_q^2}{K_q}\right)\right] \tag{2.21}$$

In which the coefficient $A^{100} = 1 - K_q \ln(-\ln(0.99))$. Comparing (2.12) and (2.21), where $p = 1 - F_q^1$ and applying the Eurocode constrain $K_q = \beta_q/\alpha_q = 0.2$, the two distribution parameters α_q and β_q can be directly related to a reference velocity pressure associated to a return period of N-years.

$$\alpha_q = \frac{q_N}{1 - K_q \ln\left(-\ln\left(1 - \frac{1}{N}\right)\right)} \tag{2.22}$$

$$\beta_q = \frac{q_N\, K_q}{1 - K_q \ln\left(-\ln\left(1 - \frac{1}{N}\right)\right)} \tag{2.23}$$

Figure 2.12 shows the cumulative distribution function (2.12) the annual exceedance probability (2.21) and the probability density function (2.13) adjusted to the specific case of the Stadium of Braga. On the abscissa axis the ratio between different velocity pressure and the reference one ($T_r = 100$ years) is plotted.

Finally the annual exceedance probability curves changing the wind intensity are plotted in Figure 2.13. Looking at Figure 2.13a it is easy to note the exponential decrement of p increasing the wind load in terms of velocity pressure. While Figure 2.13b shows the *probability of hazard p* in relation to the wind speed (*hazard intensity*) for different wind directions. Results of the last graph are used for the estimation of the structural risk of failure of the roof in chapter 6.

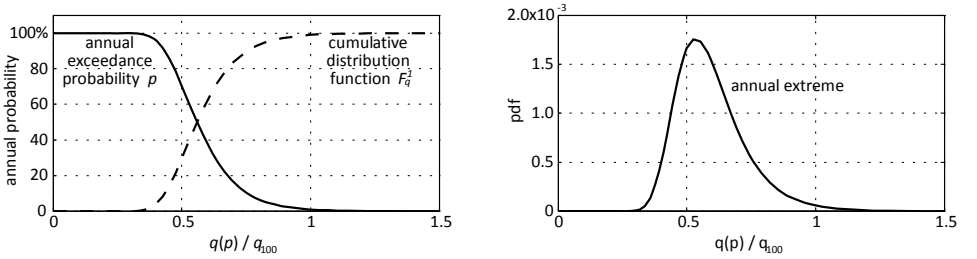

(a) (b)

Figure 2.12: Extreme value Type 1 distribution: a) cumulative and annual exceedance distribution; b) probability density function.

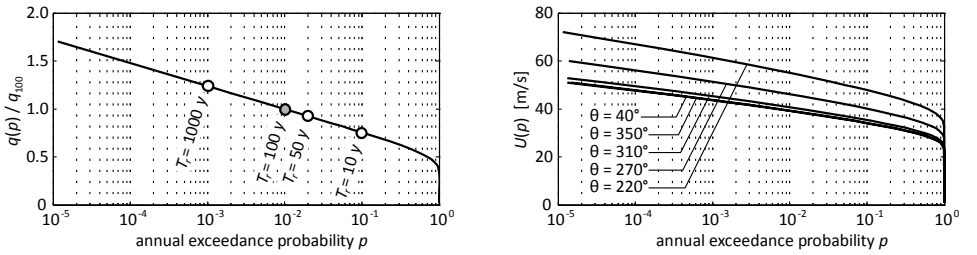

(a) (b)

Figure 2.13: Windstorm annual exceedance probability: a) referred to the velocity pressure; b) referred to the wind speed in different wind directions.

CHAPTER 3

WIND PRESSURE LOAD

Once the hazard (H) on the stadium of Braga is defined, the second step in the risk assessment chain (Figure 1.5) aims to convert the windstorm effects into loads (HL) to be applied directly on the stadium roof. The exposure of the stadium to windstorms depends on the specific surrounding nearby the structure; in particular changing, the incoming wind direction, different obstacles are encountered by the flow and different vortexes are generated. The exposure analysis should duly take into account all the aspects that can change the HL such the topography contiguous to the stadium.

In reference to the present case study, there are two mean possibilities to perform such transformation:

- the *Computation Wind Engineering* (CWE) analysis;
- the straight measure of physical quantities over a scale model in *wind tunnel* tests.

CWE is a part of *computational fluid dynamics* (CFD), widely investigated at the moment, however the lack of specific codes or effective prescriptive instruments prevents its diffusion in civil engineering, where it is advisable to measure aerodynamic forces or pressures directly in scale model. As a consequence, it appears evident why modern structures, more and more complicated and sensitive to fluid-structure interactions, are often supported by expensive scale model tests, given that CWE analyses are still deficient in their reliability and applicability.

In this section results of a wind tunnel test of the Stadium of Braga carried out by the RWDI (2001) are presented. The measured data is a complete set of pressure coefficients fields in time and space domain for 36 wind directions. Particular attention is paid presenting an efficient method to manage this huge amount of data re-elaborating the experimental pressure fields, neglecting all the ineffective information and leaving the most relevant coherent structures only.

3.1

PRINCIPAL COMPONENT ANALYSIS

Huge amounts of data need special approximation and synthesis techniques to improve their comprehension and a quick comparison between results. Pionering studies in the field were issued at the beginning of the last century by Karl Peterson, who developed the *principal component analysis* (PCA) (Pearson 1901) and later by Michael Loève, who produced a systematic investigation of generic orthogonal decomposition (Loève 1955). The pervasive successful and use of PCA let the creation of many techniques appear specific for different field of application. Specific techniques are the discrete *Karhunen–Loève transform* (KLT), the *Hotelling transform*, the *singular value decomposition* (SVD) and the *proper orthogonal decomposition* (POD). POD techniques, in particular, are extensively applied in wind engineering applications, when data sets are pressure distribution on a surface; therefore, a particular emphasis is given to this approach.

PCA is a powerful tool used in exploratory data analysis in predictive models, as it involves a mathematical procedure that transforms a number of possibly related variables into a smaller number of independent variables called principal components. The most of the variability is considered by the first principal component, and each following component accounts for as much of the remaining variability as possible. The technique involves the calculation of the *eigenvalue decomposition of a data covariance matrix*, generally after mean centring the data for each attribute.

PCA is the simplest of the true eigenvector-based multivariate analyses. It can be seen as a mean to reveal the internal structure of the data set, keeping the information which explains the variance of the dataset itself. If a multivariate dataset is visualised as a set of coordinates in a high-dimensional data space (1 axis per variable), PCA is a mean to supply the user with a lower-dimensional picture, a *shadow* of this object when viewed from its most informative viewpoint (Wikipedia PCA), to achieve a representation which should be easier to comprehend. Mathematical definitions can be founded in (Jolliffe 2002), where PCA is described as an orthogonal linear transformation that transforms the data to a new coordinate system such that the greatest variance by any projection of the data comes to lie on the first coordinate (*first principal component*), the second greatest variance on the second coordinate, and so on. The first principal component (the eigenvector with lowest frequency) will correspond to a line that passes through the mean and minimizes sum squared error with those points. Subsequently principal components correspond to the same concept after all correlations with the previous principal component have been subtracted out from the points. Hence, the sum of all the eigenvalues is equal to the sum squares distance of the points with their mean divided by the number of dimensions.

PCA can thus be considered as the optimum transform for compressing a set of high dimensional vectors into a set of lower dimensional vectors and then reconstructing the original set. The applicability is limited by the assumptions (Shlens 2005) made in its derivation, which are:

- *Assumption on Linearity*: it is assumed that the observed data set is linear combinations of certain basis.
- *Assumption on the statistical importance of mean and covariance*: PCA uses the eigenvectors of the covariance matrix and it only finds the independent axes of the data under the Gaussian assumption.
- *Assumption that large variances have important dynamics*: PCA performs a coordinate rotation that aligns the transformed axes with the directions of maximum variance. It is assumed that the principal components with larger variance correspond to interesting dynamics and lower ones correspond to noise.

Essentially, PCA involves only rotation, scaling and sorting. In particular sorting the components can be widely used for dimensionality reduction in a data set by retaining those characteristics that contribute most to its variance, by keeping lower-order principal components and ignoring higher-order ones. Such low-order components contain the *most important* physical aspects of the phenomena. This particular feature is widely used in many points of the present work.

3.1.1

Proper Orthogonal Decomposition

Some of the first researchers who investigated the complex fluctuating pressure pattern on buildings using eigenvector analysis are: (Armitt 1968) during his study on the wind pressure fields on the West Burton cooling tower, (Lee 1975) for the systematic studies on prismatic bluff bodies, (Best and Holmes 1983), (Kareem and Cermak 1984), (Holmes 1990) focalized on applications to isolated low-rise buildings.

Although there are no doubts about the incredible synthesis feature of the POD techniques and the consequent computational consuming saving, the physical meaning of the eigenvector modes is still a controversial issue. Initially Armitt suggests that there are no reasons to suppose that the spatial variation pressure field due to one cause has to be necessarily orthogonal with respect to that due to other causes; the mathematical constraints of orthogonality are too strong to describe the nature' behaviour. Another drawback is the relationship between the total number of modes found in the analysis and the number of pressure cells. It is implied that the number of points or panels considered

must be high enough to describe the modal forms in a exhaustive manner, but for the investigation purposes only the lower modes are considered, the higher ones with low energy will just complete the mathematical system of equations.

Nevertheless, Holmes (1990) notes that the separated physical causes implies zero correlation between the modes, so the orthogonal techniques are the most indicated to find such uncorrelated forms. For instance, during his study of wind effects on a circular silo, the superposition of the first two proper modes with the mean pressure distribution and its rate of change with angular position are shown. Similar considerations are reported by several authors, (Vickery 1993), (Gilliam, et al. 2004), who resume all the wind fields by the combination of few modes. Afterwards Holmes (1997) partially reviews his position pointing out that any physical interpretation of the proper modes could be misleading or fictitious in many cases.

A very helpful contribute in fixing conflicting opinions is exposed in a very exhausting paper by Tamura (1999) when he demonstrates that the first proper modes always represent the mean pressure distribution and how this feature creates an heavy constrain for other modes which must be orthogonal to the first one. An author's opinion deals to apply the decomposition only on the fluctuating wind pressure nil mean. Using this precaution, the physical interpretation of the POD modes can be discussed but not at all generalized.

Writing about the problem of generalizing wind loads, Davenport (1995) suggests three space functions which control the magnitude of the responses: the POD, powerful for the synthesis, the influence lines and the natural frequency mode shapes. When the eigenvectors of the covariance matrix (proper modes) are closed to the other representations, they boost some stress resultant (force/moment) diagram or some instability shape. In those cases the modes can be considered separately ((Holmes 1990), (Tamura, et al. 1999)), otherwise the wind load must be written as the combination of modes.

Theoretical aspects

Pressure fluctuations on buildings in natural gradient flows produced by storms have a complex temporal and spatial structure and its study, keeping under control the whole physical phenomena, is quite difficult. One help in tackling this issue is provided by the POD techniques (Loève 1955) that offers the double benefit to decompose the turbulent flow field $\tilde{p}(x,t)$ in uncorrelated proper modes, that have to be simply summed each other, and to extract the space dependant information, stored in load surfaces, from the time histories, which includes the wind action dynamics.

$$p(x,t) = \bar{p}(x) + \tilde{p}(x,t) \tag{3.1}$$

$$\tilde{p}(x,t) = \sum_{k=1}^{M} a_k(t)\, \phi_k(x) \tag{3.2}$$

The first feature allows sorting all the k-modes following energetic criteria, the lower modes include most of the signal's energy and they must be taken into account, while the other can be neglected. This consideration permits to characterize the phenomena with a physical quantity (total amount of energy) and not by means of modelling discretization (total number of pressure cells).

The second feature allows to focus directly to the pressure waves $\phi_k(x)$, one for each k-mode, which are superimposed as a load on the structure. Every wave has an independent dynamic represented by the $a_k(t)$ vectors, which maintain the units of the pressure field. The key aspect of (3.2) consists into computing the energy E_k stored inside $a_k(t)$ and including it inside the proper mode. In this way the eigenvector is turned in a static pressure surface.

$$\tilde{p}_k(x) = \sqrt{E_k} \cdot \phi_k(x) \tag{3.3}$$

$$E_k = \frac{1}{T}\int_0^T a_k^2(t)\, dt \tag{3.4}$$

where $\tilde{p}_k(x)$ is the equivalent pressure surface related to the k-mode, $T = (N-1)dt$ is the signal's length, N is the number of trials with time step dt. In the discrete calculus the integral is changed by the sum symbol. The coordinate vector of a mode is rewritten as $a_k(t) = \sqrt{E_k}\, u_k(t)$, where the energy is $E_k = \lambda_k\, dt/T$, λ_k are the eigenvalues of the zero-time-lag covariance matrix of the process and $u_k(t)$ are the dimensionless coordinate. With those remarks (3.3) can be written as:

$$\tilde{p}_k(x) = \sqrt{\lambda_k \frac{dt}{T}} \cdot \phi_k(x) = \sqrt{\frac{\lambda_k}{N-1}} \cdot \phi_k(x) \tag{3.5}$$

In order to visualize this expression an ideal situation is presented when a proper mode $\phi_k(x)$ is stressed by a simple harmonic wave $a_k(t) = A\cos(\omega t)$. The energy of the signal is half of the square of the wave amplitude $E = A^2/2$, thus the equivalent static pressure (3.5) is the eigenvector multiplied by the 70% of the amplitude: $\tilde{p}_k(x) = A/\sqrt{2} \cdot \phi_k(x)$.

Starting with the latter dimensional expression of the proper modes, some comments on the use of the POD can be done. First of all the proper modes $\phi_k(x)$ are computed as the eigenvectors of the covariance matrix, so they are defined apart from a constant factor. This constant makes the modes be unitary respect their energies but the signs remain undefined. Two different modal compositions are possible in order to find the equivalent static pressure field: algebraic and geometric sum.

In the algebraic composition every pressure modes (3.5) is simply added to the mean pressure distribution. In this case the sign variation forces the user to consider many combinations to reach the conservative solution.

$$p_{eq}^{alg}(x) = \bar{p}(x) + \sum_{k=1}^{M} \pm\tilde{p}_k(x) \tag{3.6}$$

This form can become easily expensive because there are 2^M possible combinations, but it is the safest.

On the other side, a geometric sum implements the square root of the sum of squares (SRSS). In this case the sign does not affect the result. The final combinations are just the mean pressure field plus or minus the calculated equivalent pressure fluctuation:

$$p_{eq}^{geo}(x) = \bar{p}(x) \pm \sqrt{\sum\nolimits_k \tilde{p}_k^2(x)} \tag{3.7}$$

The second equation is more handy and direct. It follows the same synthesis concept used to remove the time dependence of the field on the modes merging. The drawbacks are the addition of safety coefficient to reach suitable security levels and the sign levelling.

The geometric combination (3.7) is normally suggested on standards and codes with the gust peak factor technique, e.g. (Eurocode_1-1-4 2005) (CNR-DT_207-08), where the equivalent static wind pressure field is obtained by the mean values plus the amplified standard deviation of the field.

$$p_{eq}^{gpf}(x) = \bar{p}(x) \pm g \cdot \sigma(x) \tag{3.8}$$

where g is the amplification factor, extensively discussed in (Davenport 1964) and (Solari 1990), and $\sigma(x)$ is the standard deviation distribution through the surface. Mathematically the equality of the geometric modal composition with the standard deviation can be demonstrated.

$$\sigma(x) = \sqrt{\sum_k \tilde{p}_k^2(x)} \tag{3.9}$$

Relation (3.9) reveals the pointlessness of performing the orthogonal decomposition if the final output should be the equivalent pressure field (3.8). Computing the standard deviation directly from the original data makes much more sense than perform the POD analysis and subsequently apply (3.7).

3.2 PRESSURE LOADS ON THE STADIUM ROOF

The dynamic nature of the wind fluctuations, as well as the geometric non-linear nature of the structure, prevents the designer from studying the structural response with simple static or frequency domain analyses. In order to estimates the structural response with the highest degree of precision, a set of time domain dynamic analyses are provided.

Wind load on the stadium roof provided by a complete set of pressure time histories covering the whole surfaces, expressed in terms the reference kinetic pressure q_{ref} which depends on the extreme wind intensity (hazard intensity from section 2), and the pressure coefficients C_p.

$$p(\boldsymbol{x}, t) = q_{ref} C_p(\boldsymbol{x}, t) \tag{3.10}$$

The pressure coefficients are derived from a wind tunnel study on a rigid scaled model carried out by the RWDI laboratories in Canada (RWDI 2001). In such a process, all the time and space correlations between different points or at different time are included into the C_p fields and assumed unrelated to main wind speed. In these tests the stadium and the nearby surrounding were carefully reproduces with length scale of 1:400 (Figure 3.1a).

The wind pressure on the two slabs was measured along 36 directions, 10° spaced, starting from the true North going through the East direction (clockwise). During each test, 200 pressure taps were installed globally: 60+60 on the upper surfaces and 40+40 on the lower surfaces (Figure 3.1b). According to the measured wind speed profile (see chapter 2), the pressure coefficients were referenced to the mean kinetic pressure measured at the gradient height that is $600\ m$ in full scale.

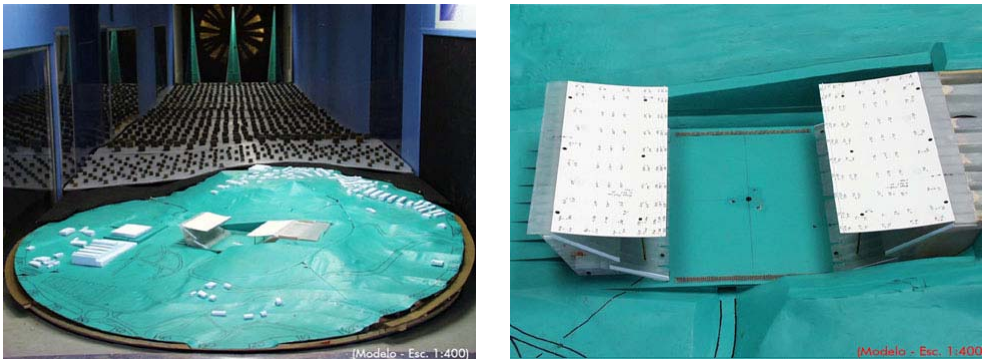

(a) (b)

Figure 3.1: Rigid scaled model: a) complete view of the model; b) particular of the stadium.

Acquisition was made at 512 samples per seconds for almost $24\ s$, under the effect of the wind tunnel test speed, at equivalent gradient height, of approximately $14.6\ m/s$. The time scaling of the samples is obtained combining the length scale $\lambda_d = 1/400$ with the appropriate velocity scale $\lambda_v = 14.6/\overline{U}_{600}$, where the gradient wind speed varies with the wind direction according (2.7). Considering the minimum and maximum value of $\overline{U}_{600} = 40 \div 55\ m/s$ (Figure 2.10d), corresponding to the length scale range $\lambda_t = 1/145 \div 1/107$, the true time step of the series is $dt = 0.28 \div 0.21\ s$ function of the wind direction. Converting the whole series by using these values implies arranging extreme wind pressure fields with constant gradient speed for $45 \div 60$ minutes that are unrealistic events. For that reason the FEM model has been loaded with small parts of the entire signals. In the analyses all the time parameter are referred to the true scale.

In order to obtain the net pressure distribution on a suitable mesh grid, comparable to the structural mesh of the slabs, all the pressure time histories have been interpolated by using the NURBS technique (Piegl and Tiller 1997). In this way it was possible to convert the 6×10 pressure taps of the upper surfaces and the 4×10 of the lower one into a fine mesh of 13×35 points for each surface and both sides. In the interpolation, a quadratic spline was used in the along-the-cable direction ($6/4 \rightarrow 13$ points); while a cubic spline was used in the across-the-cable direction ($10 \rightarrow 35$ points). All the interpolation process have been duly checked, paying attention to improve the resolution of the input data maintaining unchanged the boundary conditions.

All data collected have been treated using the POD (see section 3.1) in order to assist the implementation into the Finite Element code. For each direction, $2 \times 35 \times 13 = 910$ time series with 12200 trials each are available. This huge amount of data is very difficult to handle, thus, for each direction, it was decided to taking out the mean pressure field and to manipulate the pressure fluctuation using (3.2).

Considering for instance the wind blowing from behind the quarry ($\theta = 220°$), Figure 3.2 depicts the mean pressure and the standard deviation fields. The symmetric distribution of all the pressures coefficients appears evident; this is due to the symmetric morphology of the structure as well as the symmetric load case. From this direction, the air slides over the quarry and over the slab on the right hand side and hit the opposite one. The peak values in the standard deviation graph indicate the highest level of turbulence when the flow knocks the second slab.

Following just these two preliminary data set (mean and st.dev pressure fields) it appears that the simplest way to predict the structural response is to model only a single stripe of the roof slicing the slabs within two consecutive cables gaps. By using suitable boundary conditions to reproduce a *plane stress* system it should be possible replacing the slab shells with equivalent 2 dimensional beam elements and to estimate the response assumed constant in the across-the-cable direction. This procedure can be satisfactory considering just the mean pressure field which includes only the 71% of the total energy; while the pressure fluctuation that is the 29% of the total energy, summarized with the standard deviation is anything but an average over the time of the real signal. During the real time domain load process there will never be a single instance where the wind load follows the distribution shown in Figure 3.2.

Decomposing the wind fluctuation part into orthogonal modes by using the POD technique, it appears evident the different pressure configurations superimposed during the load procedure. Figure 3.3 shows the first mode that includes the 22% of the fluctuation energy corresponding to a 6% with respect to the total energy. It is clear how the cylindrical behaviour of the structure is invoked in this symmetrical load. The modes distribution is totally similar to the standard deviation distribution. The only differences are into the smoothes in left-slab C_p and in the value. It is worthy underline that the values reported on the level curve view are not pressure coefficients but the average values obtained with (3.3); in order to obtain the real distribution it is necessary multiply these values and the time history of the mode.

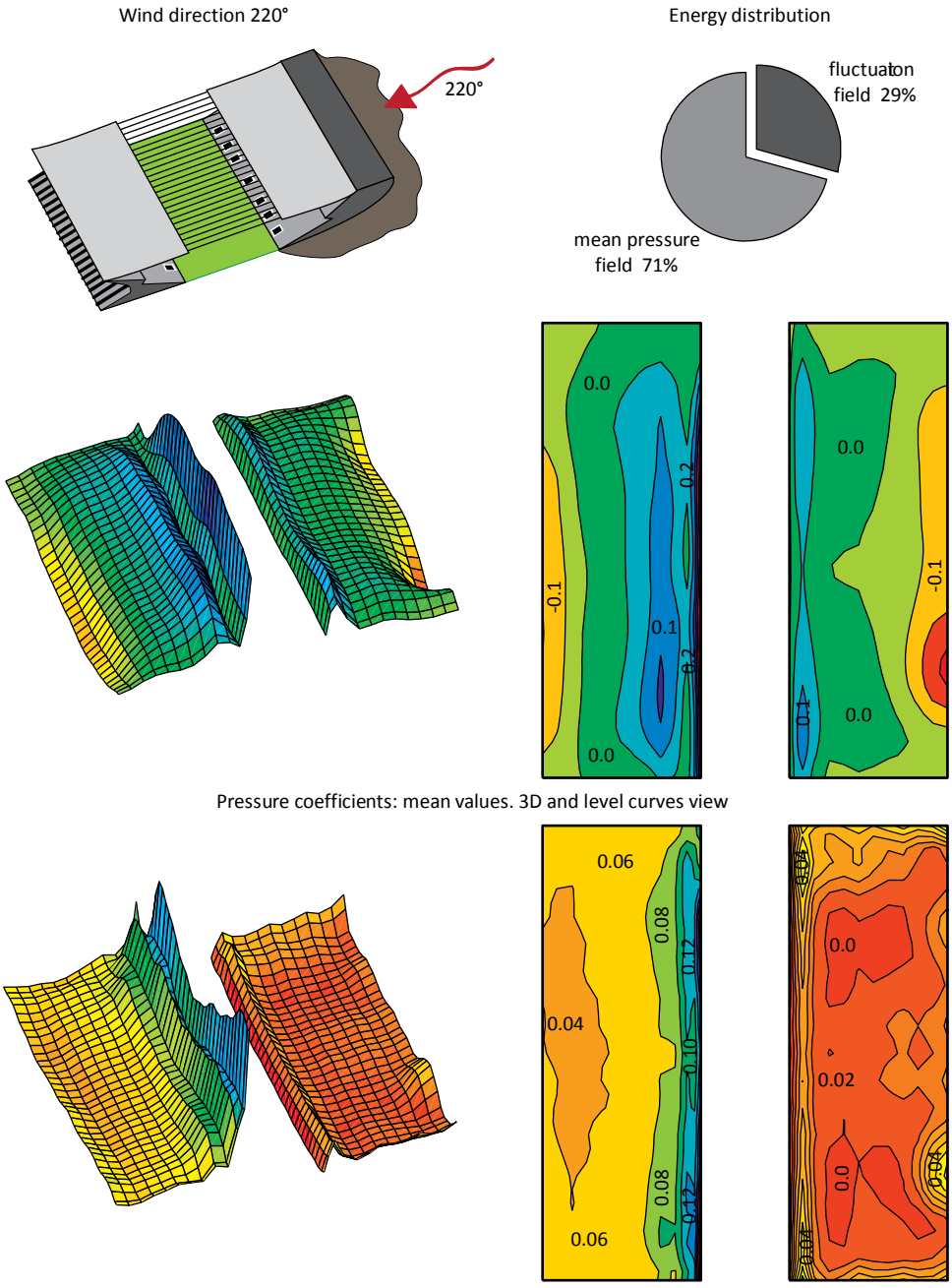

Figure 3.2: POD analysis on the pressure coefficients. Mean values and standard deviation.

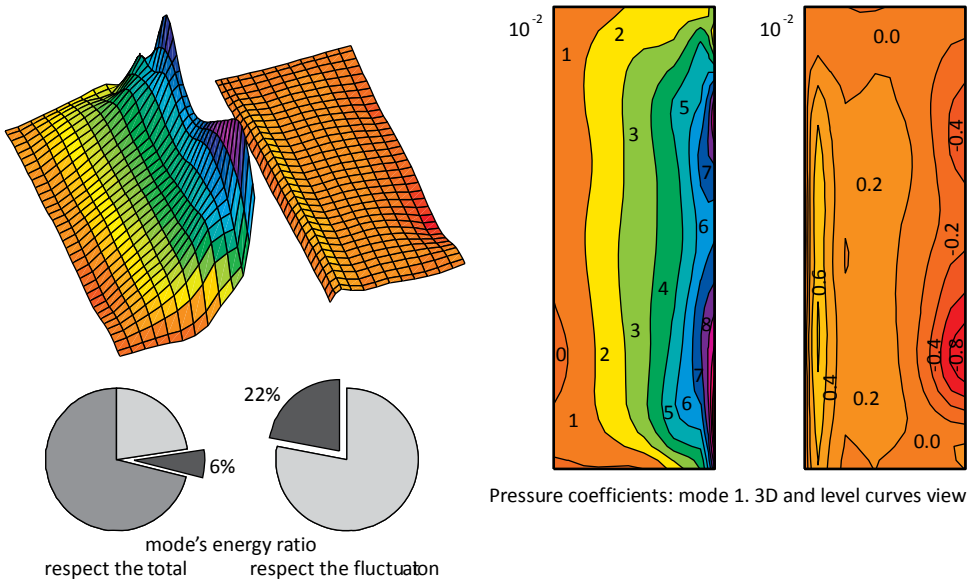

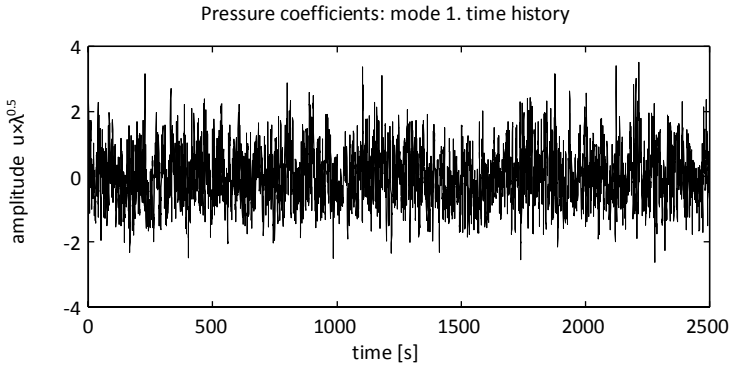

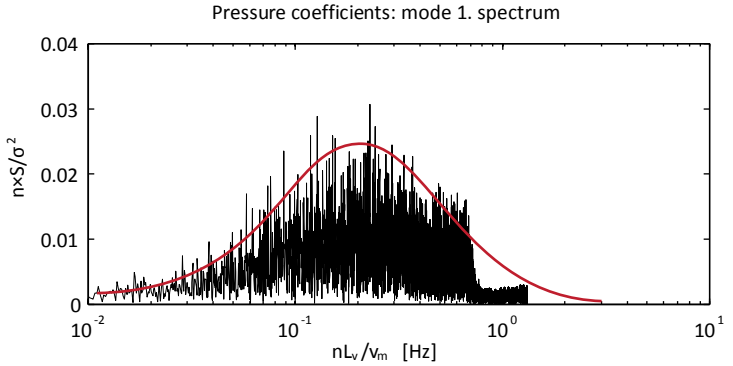

Figure 3.3: POD analysis on the pressure coefficients. Mode number 1.

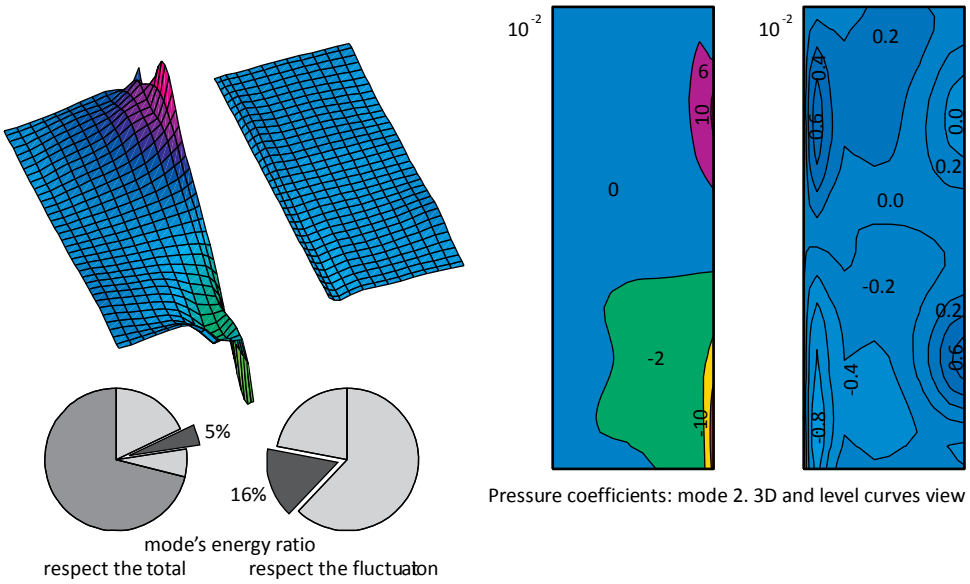

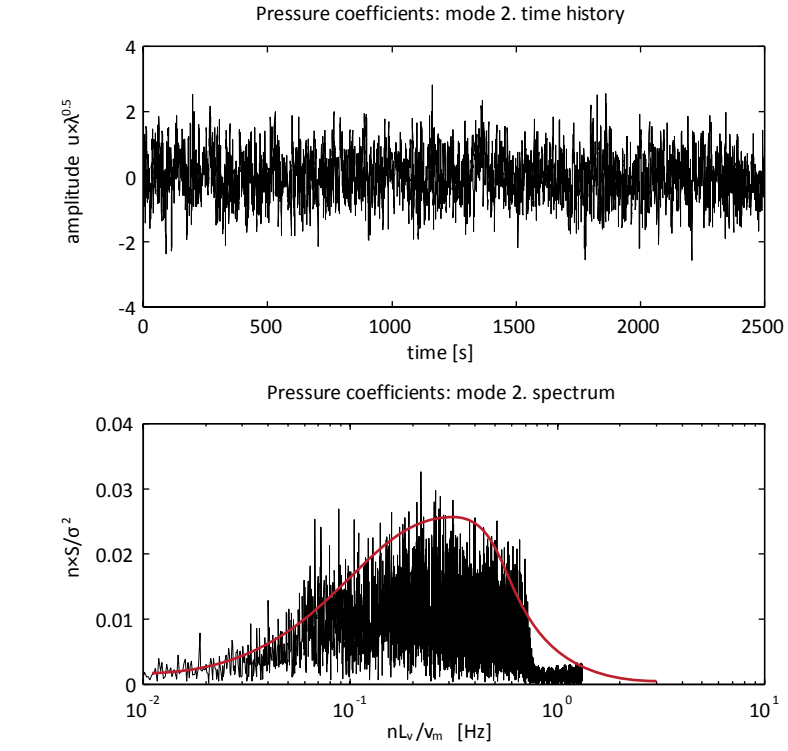

Figure 3.4: POD analysis on the pressure coefficients. Mode number 2.

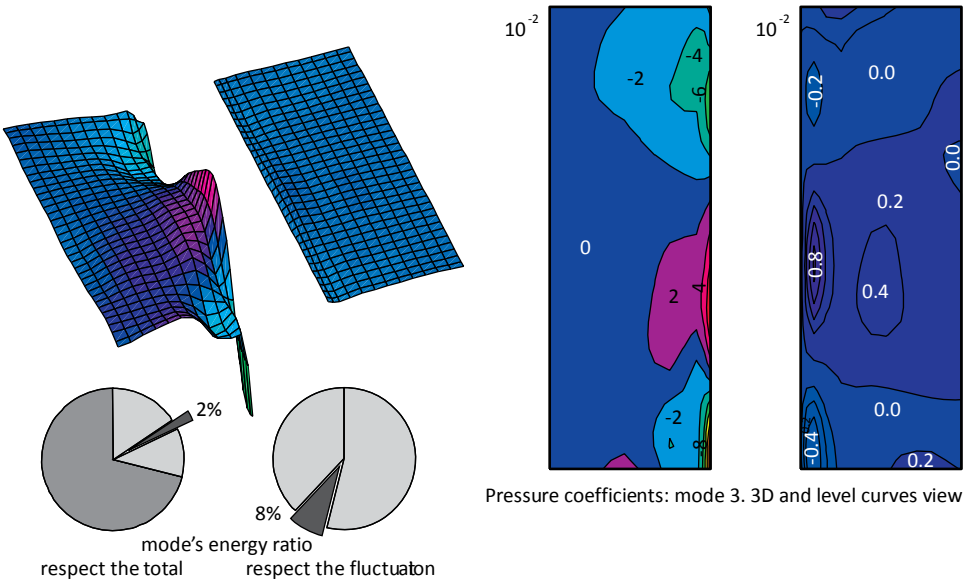

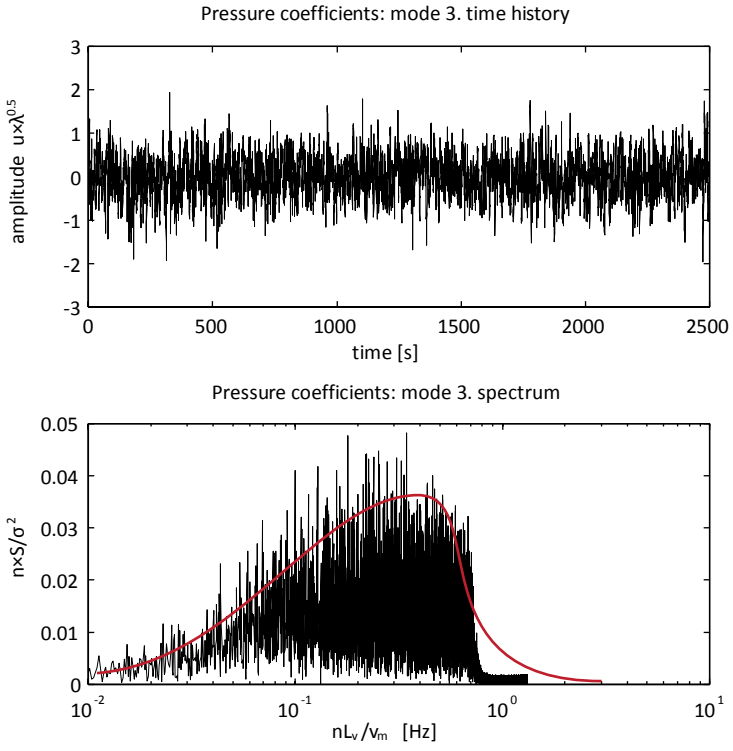

Figure 3.5: POD analysis on the pressure coefficients. Mode number 3.

On the contrary, starting from modes 2 on the across-the-cable relative pressure distributions assumes more and more importance sign of the great relevance of the complete 3 dimensional behaviour of the roof. The second mode (Figure 3.4) summarizes 5% of the total wind energy alone. Its distribution involve only the bending moment of the left slab in the across-the-cable direction: an effect completely neglected using a simplified stripe model or loading a complete roof by using the standard deviation distribution. The third mode (Figure 3.5) emphasizes more this aspect drawing 2 waves (3 peaks) on a slab, charging the shape complexity with a reduction in the energy ratio: 2% of the total.

The previous discussion provides evidence for the huge advantage in using the POD technique (section 3.1.1) in analysing pressure fluctuations due to wind action. As already explained, this method highlights the hidden structure inside complex signals like a complete time-domain pressure field. The proper modes analysis helps to assess the loads characteristics thus it helps in designing a suitable numerical model of the structure. In the following chapters, the same technique will be used also to evaluate the structural response when the output data are expressed in time series. In this view the POD can be used either for the input or the output data in a time-domain numerical analyses.

Another interesting feature of the orthogonal decomposition concerns the modes' time series. Considering that the pressure coefficients decomposed into proper modes have the same source, that is a wind excitation, it makes sense thinking that all comprise the same or at least similar frequency content. The feeling is confirmed applying the Fourier Transform to the modes' time histories, extracting in this way the modal spectra. Figure 3.3-3.5 depicts the spectra corresponding to the lower modes globally consistent with a generic Von Karman power spectrum (Von Kármán 1948):

$$\frac{nS}{\sigma^2} = \frac{nA}{(1 + Bn^p)^q} \tag{3.11}$$

where the parameters A and B fix intensity and position, while the exponential p and q fix the curve's shape. Logical consequence of this feature is that, even when the frequency information of the modes are not available, it is possible substituting completely the mode's fluctuations with a unique straightforward spectrum. Generating new time series using the superposition of elementary waves (Shinozuka and Jan 1972) (Rossi, Lazzari and Vitaliani 2004) starting from a spectrum (3.11) and applying those signal to the pressure modes (3.3) means rebuild a complete pressure field in the time domain, perfectly equivalent to the one measured in the wind tunnel test (Olivato, et al. 2010).

In the present work the time-domain pressure coefficients are available, thus there is no need to generate new signal starting from the Von Karman spectra. The POD analysis is made in order to better understand the input signals, but also to compress the information, neglecting less important data. Starting from 910 time series corresponding to the 910 pressure taps uniformly distributed over the two slabs, the POD analysis output are 910 proper modes and the corresponding 910 time series (see section 3.1.1). A great benefit of the orthogonal decomposition is sorting the proper modes with the energetic criteria. Figure 3.6 shows the cumulative energy reached considering a certain number of mode. In the following analyses only the firsts 40 modes are considered, this means to include the 91% of the fluctuation energy corresponding to the 97% of the total one (mean + fluctuation). In terms of memory allocation, the 97% of the pressure field is reproduced storing less than the 5% of the input data; then when it is required the pressure field is rebuild by using (3.2).

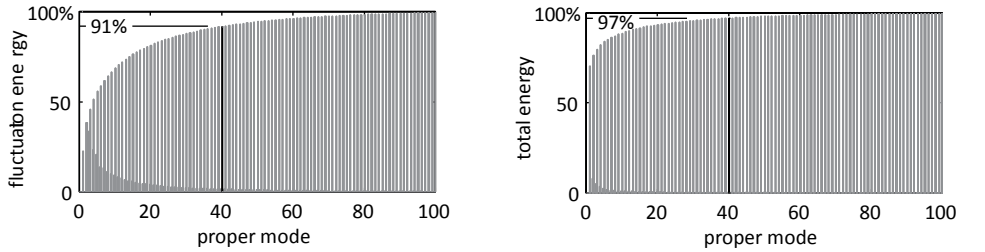

Figure 3.6: Cumulative energy: a) with respect the fluctuation term; b) with respect the total energy.

The presented results of the POD analysis are referred to a single wind direction, that is 220° with respect the North. Obviously, the whole discussion can be extended to all directions. As an example, Figure 3.7 and Figure 3.8 show the application of the POD technique in terms of the mean pressure distribution and the firsts proper modes for other four angles: 270°, 310°, 350°, 40° respectively.

Looking at the graphs, it can be seen that when the wind blows from a later side, e.g. 270°, 310°, 350°, the edge effects are predominant and the distribution of pressures is located on the first edge encountered by the flow. In particular, during events coming from the across-the-cable direction (310°) the pressure distribution as well as the fluctuation is located only on the first part of the slabs. When the flow comes from an open field and it founds the two airfoils as first obstacle, the produced vortexes are big enough to jump the whole covering, without affecting the back part of the slabs.

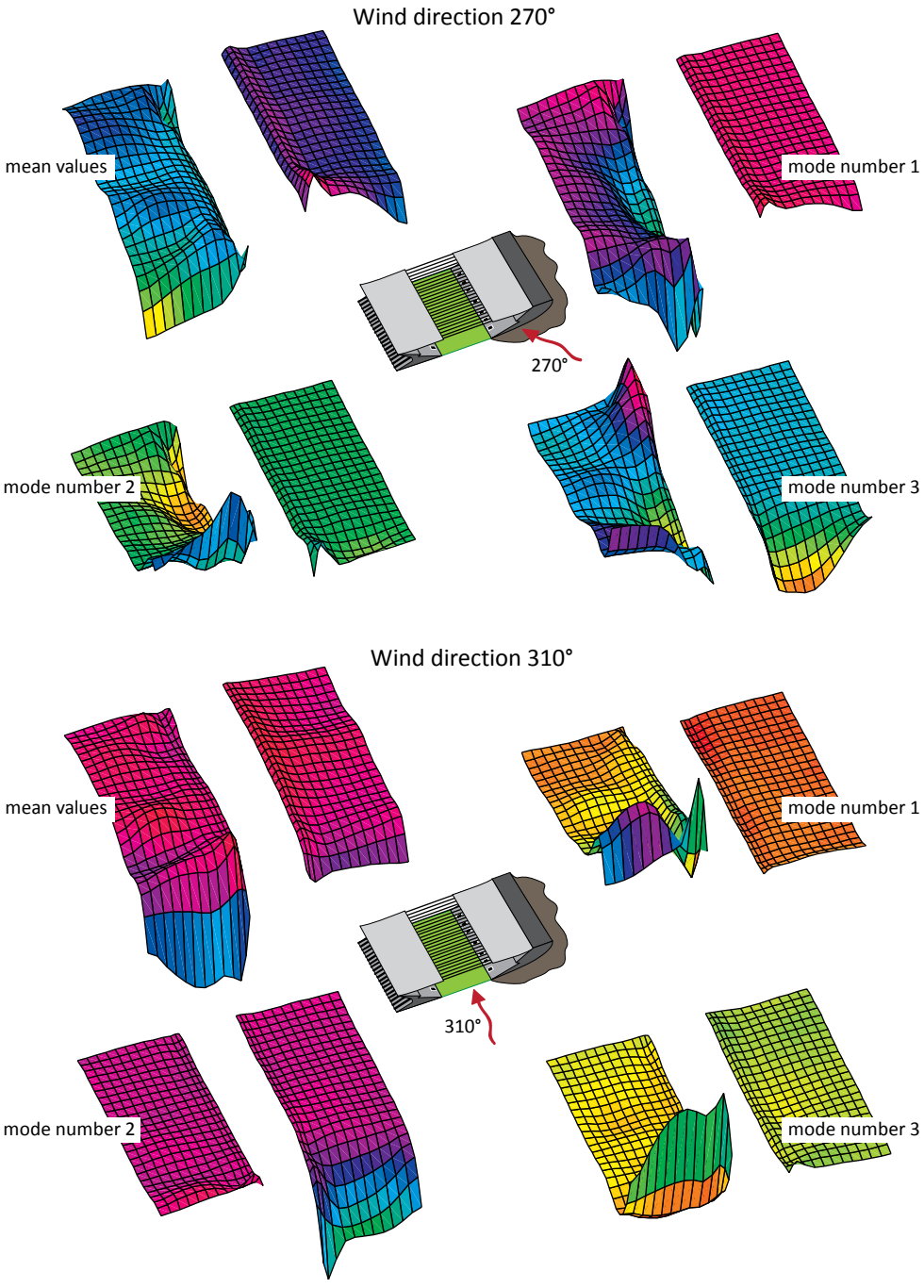

Figure 3.7: POD analysis. Mean pressure and modes number 1, 2, 3. Wind direction 270° and 310°.

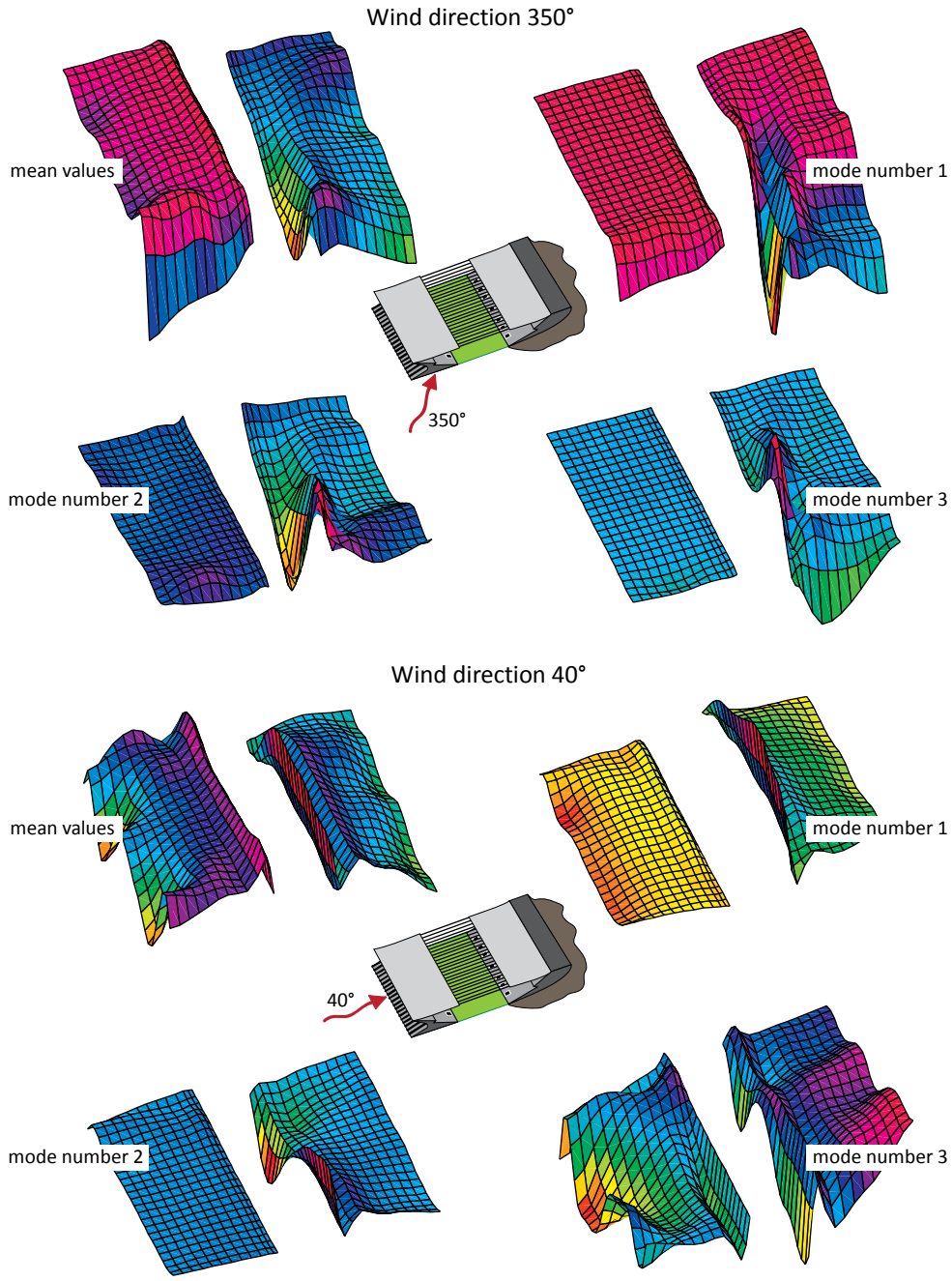

Figure 3.8: POD analysis. Mean pressure and modes number 1, 2, 3. Wind direction 350° and 40°.

Another interesting comment should be done comparing the pressure distribution in the opposite directions 220° (Figure 3.2-3.5) and 40° (Figure 3.8). In the first case the wind comes from the top of the quarry, while in the second case it comes from the ground floor and hit the whole $45\ m$ of grandstand. In the latter the mean pressure affects both the slabs in analogous manner, while the fluctuation is still greater on the second slabs encountered by the flow: the 1st and 2nd mode are very similar while only the 3rd one is different.

As the last note, it should be stressed that the presented POD analyses regard only the loads applied by a windstorm: considerations about load shapes, e.g. symmetries, cannot be expected in the structural response, in terms of displacements velocities etc., because the roof is flexible enough to filtering all the input signals giving back mainly its modal shapes. Details about this aspect are given in Chapter 4.

CHAPTER 4

NUMERICAL MODEL OF THE STADIUM

In many cases the constructions may be considered as continuous mechanical systems composed by an infinite number of degrees of freedom. Accordingly, it is necessary integrating the *differential equations of equilibrium* in order to find the structural behaviour due to the effects of external loads. Nevertheless, this kind of approach is usually very complicated or even impossible if we think to advanced geometries, special boundaries conditions or unsettled material properties. Practical aspects require simplified approaches allowing at least an approximated analysis of the structure. The most known and used method in structural engineering is the *finite element method* that reduces the whole domain into a finite number of degrees of freedom approximating the actual geometrical and mechanical properties. Using this method a revision of the equations of equilibrium into an algebraic system of equations is possible.

4.1 COROTATIONAL TRUSS ELEMENT

In this section a rapid overview about the truss finite element technology is reported. According to the corotational procedure, it is possible to write a very simple element using the engineering strain. The formulation, as well as the notation, is based on the work of Crisfield (1991) .

4.1.1 Truss implementation

Considering a straight bar with length L and cross section A loaded by an axial force q, according to the Hooke's law for elastic materials with linear stress/strain relation, the virtual work relationship using the engineering strain produces:

$$q = A\sigma_E = AE\frac{u}{l_0} = EA\bar{\varepsilon} \tag{4.1}$$

where $\bar{\varepsilon}$ is the engineering strain and it is assumed as a fixed value for the axial stiffness EA (Figure 4.1a).

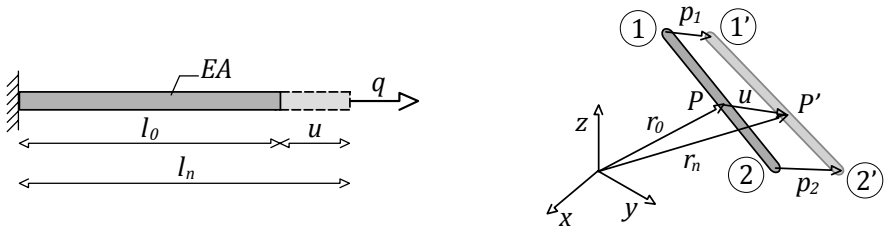

a) b)

Figure 4.1: Truss element: a) bar under axial load; b) deformation of the element.

Figure 4.1b shows the deformation process of a general truss element, where a point P in the reference configuration, identified by the position vector $\boldsymbol{r_0}$, moves into the current position P' defined by the vector $\boldsymbol{r_n}$:

$$\boldsymbol{r_n} = \boldsymbol{r_0} + \boldsymbol{u} \tag{4.2}$$

In the same way the nodal evolution during the deformation is:

$$\boldsymbol{x_n} = \boldsymbol{x_0} + \boldsymbol{p} \tag{4.3}$$

where the initial coordinates and the nodal displacements are:

$$\boldsymbol{x_o} = \{x_1, y_1, z_1, x_2, y_2, z_2\}^T \tag{4.4}$$

$$\boldsymbol{p} = \{u_1, v_1, w_1, u_2, v_2, w_2\}^T \tag{4.5}$$

Applying the corotational formulation, all the geometrical information, displacements and derivatives, are referred to a set of corotational axes which rotate with the element. Therefore, the engineering strain is given by:

$$\bar{\varepsilon} = \frac{1}{L_0}\begin{bmatrix}-1\\0\\0\\1\\0\\0\end{bmatrix}^T\begin{bmatrix}u_1\\v_1\\w_1\\u_2\\v_2\\w_2\end{bmatrix} = \frac{1}{L_0}\boldsymbol{c}_l^T\boldsymbol{p}_l \tag{4.6}$$

In the above equation the subscript l is related to the *local* corotated frame, and L_0 is the element length in the reference configuration. Applying (4.6) to the principle of virtual work, the corotated internal forces can be written as:

$$\boldsymbol{q}_{il} = \int \frac{\sigma}{L_0}\boldsymbol{c}_l \, dV_0 = A\sigma\boldsymbol{c}_l \tag{4.7}$$

In order to assemble all the internal forces of the whole domain, the transformation to a common reference system is necessary. Using the standard transformation matrix procedure we obtain:

$$\boldsymbol{q}_i = \boldsymbol{T}^T\boldsymbol{q}_{il} = A\sigma\boldsymbol{T}^T\boldsymbol{c}_l \tag{4.8}$$

where the transformation matrix is expressed in terms of the three unit vector establishing the corotational frame $\boldsymbol{e_1}$, $\boldsymbol{e_2}$, $\boldsymbol{e_3}$:

$$\boldsymbol{T} = \begin{bmatrix} e_{1x} & e_{2x} & e_{3x} & & & \\ e_{1y} & e_{2y} & e_{3y} & & \mathbf{0_3} & \\ e_{1z} & e_{2z} & e_{3z} & & & \\ & & & e_{1x} & e_{2x} & e_{3x} \\ & \mathbf{0_3} & & e_{1y} & e_{2y} & e_{3y} \\ & & & e_{1z} & e_{2z} & e_{3z} \end{bmatrix} \tag{4.9}$$

Looking to (4.9) and the definition of $\boldsymbol{c_l}$ in (4.6), it appears evident that there is no need to explicitly compute $\boldsymbol{e_2}$ and $\boldsymbol{e_3}$, so it is unimportant which assumption is used to build and update the frame (Crisfield 1997).

The local tangent stiffness matrix is obtained writing the variation of the internal forces (4.8) to give:

$$\delta \boldsymbol{q_i} = \delta \boldsymbol{T}^T \boldsymbol{q_{il}} = A\sigma \begin{bmatrix} -\delta e_{1x} \\ -\delta e_{1y} \\ -\delta e_{1z} \\ \delta e_{1x} \\ \delta e_{1y} \\ \delta e_{1z} \end{bmatrix} = A\sigma \begin{bmatrix} -\boldsymbol{I_3} \\ \boldsymbol{I_3} \end{bmatrix} \delta \boldsymbol{e_1} \tag{4.10}$$

where the Boolean matrix $\boldsymbol{F} = [-\boldsymbol{I_3}\,,\ \boldsymbol{I_3}]^T$ is composed by two identity matrices. The variation of the unit vector $\boldsymbol{e_1}$ related to the nodal increment $\delta \boldsymbol{p_{21}}$ can be written using the projection operator $\mathbb{P}_{e_1} = \left[\boldsymbol{I_3} - \boldsymbol{e_1 e_1^T}\right]$ which levels all the vector onto a plane orthogonal to $\boldsymbol{e_1}$ (Figure 4.2).

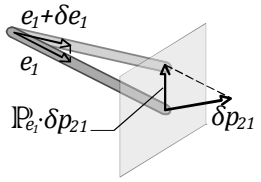

Figure 4.2: Orthogonal projection operator.

$$\delta \boldsymbol{e_1} = \frac{\partial \boldsymbol{e_1}}{\partial \boldsymbol{p_{21}}} = \frac{1}{L_n} \mathbb{P}_{e_1} \delta \boldsymbol{p_{21}} \tag{4.11}$$

Noting that $\delta \boldsymbol{p_{21}} = \boldsymbol{F}^T \delta \boldsymbol{p}$ (Crisfield 1991) and inserting (4.11) into (4.10), the tangent stiffness matrix is obtained:

$$\boldsymbol{K_t} = \frac{\partial \boldsymbol{q_i}}{\partial \boldsymbol{p}} = \frac{A\sigma}{L_n} [\boldsymbol{F}\boldsymbol{F}^T - (\boldsymbol{F}\boldsymbol{e_1})(\boldsymbol{F}\boldsymbol{e_1})^T] = \frac{A\sigma}{L_n} \left[\boldsymbol{A} - \frac{1}{L_n^2} \boldsymbol{c}(\boldsymbol{x}')\boldsymbol{c}(\boldsymbol{x}')^T\right] \tag{4.12}$$

4.1.2

Non-linear static and dynamic validation

In order to validate the implemented element, the main results of Kwan (2000) and Castellari et al. (2004) with their basic example are reproduced. In the beginning, it is recalled the basic assumption of the problem with the analytical solution, and it is subsequently presented the numerical comparison.

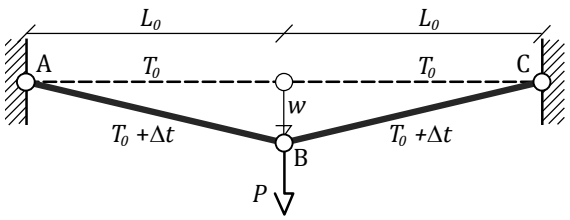

Figure 4.3: Symmetrical prestressed two-links structure.

Figure 4.3 shows the test example formed by two symmetric straight bars, restrained on nodes A and C, and free to move in the horizontal and vertical direction in the central node B. In the present tests the symmetry of the initial configuration is maintained in the elements' properties and loads. Thus, the system is completely described by the vertical displacement w resulting from external vertical force P on the central node. The bars are prestressed by the initial load T_0 and maintain the axial elastic stiffness EA throughout all the loading process. With the hypothesis of linear elastic material, referred to the engineering strain, the static deflection w, produced by P is given by the vertical equilibrium equation in the deformed configuration:

$$\frac{EA}{L_0^3} w^3 + \frac{2T_0}{L_0} w - P = 0 \tag{4.13}$$

where L_0 is the original undeformed length of the bars. All the detailed steps can be found in (Castellari, Lazzari and Saetta 2004).

The dynamic characteristic of the bars, in terms of period of oscillation of the central node, are obtained by imposing the kinetic equilibrium of the vertical forces of half-system ($P/2 + D - R = 0$). Considering a constant mass per unit length μ, the D'Alembert force for one element is given by:

$$D = \int_0^{L_0} \mu \left(\frac{x}{L_0} \ddot{w} \right) dx = \frac{\mu L_0}{2} \ddot{w} \tag{4.14}$$

While imposing momentum equilibrium of each cable with respect the central node, the vertical kinetic reaction at the support is obtained.

$$R \times L_0 = \int_0^{L_0} \mu \left(\frac{x}{L_0} \ddot{w} \right) (L_0 - x)\, dx \quad \rightarrow \quad R = \frac{\mu L_0}{6} \ddot{w} \tag{4.15}$$

Table 4.1: Truss validation. Test data.

cable axial stiffness	$EA = 556\ kN$
initial undeformed length	$L_0 = 1.143\ m$
mass per unit length	$\mu = 4.6415 \times 10^{-2}\ kg/m$
initial pretension	$t_0 = 3.5586\ kN$

Substituting (4.14) and (4.15) into the overall vertical equilibrium relationship leads to the equation of motion of the free undamped prestressed two-links:

$$\ddot{w} + \frac{3t_0}{\mu L_0^2} w + \frac{3}{2}\frac{EA}{\mu L_0^4} w^3 = 0 \tag{4.16}$$

In the case of concentrated mass M in the central node (*lumped system*) the previous equation becomes:

$$\ddot{w} + \frac{2t_0}{M L_0} w + \frac{EA}{M L_0^3} w^3 = 0 \tag{4.17}$$

According to the data of the example chosen by Kwan (2000) (see Figure 4.3), a static and a dynamic tests are made in order to validate the element formulation described in 4.1.2. Table 4.1 reports all the system information.

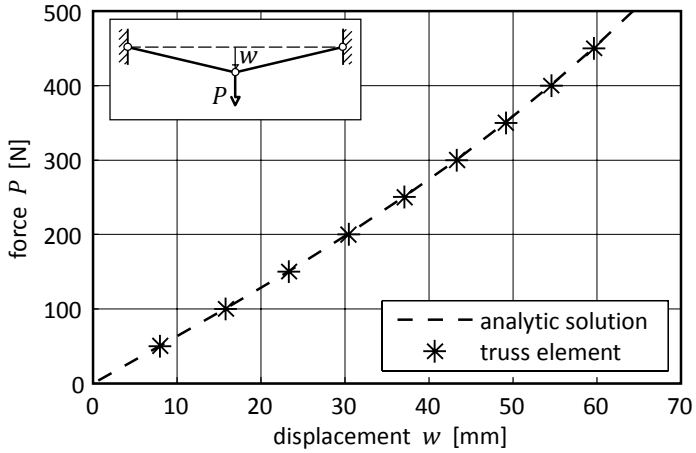

Figure 4.4: Truss validation. Non-linear static comparison.

Figure 4.4 shows the results of a non-linear static test, where the external point force P has been increased from 50 to $500\ N$ starting from the original straight configuration. It is

evident that the simulation with the finite element code Kratos, where the element has been implemented, perfectly reproduces the third order approximation of the solution (4.12) drawn here with the dashed line.

A second set of tests have been made comparing the non-linear dynamic behaviour of the element during a free oscillation. The tests aim to certify the good performance of the *truss* element as well as the Newmark's time integration scheme, implemented following (Bathe 1996). Figure 4.5 displays the results in terms of frequency ratios of a set of free oscillations starting from different initial displacements w_0. The frequencies f of the oscillations are related to the *natural frequency* of the system, i.e. the asymptotic frequency associated with infinitesimal amplitude. When $w \to 0$ the third order terms of (4.16), (4.17) are negligible, this means that the natural frequencies for consistent and lamped masses are:

$$f_n^{cons} = \frac{1}{2\pi}\sqrt{\frac{3t_0}{\mu L_0^2}} \qquad , \qquad f_n^{lump} = \frac{1}{2\pi}\sqrt{\frac{2t_0}{ML_0}} \tag{4.18}$$

The results reported in Figure 4.5 are related to a concentrated mass in the central node. In this test (see Table 4.1) the lamped mass is $M = 5.305 \times 10^{-2}\ kg$. The analytical solution has been found by solving (4.17).

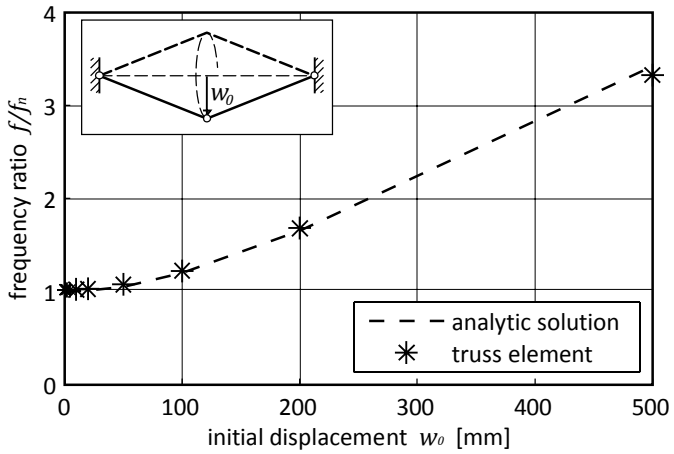

Figure 4.5: Truss validation. Non-linear dynamic comparison.

Figure 4.5 shows a perfect matching of the results for small initial displacements ($w_0 < 100\ mm$), while errors up to 3% appear for larger deflections. It should be noted

that for such values the hypothesis of small strains is not suitable anymore, thus either the numerical or the analytic solution can be hardly applied without considering special material non-linear features.

4.2 DKT PLATE ELEMENT

In this section an overview of the Discrete Kirchhoff Theory (DKT) triangular plate-bending element is reported. Particular attention is given to the concept with some remarks of the main features of this element and the implementation of the stiffness matrix. An extensive treatment of this formulation can be found in (Batoz, Bathe and Ho 1980) and (Pian and Tong 1969). The element have been found the most effective 9 degrees of freedom triangular element available for bending analysis of thin plates. Comparable results can be also obtained with the hybrid stress model (HSM) despite the first element is somewhat computational superior to the last one.

4.2.1 Plate element implementation

The element uses the *small displacement theory of plates* with the Kirchhoff hypothesis: 'points of the plate originally on the normal to the undeformed middle surface remain on straight line normal to the deformed middle surface'. With this assumption, the displacement components (u, v, w) of a point $P(x, y, z)$ are

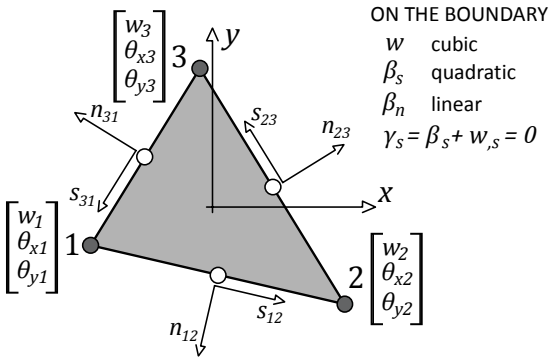

Figure 4.6: DKT triangular plate element. Geometry and degrees of freedom property.

$$u = z\beta_x(x, y), \quad v = z\beta_y(x, y), \quad w = w(x, y) \tag{4.19}$$

where w is the transversal displacement and the rotations of the normal are $\beta_x = -w_{,x}$ $\beta_y = -w_{,y}$ in the Kirchhoff plate theory (Gallagher 1975). Considering the bending strains linear through the thickness $\boldsymbol{\varepsilon_b} = z\boldsymbol{\kappa}$, where $\boldsymbol{\kappa} = \left[\beta_{x,x}\,;\beta_{y,y}\,;\,\beta_{x,y} + \beta_{y,x}\right]^T$ is the vector of curvatures, the strain energy is

$$U = \frac{1}{2}\int_A \boldsymbol{\kappa}^T \boldsymbol{E_b}\boldsymbol{\kappa}\, dx\, dy \tag{4.20}$$

For the present work, the case of isotropic homogeneous plates of constant thickness h leads to the simplest appearance of the elasticity matrix, that is

$$\boldsymbol{E_b} = \frac{Eh^3}{12(1-\nu^2)}\begin{bmatrix} 1 & \nu & 0 \\ \nu & 1 & 0 \\ 0 & 0 & \dfrac{1-\nu}{2} \end{bmatrix} \tag{4.21}$$

depending only to the Young's modulus E and the Poisson's ratio ν.

According to the formulation of the DKT element, special assumptions are made. Namely, it is assumed that the deflection w maintains a cubic variation along the sides of the triangle, while the rotations β_x and β_y vary quadratically over the element. The first statement is mathematically written by imposing the variation of the deflection in the mid-node k of side ij as:

$$w_{,sk} = -\frac{3}{2l_{ij}}w_i - \frac{1}{4}w_{,si} + \frac{3}{2l_{ij}}w_j - \frac{1}{4}w_{,sj} \tag{4.22}$$

The Kirchhoff hypothesis for thin plates is imposed along the sides, i.e.

$$\boldsymbol{\gamma} = \begin{bmatrix} \beta_x + w_{,x} \\ \beta_y + w_{,y} \end{bmatrix} = \mathbf{0} \qquad \text{at corners} \tag{4.23}$$

$$\beta_{sk} + w_{,sk} = 0 \qquad \text{at mid nodes} \tag{4.24}$$

Lastly, a linear variation of the rotation β_n (middle surface in $n-z$ plane) is imposed along the sides, i.e.:

$$\beta_{nk} = \frac{1}{2}\left(\beta_{ni} + \beta_{nj}\right) \qquad \text{at mid nodes} \tag{4.25}$$

All these assumptions guarantee that the Kirchhoff hypothesis is satisfied along the entire boundary ∂A (Figure 4.6).

In order to write an explicit form of the stiffness matrix, the expression of β_x and β_y in terms of the nodal dof $\boldsymbol{U} = \left[w_1\ \theta_{x1}\ \theta_{y1}\ w_2\ \theta_{x2}\ \theta_{y2}\ w_3\ \theta_{x3}\ \theta_{y3}\right]^T$ is needed. Using some simple geometrical relation to relate the n, s directions with x, y, and the parametric notation, Batoz et al. (1980) found:

$$\begin{aligned} \beta_x &= \boldsymbol{H_x^T}(\xi,\eta)\boldsymbol{U} \\ \beta_y &= \boldsymbol{H_y^T}(\xi,\eta)\boldsymbol{U} \end{aligned} \tag{4.26}$$

Hence, following the standard displacement formulation of the finite element method, the element curvature is written in terms of the nodal degrees of freedom by using the strain-displacement transformation matrix:

$$\boldsymbol{\kappa} = \boldsymbol{BU} \tag{4.27}$$

$$\boldsymbol{B}(\xi,\eta) = \frac{1}{2A}\begin{bmatrix} y_{31}H_{x,\xi}^T + y_{12}H_{x,\eta}^T \\ -x_{31}H_{y,\xi}^T - x_{12}H_{y,\eta}^T \\ y_{31}H_{x,\xi}^T + y_{12}H_{x,\eta}^T - x_{31}H_{y,\xi}^T - x_{12}H_{y,\eta}^T \end{bmatrix} \tag{4.28}$$

Finally, the stiffness matrix of the DKT element is:

$$\boldsymbol{K}_{DKT} = 2A\int_0^{-1}\int_0^{1-\eta} \boldsymbol{B^T E_b B}\, d\xi\, d\eta \tag{4.29}$$

The exact numerical integration of (4.29) is obtained using three integration points at the mid nodes. The last statement is suitable only for constant material properties and thickness over the whole element.

In a subsequent paper, Batoz (1982) makes explicit the expression of the stiffness matrix. With a rotated local coordinate system aligned to one side and using the decomposition presented in (Joseph and Rao 1979), it is possible to rewrite (4.29) without integration; obviously, maintain the condition of constant properties.

4.2.2

Experimental results for the plate element

The standard benchmark of a rectangular cantilever under a twist moment is presented. Figure 4.7 and Figure 4.8 show a rectangular plate, composed by two triangular elements, fully clamped on one side, twisted by a pair of forces on the opposite side. The two tests differ only for the mesh orientation. The figures plot the deflection w of one free corner for increasing length L of the cantilever. The comparison is made between the original DKT plate element (Batoz, Bathe and Ho 1980) drawn with the circle marks, the incompatible BCIZ1 element (Bazeley, et al. 1965) drawn with diamond marks, and the benchmark values obtained using 16 rectangular elements (Robinson 1978) drawn with the dashed line. The results obtained using the element implemented in this work of Thesis are plotted with the continuous line, which perfectly reproduces the original results obtained with the DKT element.

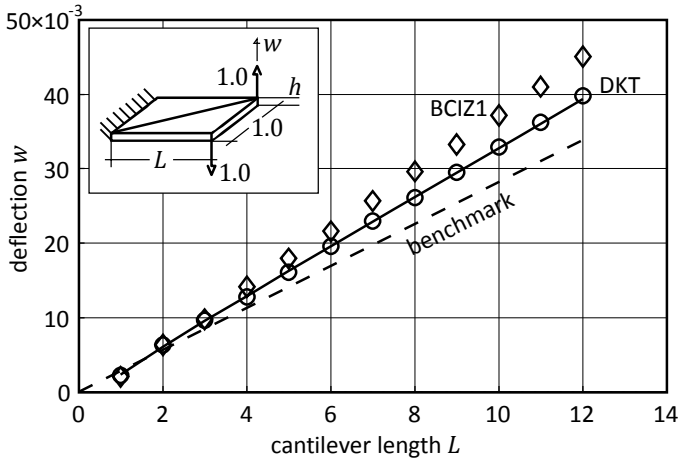

Figure 4.7: Plate validation. Cantilever under twist load. Mesh A.

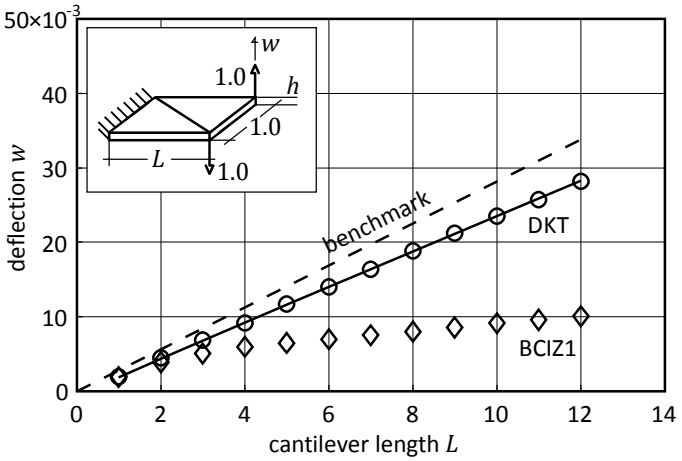

Figure 4.8: Plate validation. Cantilever under twist load. Mesh B.

4.3 OPT MEMBRANE TRIANGLE

The optimal (OPT) membrane triangle with drilling freedom is a 3 nodes plane triangle with 9 degrees of freedom studied by Felippa and co-workers in a student term project at the beginning of the 1990s (Felippa 2003). The main goal of the project was to build an "optimal" version of LST-3/9R (*linear strain triangle* with 3 nodes and 9 degrees of freedom including *rotations*) using the *direct fabrication approach*, with the ANDES template. The approach consists into the superposition of components (or multifield subspaces) of a finite element under suitable orthogonality conditions. Detail on this approach can be found in (Felippa 2000).

4.3.1 ANDES template

The ANDES (acronym for *assumed natural deviatoric strains*) is a variant of ANS formulation (Park and Stanley 1986) developed by Felippa and Militello (1991). In the framework, assumptions are made only in the *deviatoric* portion of the element strains; it is required that the integral over the element of that portion turns to zero. This assumption produces a splitting into the main portion of the strains which is left to be determined variationally from assumptions on the limit stress field, and the *high order* stiffness which include the deviatoric assumed strains.

Decomposition of the element stiffness matrix

Let $\boldsymbol{K}$ the element stiffness matrix, $\boldsymbol{u}$ the element degrees of freedom and $\boldsymbol{f}$ the corresponding element node forces. The procedure starts by splitting the stiffness matrix into the *basic* and *higher order* part:

$$\boldsymbol{K}\boldsymbol{u} = (\boldsymbol{K_b} + \boldsymbol{K_h})\boldsymbol{u} = \boldsymbol{f} \tag{4.30}$$

The basic stiffness matrix, which is usually rank deficient, is constructed for convergence; while the higher order stiffness matrix is constructed for stability and accuracy. A similar decomposition was first obtained by Bergan and Nygård (1984) in the derivation of the *free formulation* (FF), immediately applied in triangular membrane (Bergan and Felippa 1985) and plates elements (Felippa and Bergan 1987).

In his unified formulation, Felippa precises that $\boldsymbol{K}_b$ is formulation independent and it is entirely defined by an assumed constant stress state working on the element boundary displacements; no knowledge of the interior displacements field is necessary. The other term has the form $\boldsymbol{K}_h = \alpha \boldsymbol{K}_{h22}$ where α is a scaling factor.

Construction of the basic stiffness matrix $\boldsymbol{K}_b$ (from Box 2 in (Militello and Felippa 1991))

1. Assume a constant stress field $\overline{\boldsymbol{\sigma}}$ inside the element, than the associated boundary tractions are $\overline{\boldsymbol{\sigma}}_n = \overline{\boldsymbol{\sigma}} \cdot \boldsymbol{n}$, where $\boldsymbol{n}$ is the unit external normal on the element boundary S.
2. Assume the boundary displacement $\boldsymbol{d}$ over S; this field can be described by a standard interpolation of nodal freedoms: $\boldsymbol{d} = N_d \boldsymbol{u}$.
3. Construct the lumping matrix $\boldsymbol{L}$ that consistently assembles the boundary traction $\overline{\boldsymbol{\sigma}}_n$ into element node forces $\overline{\boldsymbol{f}}$ conjugate to $\boldsymbol{u}$ in the virtual work sense:

$$\overline{\boldsymbol{f}} = \int_S N_{dn}\, \overline{\boldsymbol{\sigma}}_n \, dS = \boldsymbol{L}\overline{\boldsymbol{\sigma}} \tag{4.31}$$

4. In the above, N_{dn} are boundary-system projection of N_d conjugate to the surface tractions $\overline{\boldsymbol{\sigma}}_n$.
5. The basic stiffness matrix is obtained as:

$$\boldsymbol{K}_b = \frac{1}{V}\boldsymbol{L}\boldsymbol{E}\boldsymbol{L}^T \tag{4.32}$$

6. where $\boldsymbol{E}$ is the stress-strain constitutive matrix of elastic muduli, which is assumed to be constant over the element volume V.

Construction of $\boldsymbol{K}_h$ by the ANDES formulation (from Box 3 in (Militello and Felippa 1991))

1. The first step is the selection of the *reference lines* where natural strain-gage locations are to be computed. By appropriate interpolation express the element natural strains $\boldsymbol{\epsilon}$ in terms of the strain gage readings $\boldsymbol{g}$ at those locations $\boldsymbol{\epsilon} = \boldsymbol{A}_\epsilon \boldsymbol{g}$, where the strain field in natural coordinates must include all constant strain states.
2. The relation between natural and Cartesian strains can be computed at each point using a projection tensor $\boldsymbol{\varepsilon} = \boldsymbol{T}\boldsymbol{\epsilon} = \boldsymbol{T}\boldsymbol{A}_\epsilon \boldsymbol{g} = \boldsymbol{A}\boldsymbol{g}$.
3. Relate the natural strain gage readings $\boldsymbol{g}$ to the node degrees of freedom $\boldsymbol{g} = \boldsymbol{Q}\boldsymbol{u}$, where Q is a strain gage to node displacement transformation matrix. There are several techniques to build such matrixes: the most simple is the direct interpolation over the reference lines.
4. Split the Cartesian strain field into mean (volume averaged) and deviatoric strains: $\boldsymbol{\varepsilon} = \bar{\boldsymbol{\varepsilon}} + \boldsymbol{\varepsilon}_d = (\bar{\boldsymbol{A}} + \boldsymbol{A}_d)\boldsymbol{g}$.
5. Assembling $\boldsymbol{A}_d$ and $\boldsymbol{Q}$ into a single strain displacement matrix $\boldsymbol{B}_d = \boldsymbol{A}_d \boldsymbol{Q}$, the higher order stiffness matrix is given by:

$$\boldsymbol{K}_h = \alpha \int_V \boldsymbol{B}_d^T \boldsymbol{E} \boldsymbol{B}_d \, dV \tag{4.33}$$

4.3.2

Membrane implementation

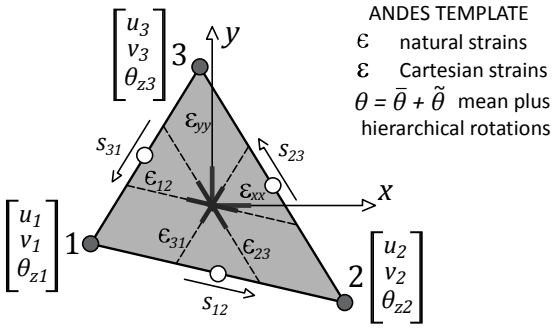

Figure 4.9: OPT triangular membrane element. Natural strains directions.

Following the ANDES template, in order to build the element, the first step is the definition of the *natural strains* directions. In agreement with the development of the DKT plate element (section 4.3) and as illustrated in Figure 4.9, the chosen strains follow the three sides. At each point of the triangle the natural strains vector is composed by the strains along the three directions:

$$\boldsymbol{\epsilon} = [\epsilon_{12} \quad \epsilon_{23} \quad \epsilon_{31}]^T \tag{4.34}$$

which is related to the Cartesian strains by the strain-gage transformation $\boldsymbol{\varepsilon} = \boldsymbol{T_e}\boldsymbol{\epsilon}$:

$$\begin{bmatrix} \varepsilon_{xx} \\ \varepsilon_{yy} \\ 2\varepsilon_{xy} \end{bmatrix} = \frac{1}{4A^2}\begin{bmatrix} y_{23}y_{13}l_{21}^2 & y_{31}y_{21}l_{23}^2 & y_{12}y_{32}l_{31}^2 \\ x_{23}x_{13}l_{21}^2 & x_{31}x_{21}l_{23}^2 & x_{12}x_{32}l_{31}^2 \\ (y_{23}x_{31}+x_{32}y_{13})l_{12}^2 & (y_{31}x_{12}+x_{13}y_{21})l_{23}^2 & (y_{12}x_{23}+x_{21}y_{32})l_{31}^2 \end{bmatrix}\begin{bmatrix} \epsilon_{12} \\ \epsilon_{23} \\ \epsilon_{31} \end{bmatrix} \tag{4.35}$$

Using the same transformation, the natural material matrix is defined by:

$$\boldsymbol{E_{nat}} = \boldsymbol{T_e^T}\,\boldsymbol{E_m}\,\boldsymbol{T_e} \tag{4.36}$$

where, recalling the same symbols of (4.21),

$$\boldsymbol{E_m} = \frac{Eh}{1-\nu^2}\begin{bmatrix} 1 & \nu & 0 \\ \nu & 1 & 0 \\ 0 & 0 & \dfrac{1-\nu}{2} \end{bmatrix} \tag{4.37}$$

According to the *direct fabrication* approach, the element stiffness matrix is decomposed into *basic* $\boldsymbol{K_b}$ and *high order* $\boldsymbol{K_h}$ parts, which are simply added to obtain the result. The basic stiffness takes care of consistency, while the high order takes care of stability and accuracy. To fulfil correctly the template, the two parts should be two orthogonal subspaces.

The explicit expression of the *basic stiffness matrix* (4.32) is published in (Bergan and Felippa 1985) where *force-lumping matrix* is expressed is (4.38). The choice of the parameter α_b depends on specific element formulation. Particularly when $\alpha_b = 0$ the basic stiffness (4.32) becomes the total stiffness matrix of the CST-3/6C, in which the drilling rotations vanish. Other special cases are the OPT: $\alpha_b = 3/2$, and the retrofitting LST with $\alpha_b = 4/3$. In these cases and with constant thickness and isotropic material, the matrix $\boldsymbol{L}$ can also be directly related to the mean strain-displacement matrix $\boldsymbol{B_0} = \boldsymbol{L}^T/V$.

$$\boldsymbol{L} = \frac{h}{2}\begin{bmatrix} y_{23} & 0 & x_{32} \\ 0 & x_{32} & y_{23} \\ \frac{\alpha_b}{6} y_{23}(y_{13}-y_{21}) & \frac{\alpha_b}{6} x_{32}(x_{31}-x_{12}) & \frac{\alpha_b}{6}(x_{31}y_{13}-x_{12}y_{21}) \\ y_{31} & 0 & x_{13} \\ 0 & x_{13} & y_{31} \\ \frac{\alpha_b}{6} y_{31}(y_{21}-y_{32}) & \frac{\alpha_b}{6} x_{13}(x_{12}-x_{32}) & \frac{\alpha_b}{6}(x_{12}y_{21}-x_{23}y_{32}) \\ y_{12} & 0 & x_{21} \\ 0 & x_{21} & y_{12} \\ \frac{\alpha_b}{6} y_{12}(y_{32}-y_{13}) & \frac{\alpha_b}{6} x_{21}(x_{23}-x_{31}) & \frac{\alpha_b}{6}(x_{23}y_{32}-x_{31}y_{13}) \end{bmatrix} \tag{4.38}$$

The high order matrix is obtained by the higher order stiffness $\boldsymbol{K_\theta}$ in terms of the hierarchical rotation $\widetilde{\boldsymbol{\theta}}$ rotated by the transformation matrix $\widetilde{\boldsymbol{T}}_{\boldsymbol{\theta u}}$, times a scaling factor:

$$\boldsymbol{K}_h = \frac{3}{4}\beta_0\, \widetilde{\boldsymbol{T}}_{\boldsymbol{\theta u}}^{\boldsymbol{T}}\, \boldsymbol{K_\theta}\, \widetilde{\boldsymbol{T}}_{\boldsymbol{\theta u}} \tag{4.39}$$

For isotropic materials, the optimality leads to $\beta_0 = \frac{1}{2}(1-4\nu^2)$. The transformation matrix is necessary to relate the final stiffness to the three corner dofs $\widetilde{\boldsymbol{\theta}} = \widetilde{\boldsymbol{T}}_{\boldsymbol{\theta u}}\boldsymbol{u_R}$:

$$\widetilde{\boldsymbol{\theta}} = \frac{1}{4A}\begin{bmatrix} x_{32} & y_{32} & 4A & x_{13} & y_{13} & 0 & x_{21} & y_{21} & 0 \\ x_{32} & y_{32} & 0 & x_{13} & y_{13} & 4A & x_{21} & x_{21} & 0 \\ x_{32} & y_{32} & 0 & x_{13} & y_{13} & 0 & x_{21} & y_{21} & 4A \end{bmatrix}\begin{bmatrix} u_1 \\ v_1 \\ \theta_{z1} \\ u_2 \\ v_2 \\ \theta_{z2} \\ u_3 \\ v_3 \\ \theta_{z3} \end{bmatrix} \tag{4.40}$$

$\boldsymbol{K_\theta}$ includes the deviatoric natural strain patterns, that means the change from constant states. A complete derivation is reported in the Appendix A of (Felippa 2003).

$$\boldsymbol{K}_\theta = Ah\left(\boldsymbol{Q}_{\boldsymbol{12}}^{\boldsymbol{T}}\boldsymbol{E_{nat}}\boldsymbol{Q_{12}} + \boldsymbol{Q}_{\boldsymbol{23}}^{\boldsymbol{T}}\boldsymbol{E_{nat}}\boldsymbol{Q_{23}} + \boldsymbol{Q}_{\boldsymbol{31}}^{\boldsymbol{T}}\boldsymbol{E_{nat}}\boldsymbol{Q_{31}}\right) \tag{4.41}$$

Matrices $\boldsymbol{Q_i}$ relates the natural strains to the deviatoric rotations following the relation $\boldsymbol{\epsilon} = \boldsymbol{Q}\widetilde{\boldsymbol{\theta}}$.

Applying a linear interpolation over the nodal values, $\boldsymbol{Q} = \boldsymbol{Q_1}\xi_1 + \boldsymbol{Q_2}\xi_2 + \boldsymbol{Q_3}\xi_3$ and evaluating the previous at the midpoints:

$$\begin{aligned} \boldsymbol{Q_{12}} &= \frac{1}{2}(\boldsymbol{Q_1} + \boldsymbol{Q_2}) \\ \boldsymbol{Q_{23}} &= \frac{1}{2}(\boldsymbol{Q_2} + \boldsymbol{Q_3}) \\ \boldsymbol{Q_{31}} &= \frac{1}{2}(\boldsymbol{Q_3} + \boldsymbol{Q_1}) \end{aligned} \tag{4.42}$$

where the corner matrices are written as function of 9 dimensionless parameters. For the OPT triangle, the parameters values are: $\beta_1 \to \beta_9 = [1, 2, 1, 0, 1, -1, -1, -1, -2]$.

$$\boldsymbol{Q_1} = \frac{2A}{3}\begin{bmatrix} \frac{\beta_1}{l_{12}^2} & \frac{\beta_2}{l_{12}^2} & \frac{\beta_3}{l_{12}^2} \\ \frac{\beta_4}{l_{23}^2} & \frac{\beta_5}{l_{23}^2} & \frac{\beta_5}{l_{23}^2} \\ \frac{\beta_7}{l_{31}^2} & \frac{\beta_8}{l_{31}^2} & \frac{\beta_9}{l_{31}^2} \end{bmatrix} \tag{4.43}$$

$$\boldsymbol{Q_2} = \frac{2A}{3}\begin{bmatrix} \frac{\beta_9}{l_{12}^2} & \frac{\beta_7}{l_{12}^2} & \frac{\beta_8}{l_{12}^2} \\ \frac{\beta_3}{l_{23}^2} & \frac{\beta_1}{l_{23}^2} & \frac{\beta_2}{l_{23}^2} \\ \frac{\beta_6}{l_{31}^2} & \frac{\beta_4}{l_{31}^2} & \frac{\beta_5}{l_{31}^2} \end{bmatrix} \tag{4.44}$$

$$\boldsymbol{Q_3} = \frac{2A}{3}\begin{bmatrix} \frac{\beta_5}{l_{12}^2} & \frac{\beta_6}{l_{12}^2} & \frac{\beta_4}{l_{12}^2} \\ \frac{\beta_8}{l_{23}^2} & \frac{\beta_9}{l_{23}^2} & \frac{\beta_7}{l_{23}^2} \\ \frac{\beta_2}{l_{31}^2} & \frac{\beta_3}{l_{31}^2} & \frac{\beta_1}{l_{31}^2} \end{bmatrix} \tag{4.45}$$

4.3.3

Membrane numerical results

The membrane part of the shell element is tested according to the benchmark proposed firstly by Cook (1974). In the test, a non-rectangular quadrilateral element, clamped on

one side, is skewed by unitary load ($P = 1.0$) distributed over the whole left side. The test data, as well as the results are given in Figure 4.10. The comparison is made between three elements obtained with the proposed template:

- CST (*constant strain triangle*), $\alpha_b = 0$,
- LST-Ret (*retrofitting linear strain triangle*), $\alpha_b = 4/3$,
- OPT (*optimal membrane triangle*), $\alpha_b = 3/2$,
- OPT+DKT (*presented formulation*).

The implemented element differs from the OPT only because it already includes the bending part of the shell.

Results show the same trend of the three high order elements, while the simple CST requires a finer mesh to reach acceptable results. It should be noted that the LST-Ret requires one drilling freedom to be fixed, otherwise the stiffness matrix turns singular, and there is no analytical solution for the test: it can be only said that the asymptote of all elements is $v_C = 23.956$.

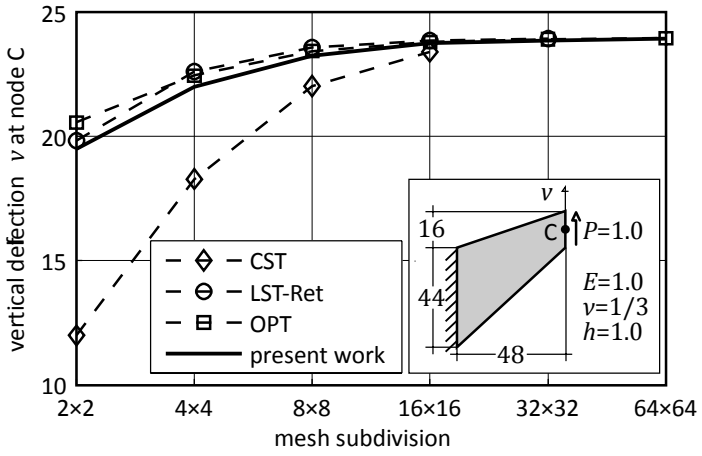

Figure 4.10: Membrane validation. Non-rectangular cantilever under skewed load.

4.4 SHELL ELEMENT

Developing shell elements is one of the greatest issues in Finite Element Analysis. A huge amount of papers have been published on this subject (see the review in (Zienkiewicz and

Taylor 2005)), but mainly three approaches can be identified for the creation of these elements:

1. a particular bi-dimensional shell theory is used (*classical shell theory*);
2. three-dimensional continuum equations are used and discretised (*degenerated solid approach*);
3. plate bending and membrane element stiffness are superimposed and assembled in a global coordinate system.

Although the hypothesis underlying the classical shell theory and the degenerated solid approach are the same, the reduction to resultant form is usually carried out analytically in the first choice and numerically in the latter (Belytschko, Liu and Moran 2000). The degenerated solid approach was pioneered by Ahmad, Irons and Zienkiewicz (1970); a non linear version of the theory was offered By Hughes and Liu (1981), while the generalisation of the classical shell theory, extensively exposed in (Fung and Sechler 1974), is recently risen again thanking Simo and Fox (1989), (1990) who, starting from the mathematical basis of the Cosserat (1909) and the Rodrigues' rotation tensor, build a geometrical exact shell element for large rotations.

The third method has gained great attention for the linear analysis in the 1960s and recently has come back as the most popular when combined with the corotational theory (Felippa and Haugen 2005), or used to define macro-elements (patch) taking advantage of the simplest flat elements (Oñate and Flores 2005). The derivation of flat elements is simpler and computationally more efficient than the curved ones. The triangular shell element presented and used in this study is obtained by the superposition of the DKT plate element (section 4.2) and the OPT membrane element (section 4.3) following the indication and some clever suggestions of Khosravi et al. (2007).

4.4.1

Material stiffness matrix

Coupling the membrane and the bending part, the strain-displacement relationship becomes:

$$\begin{bmatrix} \boldsymbol{\varepsilon_m} \\ \boldsymbol{\varepsilon_b} \end{bmatrix} = \begin{bmatrix} \boldsymbol{B_m} & \mathbf{0} \\ \mathbf{0} & \boldsymbol{B_b} \end{bmatrix} \begin{bmatrix} \boldsymbol{d_m} \\ \boldsymbol{d_b} \end{bmatrix} = \boldsymbol{B_0} \begin{bmatrix} \boldsymbol{d_m} \\ \boldsymbol{d_b} \end{bmatrix} \tag{4.46}$$

where the 18 element degrees of freedom have been rearranged in order to maintain the two parts disconnected. In (4.46) the total strain-displacement matrix is composed by the

bending part $\boldsymbol{B_b}$ taken from (4.27) and the membrane part $\boldsymbol{B_m}$. In order to write a unique matrix, the basic and higher order matrices of the OPT are merged into:

$$\boldsymbol{B_m} = \underbrace{\frac{1}{V}\boldsymbol{L^T}}_{basic} + \underbrace{\frac{3}{2}\sqrt{\beta_0}\boldsymbol{T_e}(\boldsymbol{Q_1}\xi_1 + \boldsymbol{Q_2}\xi_2 + \boldsymbol{Q_3}\xi_3)\widetilde{\boldsymbol{T}}_{\boldsymbol{\theta u}}}_{higher\ order} \tag{4.47}$$

Relations (4.46) and (4.47) show the advantage of using two simple flat elements, thus the mix terms turn to be zero. Another important note is that the OPT is an *energetically orthogonal element*, then the integral of the higher order strains over the domain is zero.

For isotropic material and constant thickness, the material matrix $\boldsymbol{D_0}$ and therefore the material stiffness matrix $\boldsymbol{K_0}$ follows the same appearance of $\boldsymbol{B_0}$. Thus:

$$\boldsymbol{D_0} = \begin{bmatrix} \boldsymbol{E_m} & \boldsymbol{0} \\ \boldsymbol{0} & \boldsymbol{E_b} \end{bmatrix} \tag{4.48}$$

Recalling (4.21) and (4.37):

$$\boldsymbol{K_0} = \int_A \boldsymbol{B_0^T D_0 B_0}\, dA = \begin{bmatrix} \boldsymbol{K_m} & \boldsymbol{0} \\ \boldsymbol{0} & \boldsymbol{K_b} \end{bmatrix} \tag{4.49}$$

In the implemented code, the stiffness matrix is arranged to keep track the normally sorted nodal degrees of freedom $\boldsymbol{d} = \left[u_1, v_1, w_1, \theta_{x1}, \theta_{y1}, \theta_{z1}, \dots\right]^T$; this is made multiplying (4.49) by a indices matrix: $\boldsymbol{K_0^{arraged}} = \boldsymbol{I^T}\, \boldsymbol{K_0}\, \boldsymbol{I}$.

4.4.2

Geometric stiffness matrix

The *tangent stiffness* matrix in a non-linear code is composed by the *material stiffness* and the *geometric stiffness*, also called *stress stiffness*. The latter takes into account the work done by the internal forces in the deformed configuration. In this framework only the membrane forces $\left[N_x, N_y, N_{xy}\right]$ are considered making such a work, while the bending moments are neglected (Belytschko, Liu and Moran 2000). The work is calculated as constant membrane forces acting through the strains; thus the strain energy stored into the element is:

$$U = U_L + U_\sigma = \int_A [\varepsilon_x \quad \varepsilon_y \quad \gamma_{xy}] \begin{bmatrix} N_x \\ N_y \\ N_{xy} \end{bmatrix} dA \tag{4.50}$$

In the previous equation the membrane strains associated with the deflections u, v, w are written following the Green-Lagrange strains:

$$\begin{bmatrix} \varepsilon_x \\ \varepsilon_y \\ \gamma_{xy} \end{bmatrix} = \begin{bmatrix} (u_{,x}) + \frac{1}{2}(u_{,x}^2 + v_{,x}^2 + w_{,x}^2) \\ (v_{,y}) + \frac{1}{2}(u_{,y}^2 + v_{,y}^2 + w_{,y}^2) \\ (u_{,y} + v_{,x}) + \frac{1}{2}(u_{,x}u_{,y} + v_{,x}v_{,y} + w_{,x}w_{,y}) \end{bmatrix} \tag{4.51}$$

The initial terms in (4.51) are the engineering strains and, multiplied by the axial forces, produce the linear work U_L; while the geometric part of the work U_σ, related to the stress stiffness $\boldsymbol{K_\sigma}$, arises from the high order strain terms:

$$U_\sigma = \frac{1}{2}\int_A \begin{bmatrix} u_{,x} \\ u_{,y} \\ v_{,x} \\ v_{,y} \\ w_{,x} \\ w_{,y} \end{bmatrix}^T \begin{bmatrix} N_x & N_{xy} & \mathbf{0_2} & \mathbf{0_2} \\ N_{xy} & N_y & & \\ \mathbf{0_2} & & N_x & N_{xy} \\ & & N_{xy} & N_y \\ \mathbf{0_2} & & \mathbf{0_2} & \begin{matrix} N_x & N_{xy} \\ N_{xy} & N_y \end{matrix} \end{bmatrix} \begin{bmatrix} u_{,x} \\ u_{,y} \\ v_{,x} \\ v_{,y} \\ w_{,x} \\ w_{,y} \end{bmatrix} dA \tag{4.52}$$

where $\mathbf{0_2}$ is a zeros 2×2 matrix.

Since the formulations of both DKT plate bending and OPT membrane elements are based on the assumptions on strains, there are no explicit definition of the internal displacements u, v and w. The solution adopted by Khosravi et al. (2007) is to use the shape functions of other elements with the same degrees of freedom. Particularly the BCIZ plate bending (Bazeley, et al. 1965) and LST-Ret membrane elements (Felippa 2003) have the same degrees of freedom corresponding with DKT and OPT elements. The adopted shape functions are give in (4.56), (4.57) and (4.58).

Using (4.56), (4.57) and (4.58), it is possible to make explicit the derivatives of the displacement functions needed in (4.52) by invoking inverse of Jacobian matrix of isoparametric elements:

$$\boldsymbol{u}_{,x} = \boldsymbol{J}_t^{-1}\boldsymbol{G}\begin{bmatrix}\boldsymbol{d_m}\\ \boldsymbol{d_b}\end{bmatrix} \tag{4.53}$$

where the Jacobian and the derivatives of shape functions are considered as function of ξ_2 and ξ_3, imposing $\xi_1 = 1 - \xi_2 - \xi_3$.

$$\boldsymbol{J}_t^{-1} = \begin{bmatrix}\boldsymbol{J^{-1}} & \boldsymbol{0_2} & \boldsymbol{0_2}\\ \boldsymbol{0_2} & \boldsymbol{J^{-1}} & \boldsymbol{0_2}\\ \boldsymbol{0_2} & \boldsymbol{0_2} & \boldsymbol{J^{-1}}\end{bmatrix} \quad \text{with} \quad \boldsymbol{J} = \begin{bmatrix}x_{,\xi_2} & y_{,\xi_2}\\ x_{,\xi_3} & y_{,\xi_3}\end{bmatrix} \tag{4.54}$$

$$\boldsymbol{G} = \begin{bmatrix} N^u_{1,\xi_2} & 2\cdots 8 & N^u_{9,\xi_2} & 0 & \cdots & 0\\ N^u_{1,\xi_3} & 2\cdots 8 & N^u_{9,\xi_3} & 0 & \cdots & 0\\ N^v_{1,\xi_2} & 2\cdots 8 & N^v_{9,\xi_2} & 0 & \cdots & 0\\ N^v_{1,\xi_3} & 2\cdots 8 & N^v_{9,\xi_3} & 0 & \cdots & 0\\ 0 & \cdots & 0 & N^w_{1,\xi_2} & 2\cdots 8 & N^w_{9,\xi_2}\\ 0 & \cdots & 0 & N^w_{1,\xi_3} & 2\cdots 8 & N^w_{9,\xi_3}\end{bmatrix} \tag{4.55}$$

$$u = \begin{bmatrix} \xi_1\\ 0\\ \frac{\alpha_b}{2}\xi_1(y_{12}\xi_2 - y_{31}\xi_3)\\ \xi_2\\ 0\\ \frac{\alpha_b}{2}\xi_2(y_{23}\xi_3 - y_{23}\xi_1)\\ \xi_3\\ 0\\ \frac{\alpha_b}{2}\xi_3(y_{31}\xi_1 - y_{23}\xi_2)\end{bmatrix}^T \begin{bmatrix} u_1\\ v_1\\ \theta_{z1}\\ u_2\\ v_2\\ \theta_{z2}\\ u_3\\ v_3\\ \theta_{z3}\end{bmatrix} = \boldsymbol{N^u}\,\boldsymbol{d_m} \tag{4.56}$$

$$v = \begin{bmatrix} 0\\ \xi_1\\ \frac{\alpha_b}{2}\xi_1(x_{21}\xi_2 - x_{13}\xi_3)\\ 0\\ \xi_2\\ \frac{\alpha_b}{2}\xi_2(x_{32}\xi_3 - x_{32}\xi_1)\\ 0\\ \xi_3\\ \frac{\alpha_b}{2}\xi_3(x_{13}\xi_1 - x_{32}\xi_2)\end{bmatrix}^T \begin{bmatrix} u_1\\ v_1\\ \theta_{z1}\\ u_2\\ v_2\\ \theta_{z2}\\ u_3\\ v_3\\ \theta_{z3}\end{bmatrix} = \boldsymbol{N^v}\,\boldsymbol{d_m} \tag{4.57}$$

$$w = \begin{bmatrix} \xi_1^2(3-2\xi_1)+2\xi_1\xi_2\xi_3 \\ -\xi_1^2(y_{12}\xi_2+y_{13}\xi_3)-\frac{1}{2}(y_{12}+y_{13})\xi_1\xi_2\xi_3 \\ \xi_1^2(x_{12}\xi_2+x_{13}\xi_3)+\frac{1}{2}(x_{12}+x_{13})\xi_1\xi_2\xi_3 \\ \xi_2^2(3-2\xi_2)+2\xi_1\xi_2\xi_3 \\ -\xi_2^2(y_{23}\xi_3+y_{21}\xi_1)-\frac{1}{2}(y_{23}+y_{21})\xi_1\xi_2\xi_3 \\ \xi_2^2(x_{23}\xi_3+x_{21}\xi_1)+\frac{1}{2}(x_{23}+x_{21})\xi_1\xi_2\xi_3 \\ \xi_3^2(3-2\xi_3)+2\xi_1\xi_2\xi_3 \\ -\xi_3^2(y_{31}\xi_1+y_{32}\xi_2)-\frac{1}{2}(y_{31}+y_{32})\xi_1\xi_2\xi_3 \\ \xi_3^2(x_{31}\xi_1+x_{32}\xi_2)+\frac{1}{2}(x_{31}+x_{32})\xi_1\xi_2\xi_3 \end{bmatrix}^T \begin{bmatrix} w_1 \\ \theta_{x1} \\ \theta_{y1} \\ w_2 \\ \theta_{x2} \\ \theta_{y2} \\ w_3 \\ \theta_{x3} \\ \theta_{y3} \end{bmatrix} = \boldsymbol{N^w}\,\boldsymbol{d_b} \tag{4.58}$$

The final expression for the geometric stiffness matrix is:

$$\boldsymbol{K_\sigma} = 2A \int_A \boldsymbol{G^T J^{-T}}\,\widetilde{\boldsymbol{N}}\,\boldsymbol{J^{-1}G}\; d\xi_2 d\xi_3 \tag{4.59}$$

where $\widetilde{\boldsymbol{N}}$ is the 6×6 matrix taken from (4.52). The expression of $\boldsymbol{K_\sigma}$ given in (4.59) corresponds to the separated sets of nodal displacements $[\boldsymbol{d_m},\ \boldsymbol{d_b}]^{\boldsymbol{T}}$; the matrix implemented into the code is rearranged in the same way of (4.49).

4.5 FEM ANALYSIS

Several authors have studied the evolution in the design of the stadium's roof adjusting step by step the assumptions and, after various experimental tests, the final input data for the FEM analysis were carried out. The numerical model used in the present work is quite simple but very sensitive to some parameters which have been tested until the convergence of the results. The cables are modelled with geometrically non-linear rod elements implemented using the Total Lagrangian formulation (Crisfield 1991) explained in section 4.1. The material behaviour is assumed linear elastic following the constructor's specifications (Tensoteci). The two concrete slabs are reproduced using corotational shell elements (see section 4.4), which allow small deformations in relation to the rotated configuration. Details on the used elements can be found following the studies of Professors Felippa

(2003), Bathe (Batoz, Bathe and Ho 1980) and Ganesan (Khosravi, Ganesan and Sedaghati 2007). The third component is identified by the border steel girders, which are modelled for reproducing accurately the real structure using standard truss elements. In order to read all the following results in a correct way, some considerations on the adopted scheme have been specified.

After the total application of the dead loads, a stable configuration is the first important goal to reach, because the almost entirety of the structural stiffness is provided by the cables and in the way they are placed. Later on it will be referred on this first reference configuration by the name "*state 0*". The builders installed all the wires set without special pretension more than the needed value to bear their self weight, varying the length to facilitate the required slope in the across-the-cable direction ($\approx 1\%$) to permit the drainage of rainwater. This particular feature implies a drawback because, varying the lengths with the same plane span ($212\ m$), different initial arch heights result and this implies a variable stiffness on the wires set. In this way the roof is narrowly asymmetric across-the -cables direction, that is not so relevant in terms of displacements but more significant as stiffness distribution. On the valley side, the North side, the cables are more stretched and less stiffed; hence, it is expected that structure crisis starts from this side.

The numerical model is created drawing wires with parabolic initial geometry, as an approximation of the catenary, with maximum height variable form $4.2\ m$ to $7.2\ m$ form valley to the quarry. The dead load has smoothed this difference in level to the final slope from $7.0\ m$ to $8.0\ m$ in the *state 0*.

The slabs were built by assembling several concrete panels in situ (Figure 2.2d) and, after the positioning, the two covers have been merged into two continuous solids. These steps have to be taken into account during the analysis because the shell elements are jointed together in the same nodes since the very beginning of the simulation. This distinctiveness makes uncertain the determination of uniform material law attribution for the concrete, in particular the value for the elastic modulus E_{con}^{d} which should vary in a range of $0 \div 32.8\ GPa$ corresponding to divided panels and to perfect continuity respectively. The comparison between several analyses with different modulus' values in the way to reach the state 0 configuration are summarized in Table 4.2, where the low sensitivity of the system on this parameter appears.

The connection between the slabs and the cables is realized using ring-type joints that fix the lateral and vertical displacements while allows the along-the-cable relative movement. Building the numerical model, the first trial was made inserting an ordinary Master-Slave constraint in the model fixing the relative nodes' displacement $\Delta Y - \Delta Z$ and leaving release the displacement ΔX. The directions are referred to the global reference system

where X is the main cable directions, positive from East to West; Y is the across-the-cable direction, positive from North to South; while Z is the upward vertical direction. It must be noted that those links are not equivalent to the real joints, in fact the true free path is in the tangent of the cable direction and not in the projection to the horizontal. This approximation inserts a little locking but the relative stiffness of the shells is small in reference to the cables stiffness, thus this effect does not appear. The maximum relative ΔX from slabs' nodes to the correspondent wires' nodes remains near $16\ cm$ with all the concrete elastic modulus. Subsequently an improved model has been used, substituting all the links with small truss elements, $30\ cm$ long, with modified mechanical parameters to better simulate the real connection.

Table 4.2: *State 0* configuration varying the slab's elastic modulus

E/E_d	$d_{max}^{valley}\ [m]$	$d_{max}^{quarry}\ [m]$	$\Delta X_{max}^{slip}\ [cm]$	$T_{max}\ [kN]$	$M_{xx}^{slab}\ [kNm]$	$M_{yy}^{slab}\ [kNm]$
1/100	6.99	7.98	16.10	6830	1.36	1.31
1/50	6.98	7.97	16.00	6820	2.61	2.00
1/20	6.98	7.96	15.90	6820	6.40	3.18
1/10	6.98	7.96	15.90	6810	15.48	4.49
1/5	7.00	7.97	16.00	6810	24.90	6.61
1/2	7.03	7.98	16.00	6840	62.60	13.50
1	7.07	8.01	16.00	6890	119.50	23.04

Table 4.2 reports some characteristic values of the dead load configuration (*state 0*) calculated with different trials where only the value of the concrete elastic modulus has been varied. The measure of E_{con} is expressed as a ratio with respect to the design value for concrete class C30/37 (EN 206-1): $E_{con}^{d} = 32.8\ GPa$. In the columns, the maximum vertical displacements of the slabs are reported with a range $d_{max}^{valley} \div d_{max}^{quarry}$ corresponding to the values taken on the North (the valley) and on the South (quarry) side of the Stadium. The almost 1 meter of difference between the range is due to the drainage of the water toward the quarry (see section 2.1). The fourth column shows the maximum slip ΔX_{max}^{slip} between cables and slabs: the slip test aim to evaluate the quality of the joints estimating a possible additional damping due to the friction of the two materials. On the fifth column the maximum axial force in a pair of cables is reported; the most excited cables are always in the valley side because they are the straightest for geometrical conditions.

From the exposed results, it appears evident that the stiffness of the slabs, expressed in terms of their Young modulus, does not change the final loaded configuration; in this preliminary step the slabs' self weight is the major load. The last two columns highlight the bending moment values on the slabs in both the principal directions. The amount of external forces which load on the shells grows increasing the elements' stiffness as a reflection on common physical structural behaviour. It is obvious that the panels cannot be melted until the *state 0* is not reached, so the trials with the higher E are not truthful. In the present work, the slabs are inserted in the numerical model with two continuous sur-

faces with constant elastic modulus $E_{con} = 656\ MPa$, equal to $1/50$ of the design value. This hypothesis is only used to get to the reference configuration, while for the service loads, like the wind load, an increased value is restored.

4.6 FREQUENCY CONTROL

In reference to the mechanical features on the *state 0* configuration, the value of the concrete elastic modulus on the complete and homogeneous roof is still decisive for the dynamic characterization of the structure. Even if it has been demonstrated on Table 4.2 that this value is not worthy for the static configuration, it will be shown that this parameter greatly modifies the natural frequency and, sometimes, even the modal shapes.

A sensitivity analysis of the concrete Young modulus is referred around the theoretical value for undamaged concrete C30/37: $E_{con}^{d} = 32.8\ GPa$, a safeguard Code value that includes some coefficients to protect against the uncertainties. Starting from this reference, many linear eigenvalue analyses with different elastic modulus values have been carried out covering a wide open windows of trials: $0 < E_{con} < 2\ E_{con}^{d}$. The terms of comparisons are the natural frequencies and the modal shapes, trying to find the best fitting to the identified results of the experimental tests (Figure 2.6). It is interesting noting that in different trials the order of the modal shape can change.

Figure 4.11 to 14 show four trials resulted from the corresponding linear eigenvalue problem starting from the *state 0* configuration. On different trials, all but the slab modulus value remains constant. In different trials the modulus value is respectively set on $\{10\%\,;50\%\,;100\%\,;150\%\}\ E^{d}$. This great variability is necessary for the uncommon construction process which provides to join together the slabs' panels with a concrete casting in a very flexible support that is the set of 34 pairs of cables at $40\ m$ with respect the ground level. Recent visual surveys pointed out a lot of cracks and damages on the cover surfaces, just a few years after the construction. The main results of different tests are summarized in the Table 4.3, which takes the identified natural frequencies from the ambient test as sample.

The first two natural vibration modes involve the cylindrical behaviour of the roof, so basically the cables stiffness; due to that reason every trial is able to find the suitable profile. By the way, the frequency check shows that best calibration between masses and stiffness is obtained for very low elasticity modulus values, around $10\%\ E^{d}$. However, this first result does not find evidences on the further modes. On the contrary, the lowest values of E sets all the eigenvectors in a wrong order, and moreover they emphasize local instabilities

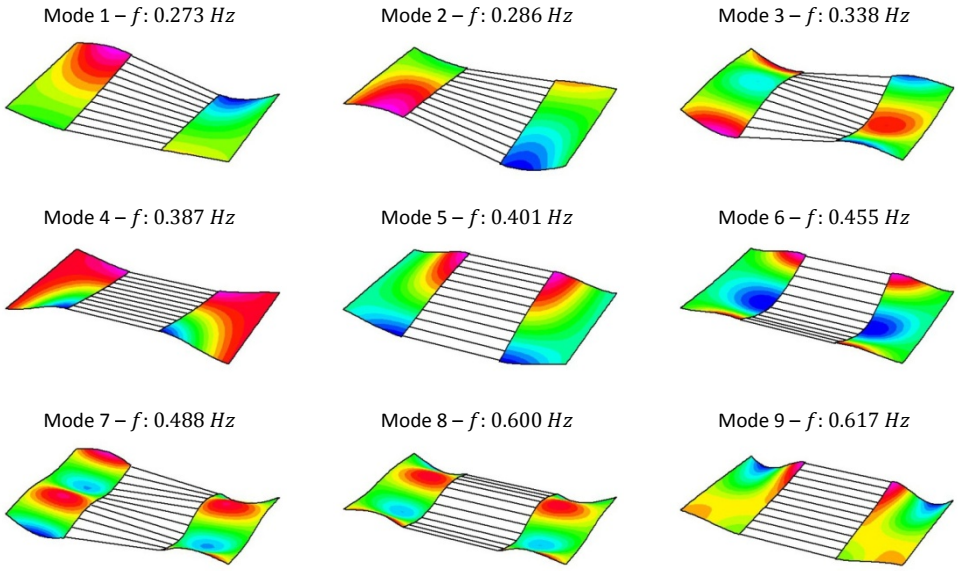

Figure 4.11: Natural vibration modes according to the *State 0* configuration. Slabs elastic modulus $E = 3.3\ GPa$.

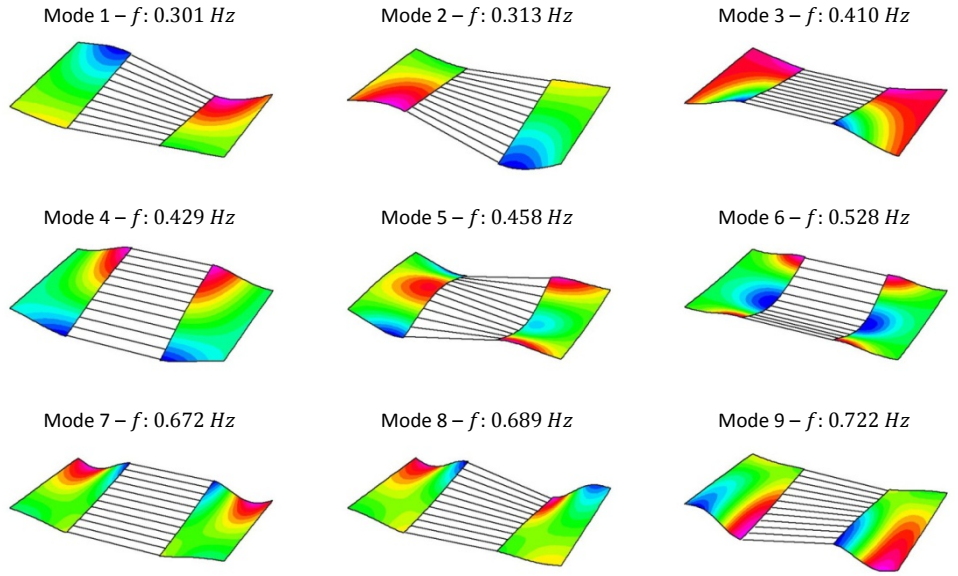

Figure 4.12: Natural vibration modes according to the *State 0* configuration. Slabs elastic modulus $E = 16.4\ GPa$.

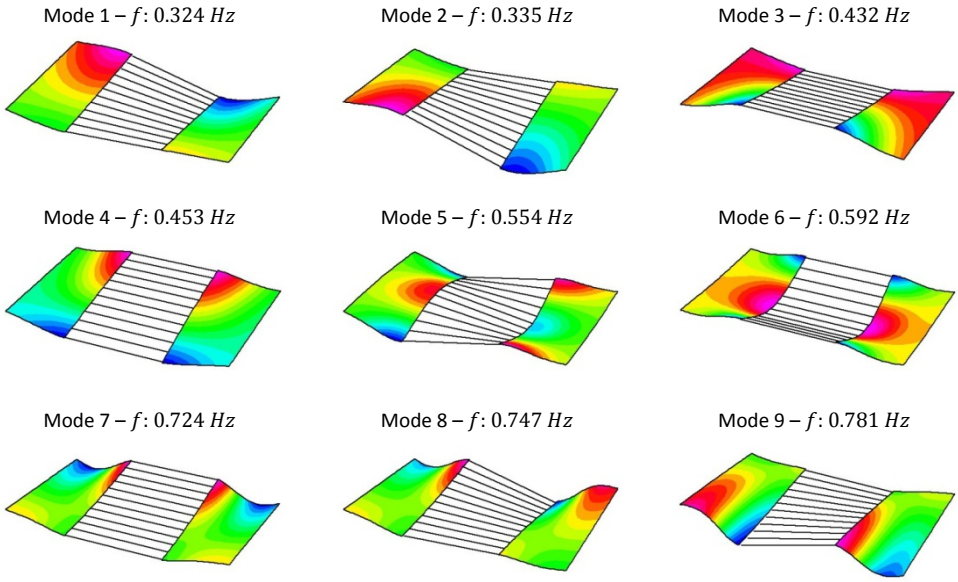

Figure 4.13: Natural vibration modes according to the *State 0* configuration. Slabs elastic modulus $E = 32.8\ GPa$.

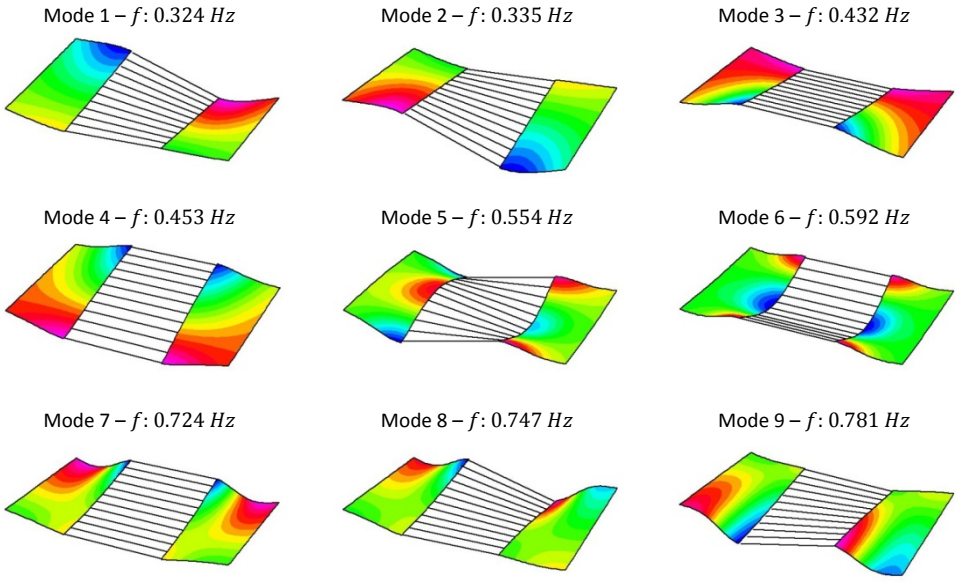

Figure 4.14: Natural vibration modes according to the *State 0* configuration. Slabs elastic modulus $E = 49.2\ GPa$.

Table 4.3: Frequencies (Hz) comparison between different slabs stiffness.

mode	Identified	$E = 3.3\ GPa$	$E = 16.4\ GPa$	$E = 32.8\ GPa$	$E = 49.2\ GPa$
1	0.275	0.273	0.301	0.324	0.339
2	0.293	0.286	0.313	0.335	0.350
3	0.525	0.338	0.410	0.432	0.448
4	0.537	0.387	0.429	0.453	0.471
5	0.562	0.401	0.458	0.554	0.623
6	0.635	0.455	0.528	0.592	0.644
7	0.653	0.488	0.672	0.724	0.766
8	0.702	0.600	0.689	0.747	0.795
9	0.737	0.617	0.722	0.781	0.828

evolving on the slabs as it is shown in Figure 4.11 modes 7-8. All the other trials are able to reach the correct order on the modal shapes proofed by the full scale tests (see section 2.2), with slightly differences on the frequency values. It can be also noted that the 5th and 6th modal shapes which stressed the transversal stiffness of the structure, which means involving only the slabs, are well approximated with the full theoretical value or even greater. The last three shapes affect the stiffness in both directions; they are better fitted with intermediate value around $50\%\ E^d$.

Concluding it seems evident that the two slabs do not have an homogeneous behaviour in both the principal directions; the huge cylindrical flexibility has produced many transversal cracks with the consequential stiffness reduction $E_{slab}^{long} \cong (0.1 \div 0.2)E^d$, while on the other direction the concrete's mechanical characteristics seem been remained unchanged $E_{slab}^{trasv} \cong (1.0 \div 1.2)E^d$.

4.7 NUMERICAL RESONANCE TESTS

The preliminary models are successfully used to characterise mechanically and geometrically the roof, moreover the results of standard linear eigenvalue analysis around the reference configuration former shown allow focussing into a deeper investigations on a restricted windows of frequencies. With all the available data, newer enhanced models are created in order to develop complete non-linear dynamic analyses aimed to accurately reproduce the full scale test carried out in the last years. The analyses are performed implementing several subroutines in the open source code Kratos (KRATOS) developed by the group of Prof. Oñate among the CIMNE in Barcelona (CIMNE). The code allows interacting with every step of the solving process with pleasant features in the performance of complex load time histories.

The first numerical tests reproduce the resonance load experiments carried out by the Prof. Majowiecky's team on the built-up structure (Cosentino and Majowiecki 2004). The

two tests (see section 2.2) apply an oscillating force using an unbalance motor on the corner and mid-span points of the west slab: respectively EXCA, EXCB (see Figure 2.3), varying the applied loading frequency in order to excite all the structural frequencies of the stadium's roof. The structural responses were caught and reported by six accelerometers on the two edges of the slabs. The load is applied in the numerical simulations with a bell-shape distribution of pressure (Figure 4.15a,c) on the selected loaded points; in this way several singularities are avoided and the convergence of the solution is improved.

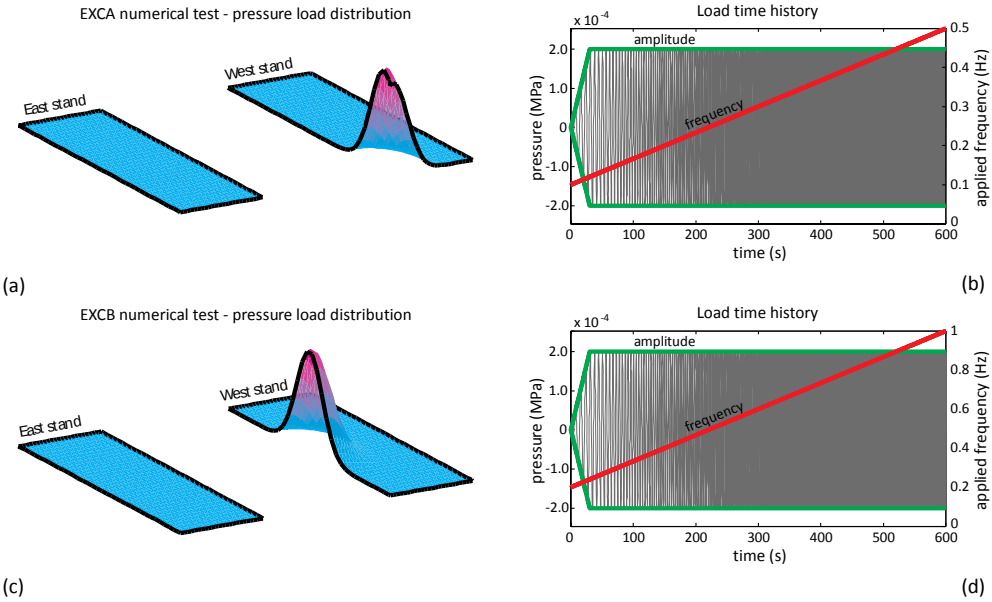

Figure 4.15: Numerical test load on points EXCA, EXCB: a-c) pressure distribution; b-d) complete time history of the loads.

The exciting pressure follows the formulae:

$$p(t) = A \sin\left(2\pi \bar{f} \cdot t\right) \tag{A.1}$$

where the amplitude A is linear increasing for the first 30 seconds of simulation up to the maximum value $2 \cdot 10^{-4}\ MPa$, the value is referred to the top of the bell; while the applied frequency $\bar{f}$ is constantly increasing from 0.1 to $0.5\ Hz$ during test EXCA and from 0.2 to $1.0\ Hz$ during the second trial (see Figure 4.15b,d). The simulations are both $10\ min$ long.

After the solution by numerical simulations, a complete characterisation of the results is possible. The following sections show the modal shapes with relevant identified frequencies pointed out by the orthogonal decomposition of the vertical displacements of the two

slabs. It is worthy to highlight that the applied loads are nil mean, in this way numerical fakes are avoided (see section 3.1).

The modes pointed out on Figure 4.16 and Figure 4.20 are compared with those experimentally identified showed in Figure 2.6; the comparisons are specified in the third column in the summary tables. Other figures show the power spectra and the time histories of the maximum displacements. It can be noted from the displacement graphs that each modes remain frozen until the approach of the applied load frequency to the natural frequency of the mode $\bar{f} = f_k$. Besides, it is evident that energetically higher modes boost higher peak displacements. The energy ratio distribution is reported on the second column of the summary tables.

4.7.1

Results with load on EXC A

In the first test the load is applied on the North corner of the West slab. The intent is to stimulate asymmetrical deformations of the roof, in particular the first two modes where concrete slabs stiffness is less significant.

Table 4.4: Summary of the results in resonance numerical test on point EXC A.

Mode	Energy ratio	Mode shape type	Frequencies recognized
1	46.82%	2	0.277
2	34.53%	3	0.380
3	8.63%	5	0.433 ; 0.277 ; 0.262
4	5.43%	6	0.505 ; 0.393 ; 0.380
5	1.26%	4	0.393 ; 0.505
6	1.01%	9	0.637 ; 0.733

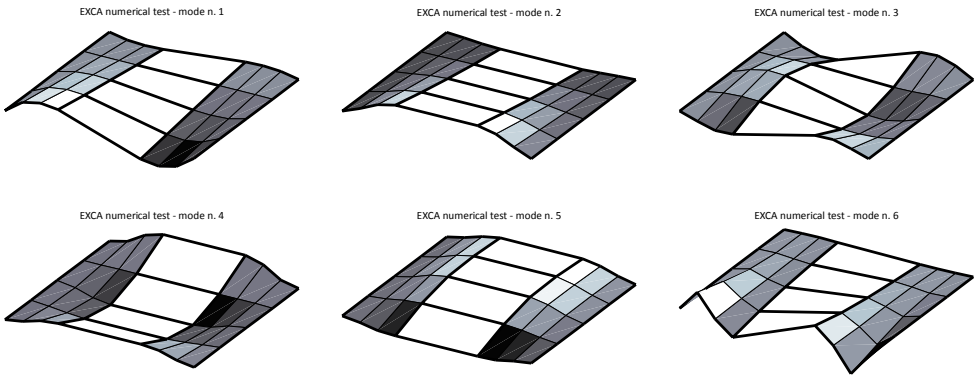

Figure 4.16: Modes resulting from numerical test EXC A.

The energetic comparison between modes shows a high predominance of the first two of them, as a sign of the correct procedure in the test development. The recognized modes have shape similar to the second and third in Figure 2.6, while the first and fourth are missing; this aspect is easily explained noting that the load (Figure 4.15a) is applied on the same corner that boosts the modes 3 and 4. It can be demonstrated that loading the other corner of the same slab the other two modal shapes will be awaken. The other pointed out modes of this trial have very low energy, but still the procedure is able to reproduce the correct frequencies (see also test B).

Figure 4.17 depicts the displacement and the awaken frequencies of the loaded corner of the west grandstand resulting from the simulation. The maximum deflection is about half a meter.

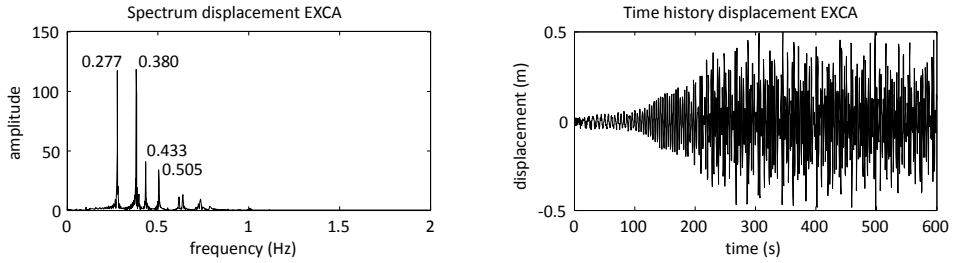

Figure 4.17: Power spectra and displacement time history of point A

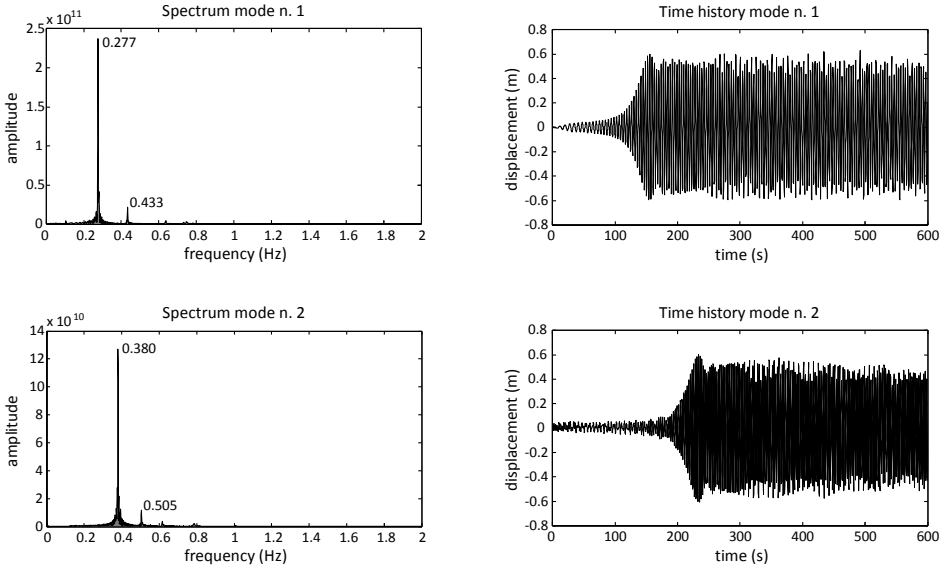

Figure 4.18: Power spectra and displacements on numerical test EXC A. Modes 1, 2.

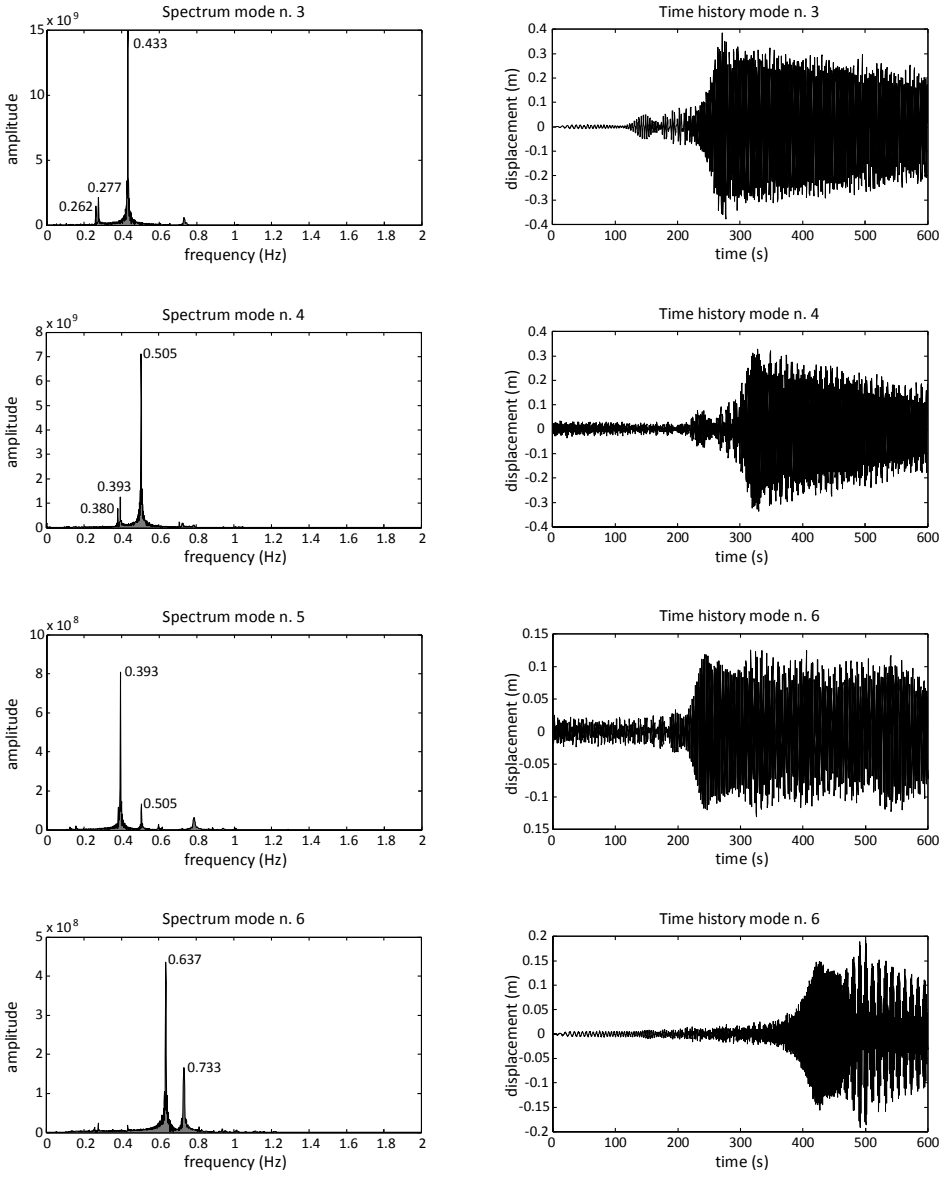

Figure 4.19: Power spectra and displacements on numerical test EXC A. Modes 3, 4, 5, 6.

Figure 4.18-19 show the first six modes of the test EXC A. As already mentioned, the n-mode is highlighted only when the load frequency approach the n^{th} natural frequency. The reducing displacement amplitude depicted at the end of the graphs is not an effect of some external dissipation device, but is due to the shifting in the load frequency.

4.7.2

Results with load on EXC B

The second test is carried out applying the resonance load in the mid span of the west slab (see Figure 4.15c). Being the complementary trial with respect EXC A, in this case the symmetric modal shapes are stimulated.

Table 4.5: Summary of the results in resonance numerical test on point EXC B.

Mode	Energy ratio	Mode shape type	Frequencies recognized
1	24.62%	5	0.433 ; 0.277 ; 0.263
2	18.75%	1,2	0.277 ; 0.263 ; 0.433
3	17.96%	3,4,6	0.505 ; 0.393 ; 0.380
4	17.63%	3,4	0.393 ; 0.380 ; 0.505
5	9.34%	1,2,5	0.263 ; 0.277 ; 0.433
6	8.49%	3,4,6	0.505 ; 0.380 ; 0.393

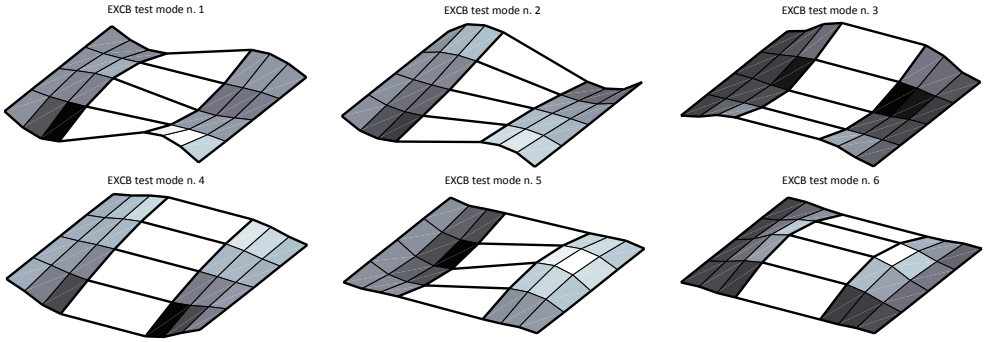

Figure 4.20: Modes resulting from numerical test EXC B.

Table 4.5 and Figure 4.20 give the same information of the corresponding Table 4.4 and Figure 4.16 of the previous test. In this case the most energetic modes are the symmetric ones, which are stiffer: the latter consideration makes clear the reduction to almost $0.2\ m$ of the maximum deflection as depicted in Figure 4.21. However, comparing Figure 4.17 and 4.21 it must be considered that the graphs measure different points.

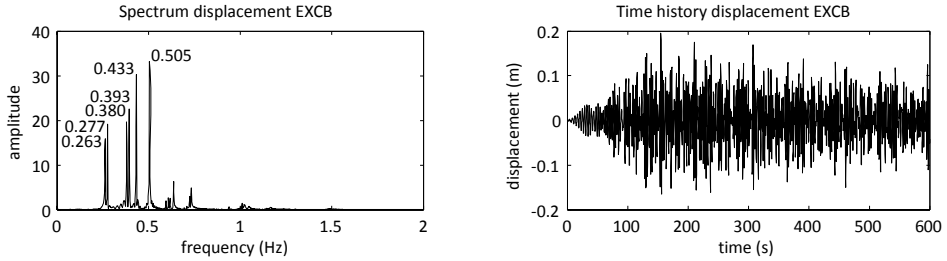

Figure 4.21: Power spectra and displacements of point B

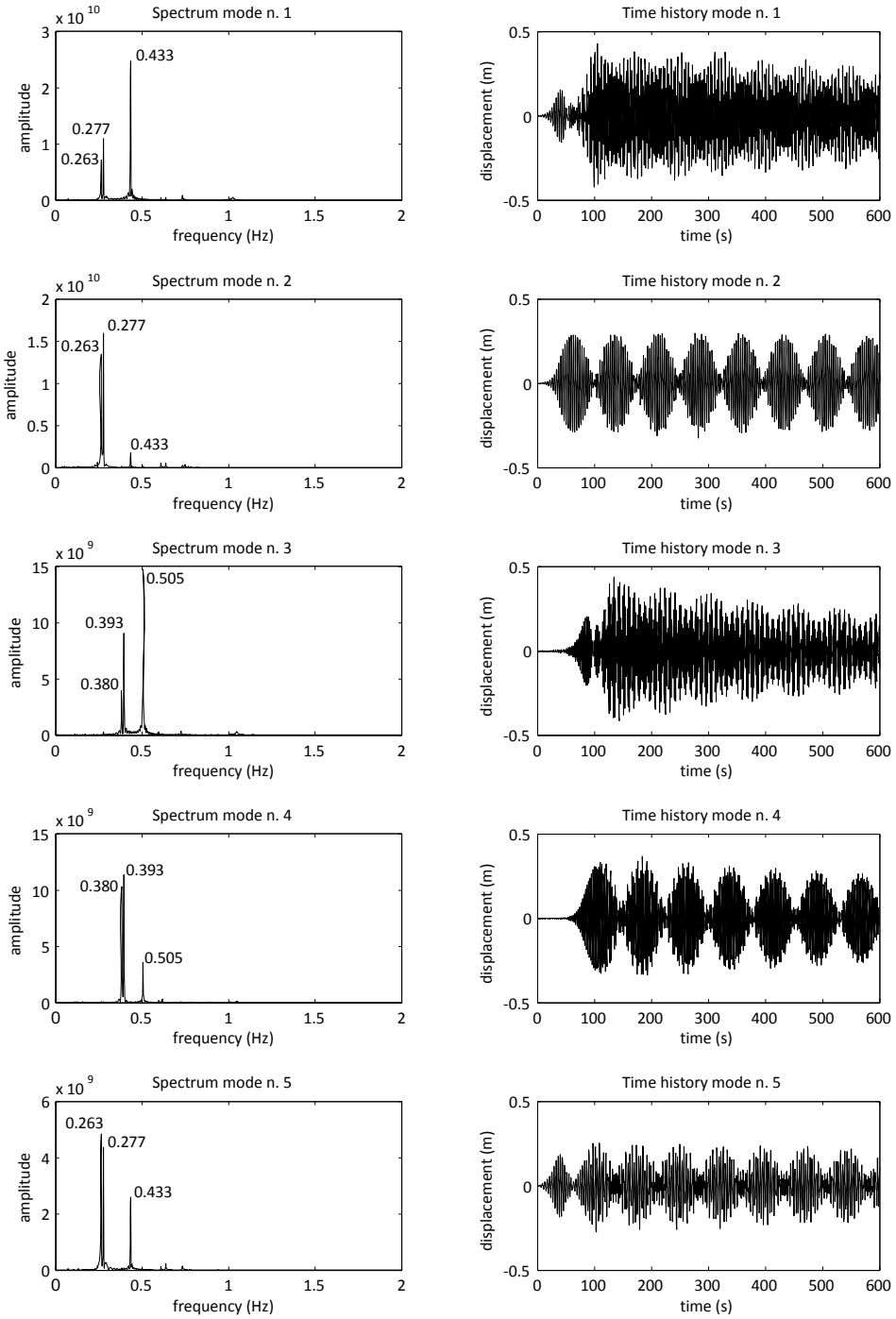

Figure 4.22: Power spectra and displacements on numerical test EXC B. Modes 1 to 5.

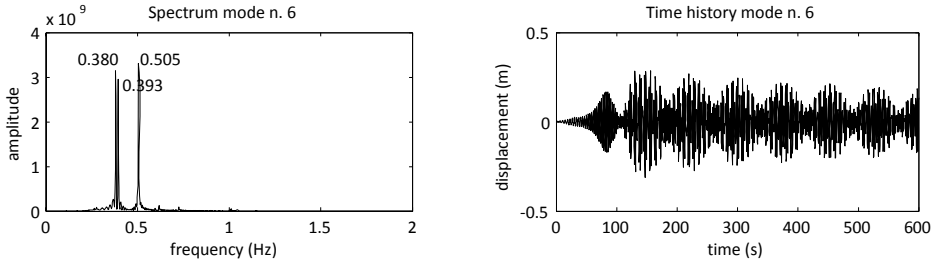

Figure 4.23: Power spectra and displacements on numerical test EXC B. Mode 6.

In this trial the energetic ratios are quite spread between the first six modes (Figure 4.22-4.23) and, in contrast with EXC A test, the first two couple are correctly identified jointly (1-2, 3-4) with slight differences in the frequencies due to the non perfect symmetry of the structure in the across the cable direction.

Resuming, the two numerical dynamic tests allow us to carefully characterise the natural frequencies of the model (Table 4.6) considering all the geometrical non linearity. All this data, including the little gaps in comparison to the full scale characterisation, have to be taken as a reference on the evaluation of following results in chapter 6.

Table 4.6: Dynamic characterization of the non-linear numerical model of the roof.

mode	1	2	3	4	5	6
$f\ (Hz)$	0.263	0.277	0.380	0.393	0.433	0.505
$\omega\ (rad/s)$	1.652	1.740	2.388	2.469	2.721	3.173
$T\ (s)$	3.802	3.610	2.632	2.545	2.309	1.980

CHAPTER 5

DAMPING IN STRUCTURES

The importance of damping is becoming increasingly significant as buildings are becoming taller and more flexible. Modern high-rise buildings designed to satisfy lateral drift requirements still may oscillate excessively during wind storms. The level of these oscillations may be not significant enough to cause structural damage, but may cause discomfort to the building occupants, i.e. it may exceed the serviceability limit states. Damping in engineering structures is, however, the most uncertain parameter in the prediction of the dynamic response if compared with the elastic and inertial ones. There are two principal reasons for this: the variety of mechanisms contributing to damping and the rarity of reliable data on damping characteristics of different structures. Concerning the former, the sources of damping of structures are various and not well understood; the task of finding a suitable model and its associated damping forces is a continuous concern in engineering research. The latter reason refers to the additional uncertainties introduced by the analysis and interpretation of data of full scale structural tests. Any accurate information concerning the damping values, at the design stage, may certainly alleviate a major source of uncertainty routinely experienced by designers of wind sensitive structures.

In this section, problems regarding the structural aerodynamics and the evaluation of damping coefficients are presented.

5.1 STRUCTURAL DAMPING

Structural damping is a measure of energy dissipation in a vibrating structure that results in bringing it to a stillness state. The damping capacity is defined as the ratio of the energy dissipated in one cycle of oscillation to the maximum amount of energy accumulated in the structure in that cycle (Letchford, et al. 2002). There are as many damping mecha-

nisms as there are modes of converting mechanical energy into heat: among the major there are *material damping*, *friction damping* and *soil-structure interaction*. Material damping dissipates energy by micro-cracking within the structural matrix of the material. Friction damping refers to damping caused by relative movement of structural components, such as movement within bolted connections (Gaul and Nitsche 2001), or relative motion between structural frameworks and internal partitions in buildings. Damping from soil-solid interaction depends on both the foundation type and the underlying soil characteristics (Gazetas and Mylonakis 1998).

The material damping contribution comes from a complex molecular interaction within the material, thus the damping is dependent on the type of material, method of manufacturing and final finishing processes. The complexity of the situation is further enhanced by the simple reality that material properties often differ from sample to sample, resulting possibly in significant differences in energy losses among distinct members of a structural system. The equation of motion in structural dynamics usually describes a macroscopic behaviour, while material damping processes arise from microscopic phenomena. This conflict in the scales leads to a search for phenomenological theories for the representation of structural damping (Yuan 2002). The interfacial damping mechanism is the Coulomb friction between members and connections of a structural system, and between structural components like partitions and exterior facade. Welded connections tend to reduce the contribution of interfacial damping as compared to the bolted connections. Soil-structure interaction also contributes towards the overall damping depending on the soil characteristics.

In order to avoid all these uncertainties in the damping design stage, in engineering practice an equivalent viscous damping model is used for the sake of simplicity as it lends to a linear equation of motion. This applies to mechanical systems subject to slow motion in both liquids and gases, such as shock absorbers, sliding bearings and tune mass damper, for instance. The viscous damping coefficient is either assigned on the basis of the construction material, e.g. steel or concrete, or it is evaluated using a system identification technique. A logarithmic decrement of a free vibration test is one such approach. Any source of nonlinearity is obscured in this approach and consequences of such an assumed model are either ignored or disregarded. This concept has been extended to represent equivalent viscous damping, whereby the energy dissipated by a nonlinear system in a steady-state vibration is equated to the energy dissipated by an equivalent viscous system (Pekcan, Mander and Chen 1999).

In contrast, Coulomb damping or dry friction arises through the motion of a body along a dry surface. In this case, the friction which is otherwise constant depends to a large extent upon the contact pressure and the friction coefficients. This type of friction can also occur

in compression joints (e.g. bolts and rivets). It is the internal friction within the material itself which generates structural or hysteretic damping. The damping force arising at the joints may be also included in this model. The resulting forces depend in the main on the strains or displacements in the structure. The term "hysteretic damping" (Inaudi and Kelly 1995) trunks from the consideration that these damping effects can be deduced experimentally from the hysteresis perceptible in a load-displacement diagram of a body subject to harmonic excitation. When the material is of the linear-elastic type, the damping forces are assumed to be proportional to the elastic forces and point in the opposite direction to the velocity.

Some of the commonly used damping models can be described by

$$f_d(x,\dot{x}) = a\dot{x}|\dot{x}|^{\theta-1} \tag{5.1}$$

where $f_d(x,\dot{x})$ is the damping force, x, $\dot{x}$ are the position and its first derivative and a is the damping coefficient; the value of θ determines the damping model (Argyris and Mlejnek 1991).

Table 5.1: Damping models

Damping model		damping force	damp. ratio	
Linear viscous damping	$\theta = 1$	$f_d = c\dot{x}$	$\xi = \frac{c}{2m\omega}$	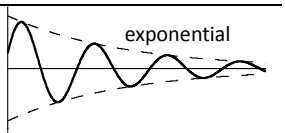
Coulomb damping	$\theta = 0$	$f_d = \mu\,\mathrm{sign}(\dot{x})$	$\xi = \frac{2\mu}{\pi m\omega^2 A}$	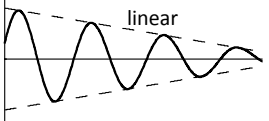
Quadratic damping	$\theta = 2$	$f_d = q\dot{x}\|\dot{x}\|$	$\xi = \frac{4qA}{3\pi m}$	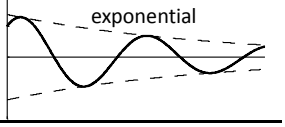

Table 5.1 shows some typical damping models: c, q and μ are the linear viscous, quadratic and Coulomb damping coefficients respectively, m, ω are the mass and the circular frequency respectively while A is the amplitude of the motion.

It is important to note that the linear viscous damping ratio is independent of amplitude, whereas Coulomb and quadratic damping ratios are respectively inversely and directly proportional to amplitude of motion. For narrowly damped systems, where all three preceding damping mechanisms may coexist, a first order approximation for the total damp-

ing of the system can be obtained by fitting data to (5.1). Such a model may bring out useful information regarding the inherent damping mechanisms in a system which experiences different types of damping sources.

5.1.1 Rayleigh Damping

None of the damping models mentioned above offers an exact description of damping in engineering structures, excluding a small number of buildings provided with a finite number of damping devices where real viscous dynamic properties can be measured. In most cases, different models of damping should be applied simultaneously. Consequently, designers are led to substitute an equivalent viscous damping model in place of rather complex damping mechanisms. However, the substituting model should ensure the same amount of dissipation as in the original damping mechanism.

The most used form of damping in the mathematical model for dynamic response of a structure is proportional to the stiffness and mass of the structure. This is referred to as *Rayleigh* damping (Clough and Penzien 1993). Both modal and Rayleigh damping are used in order to avoid the need to form a damping matrix based on the physical properties of the real structure.

$$c = a_0 m + a_1 k \tag{5.2}$$

$$\xi_n = \frac{a_0}{2\omega_n} + \frac{a_1 \omega_n}{2} \tag{5.3}$$

Equations (5.2) and (5.3) report the expression of the damping coefficient c (or matrix in multidimensional systems) and the relation between damping ratio ξ and circular frequency ω. The latter is shown graphically in Figure 5.1.

It is to note that the two Rayleigh damping factors, a_0 and a_1, can be evaluated by the solution of a pair of simultaneous equations if the damping ratios ξ_m and ξ_n associated when two specific circular frequencies ω_m, ω_n are known. Usually, due to a lack of detailed information about the variation of damping ratio with frequency, it is assumed that the same damping ratio coefficient applies to both control frequencies, i.e. $\xi_m \equiv \xi_n = \xi$. Accordingly, (5.4) gives the mass and stiffness proportionality factors that satisfy (5.3) with a unique frequency.

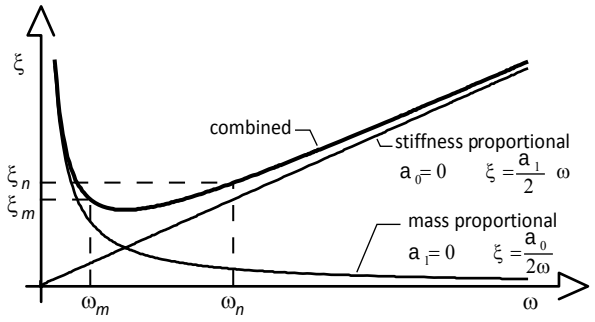

Figure 5.1: Rayleigh damping: damping ratio vs frequency.

$$\begin{Bmatrix} a_0 \\ a_1 \end{Bmatrix} = \frac{2\xi}{\omega_m + \omega_n} \begin{Bmatrix} \omega_m \omega_n \\ 1 \end{Bmatrix} \tag{5.4}$$

Applying the latter proportional damping matrix derivation procedure in practice, it is recommended that ω_m should be taken as the fundamental frequency of the multi-degrees of freedom system and that ω_n is set among the higher frequencies of the modes that contribute significantly to the dynamic response. The derivation ensures that the desired damping ratio is obtained for these two modes; then as shown by Figure 5.1, modes with frequencies between these two specified frequencies will have somewhat lower values of damping ratio, while all modes with frequencies greater than ω_n will have damping ratios that increase above ξ_n monotonically with frequency. The final results of this situation ensure that the responses of very high frequency modes are effectively eliminated by their high damping ratios.

5.2 AERODYNAMIC DAMPING

In addition to structural damping, some structures exhibit significant aerodynamic damping that is when the surrounding flux starts to influence the motion. Large positive aerodynamic damping may be exhibited by structures such as large roofs, where large volumes of air are displaced by the structures' motion. Aerodynamic damping may become significantly negative for other structures at various wind speeds, leading to aerodynamic instabilities. A complete overview of these effects can be found in (Simiu and Scanlan 1996) with particular attention to bridges and high-rise buildings. The aerodynamic damping, as well as the structural damping, usually exhibits significant amplitude dependence, for that reason its importance increase when talking about extreme vents analyses.

5.2.1

Outline

The principal sources of fluctuating pressure and the corresponding forces are divided into three types. In the first the pressure variation follows the variation of the stream velocity according to the quasi-steady theory in natural turbulence stream flow. The second appears following the separation and reattachment of the vortexes (vortex shedding), then the body itself generates an unsteady flow and thus unsteady pressures. In the last type the movement of the structure itself modify the fluctuating pressure and forces; this is the case of the aerodynamic damping.

The concept of quasi-steady theory essentially implies that for every instant during the oscillations, the aerodynamic forces remain the same as the forces on a rigid segment of the body at the same angle of attack. This assumption has been shown to hold good for large reduced velocities where the wavelengths associated with the frequencies of aerodynamic loading are several times the representative width of the building. In this situation, the approaching flow can be assumed to be locally steady. The aerodynamic damping on a segment of a building is determined from sectional aerodynamic characteristics for the corresponding angle of attack in terms of pressure and force coefficient and the relative velocity.

The assumptions of this theory are the most common in the prescription of the national standards in wind loads. The variation of the fluctuation pressure is supposed equal to the variation of the longitudinal wind speed:

$$p(t) = C_{po}\frac{1}{2}\rho U(t)^2 \tag{5.5}$$

where C_{po} is the quasi-steady pressure coefficient and $U(t) = \overline{U} + u'(t)$ is the velocity of the flow composed by a mean and a fluctuation term. The mean pressure value should be calculated as:

$$\bar{p} = C_{po}\frac{1}{2}\rho(\overline{U}^2 + \sigma_u^2) \cong \bar{C}_p\frac{1}{2}\rho\overline{U}^2 \tag{5.6}$$

According to the quasi-steady assumptions the turbulent intensity is small and negligible if compared with mean wind speed, and also the pressure coefficient is approximated with the mean pressure coefficient $\bar{C}_p$.

Subtracting (5.6) from (5.5), the fluctuating time dependent pressure $p'(t)$ is obtained, from which a quasi-steady relationship between the mean square values of the pressure fluctuation and the wind velocity fluctuation (Holmes 2001):

$$\overline{p'}^2 = \bar{C}_p^2 \rho^2 \overline{U}^2 \overline{u'}^2 \tag{5.7}$$

and the corresponding peak pressure used in many codes and standards related to the peak gust wind speed:

$$\hat{p} = \bar{C}_p \frac{1}{2} \rho \widehat{U}^2 \tag{5.8}$$

The quasi-steady theory is generally not applicable in the low reduced velocity range where the evaluation of aerodynamic damping must be based on unsteady aerodynamics. This can be accomplished through a free oscillation or forced oscillation test.

More in general the equation of motion of an aerodynamically excited structure is given by the relation:

$$m\ddot{u} + c\dot{u} + ku = f(t, u, \dot{u}, \ddot{u}) \tag{5.9}$$

The left hand side of the equation represents typical inertial, damping and stiffness forces acting on the structure, whereas the right-hand side of the equation denotes the aerodynamic forcing function which is dependent on time, space and its derivatives. Typically $\ddot{u}$ and u are known to have insignificant influence on building response due to the relatively small value of the aerodynamic mass and stiffness in comparison with that of the building. On the contrary the $\dot{u}$ term, depending on its sign, contributes with positive or negative values increasing aerodynamic damping on structures (Kareem and Gurley 1996). Since the aerodynamic damping is due to building motion, it is manifested in the along-wind, across-wind and torsional directions.

If a structure oscillates, for example, in a flowing medium, forces arise which depend upon the motion of the system in the same way as damping forces do. If we also include the externally applied aerodynamic or hydrodynamic forces in this group of forces, we are led to the unusual concept of negative damping. In fact, a phenomenon can occur which appears strange at first sight: an oscillating structure may extract energy from the flow, in which case the oscillation is not damped, as in the presence of positive damping which consumes

energy, but incited, as would arise from a so-call negative damping model. Well-known examples of the above phenomena are the vibration (and collapse) of an open air transmission line, suspension bridge and cooling towers or the flutter of aeroplanes and car wheels. For the latter phenomena the name *aeroelasticity* has been coined.

5.2.2

Model of an aeroelastic correction

Aerodynamic forces

Dealing with wind as an element of a wider and more complex atmospheric and meteorological system, the analysis of wind actions and their effects on the structures is based on the evaluation of the wind speed U in the considered site.

In a fixed and non-deformable structure the wind load can be given by a set of aerodynamic forces $\boldsymbol{F_s}$. Assuming that the structure is subject to displacements caused by the wind action, resulting in small deflections, so that the state of the system can be identified with the initial configuration, the response $\boldsymbol{R}$ may be assessed with the classical methods of the structural analysis. This response is classified as static in case of very rigid and damped structures, while for flexible and narrowly damped structures the response has to be treated as dynamic.

Figure 5.2 shows the procedure to transform the wind speed $\boldsymbol{U}$ into the structural response $\boldsymbol{R}$.

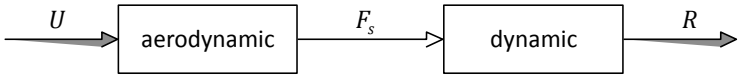

Figure 5.2: Aerodynamic structural response.

The aerodynamic forces depend on the shape, the dimensions and the orientation of the construction and on non-structural elements in relation to the wind direction. Moreover, the forces depend on the mean velocity and the turbulence of the wind, and they are closely related to the Reynolds number and the roughness of the surfaces, especially for constructions or elements with rounded surfaces (CNR-DT_207-08 2008). Under these assumptions, the wind load is simply due to the velocity pressure of a fluid in motion:

$$p = \frac{1}{2}\rho v^2 \tag{5.10}$$

where p is the velocity pressure, ρ is the density of the fluid ($1.25\ kg/m^3$ for the air) and v is the wind speed nearby the surface. In the present study, only the pressure normal to the surface is considered, i.e. generated by the component of the velocity orthogonal to the surface, thus friction phenomena are neglected.

Equation (5.10) is difficult to be applied in this direct form, since it requires the evaluation of all the velocities nearby each point of the surface. Therefore, all the flux lines and the local vortices derived from the presence of a body immersed in a fluid should be exactly known. Actually, a detailed evaluation of the fluid field is possible through CFD analyses, which nevertheless imply other uncertainties and troubles, like for instance the mesh dimension, the blockage of the flow, error estimators etc. (Coleman and Stern 1997), (Franke, et al. 2004).

In standard design approaches, (5.10) is usually transformed defining the pressure that acts on a surface as the product of a unique reference kinetic pressure $\boldsymbol{q_{ref}} = \rho \boldsymbol{U^2}/2$ and a field of the so-called pressure coefficients C_p variable throughout the points of the structure. All Standards define the reference kinetic pressure $\boldsymbol{q_{ref}} = \boldsymbol{q_{ref}}(z)$, in terms of reference wind speed $U(z)$ at the height z of the considered point, and specify the pressure coefficients only for the most common shapes, referring to detailed wind tunnel tests for the other cases. Therefore, (5.10) is usually expressed as:

$$p = q_{ref}(z) \cdot C_p \tag{5.11}$$

It is worth noting that the dimensionless value of the pressure coefficient depends on the value considered for the reference kinetic pressure. The Standards and the laboratories have to specify the measured height of the wind speed to reduce the pressure to a dimensionless value as well.

Aeroelastic forces

Dealing with very flexible and narrowly damped structures, characterized by an aerodynamic shape sensitive to wind actions, the structural displacements and velocities may be sometimes so large to produce wind-structure interaction phenomena, called aeroelastic or feedback effects. These effects modify the acting wind speed $\boldsymbol{v}$, the aerodynamic actions $\boldsymbol{F_s}$ and the response $\boldsymbol{R}$. These phenomena are normally modelled assuming that on the structure the wind produces global actions $\boldsymbol{F} = \boldsymbol{F_s} + \boldsymbol{F_a}$, where $\boldsymbol{F_s}$ are the aerodynamic actions supplied by the wind on the structure supposed as fixed, while $\boldsymbol{F_a}$ are the aeroelastic or auto-excited actions due to the structure's motion. In view of these concepts, Figure 5.3 illustrates the evolution of the scheme of Figure 5.2.

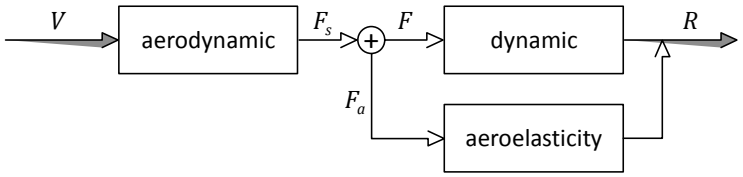

Figure 5.3: Aeroelastic structural response.

By definition, the aeroelastic forces cannot be directly determined, since they are related with the structure oscillations, which modify the acting flux and consequently the aerodynamic forces that the wind would produce on a fixed body. For simple structures and scarcely sensitive to this interaction, the codes usually suggest an equivalent static approach, in which the aerodynamic forces are amplified by a dynamic coefficient. For more particular cases the simplified methods are not exhaustive, therefore requiring detailed analyses which often make use of flexible scaled models analysed in the wind tunnel. Nevertheless, these extremely expensive tests imply considerable difficulties in post-processing the results: in particular, the experimental results cannot be directly used in the definition of numerical model loads, since the tests provide the complete structural response and not the values of the applied forces, with high uncertainties regarding the real safety coefficient of the structure.

Proposed corrective approach

From the above considerations concerning aerodynamic and aeroelastic forces it is possible to derive a simple and effective approach, to correct the aerodynamic data provided by the wind tunnel tests on rigid models, in order to numerically approximate the aeroelastic effects of wind-structure interaction. With this regard, two remarks are necessary to justify the suggested procedure:

Remark 1

The importance of taking into account the aeroelastic effects as an improvement of the aerodynamic forces depends on the entity of the structure's displacements for the dynamic load condition under consideration.

Remark 2

Equation (5.11) for the assessment of the pressure produced by an acting wind correlates the intensity of the action only to the kinetic loading $\boldsymbol{q_{ref}}$. It is assumed that the pressure coefficients C_p are not dependent on the variation of the acting wind speed.

Concerning these remarks, it should be emphasized that the present approach is not devoted to the substitution of the fluid-structure coupled analysis, but it is able to describe its effects with a minimal effort.

Starting from (5.10), it should be highlighted that the velocity wind pressure on a surface is unambiguously determined by the orthogonal component of the acting wind speed, neglecting the friction effects, as already mentioned. Also, (5.11) relates the same local pressure acting on the structure to the reference loading, that identifies the intensity of the meteorological event, and to the pressure coefficients, that summarize the effects of local turbulence. Thus, the combination of the two relationships allows calculating the wind speed on the structure point by point:

$$\boldsymbol{p} = \frac{1}{2}\rho \boldsymbol{v}^2 = \frac{1}{2}\rho \boldsymbol{U}^2 \cdot C_p \tag{5.12}$$

$$\boldsymbol{v} = \sqrt{C_p} \cdot \boldsymbol{U} \tag{5.13}$$

It is worth underlining that the pressure coefficients C_p obtained by an aerodynamic wind tunnel test performed on a rigid model can be considered equivalent to those obtained by a test carried out on a flexible model of the same structure loaded with a weak wind action. In such a hypothesis, (5.13) gives the local wind speed on the real structure. This expression is particularly useful if whole time histories of C_p values, related to the gradient wind speed, are available.

Summarizing, given the two aforementioned assumptions, it is possible to consider the pressure coefficients measured in a rigid model equivalent to the values measured on a flexible model with low wind speeds (remark 1, Figure 5.4a). Afterwards, the varying-in-time local velocity is calculated as a function of the wind outer the structure and of the quantities $C_p(\boldsymbol{x}, t)$ assumed independent from the wind intensity (remark 2, Figure 5.4b). Such a local velocity is applicable to a numerical model of the flexible structure (Figure 5.4c).

More in detail, let us consider a surface loaded by an orthogonal wind with velocity $\boldsymbol{v}$ moving through the air with velocity $\dot{\boldsymbol{u}}$. The *effective pressure* acting on the element, which includes the aeroelastic effects, is given by:

$$\boldsymbol{p_a} = 1/2\ \rho(\boldsymbol{v} - \dot{\boldsymbol{u}})^2 \tag{5.14}$$

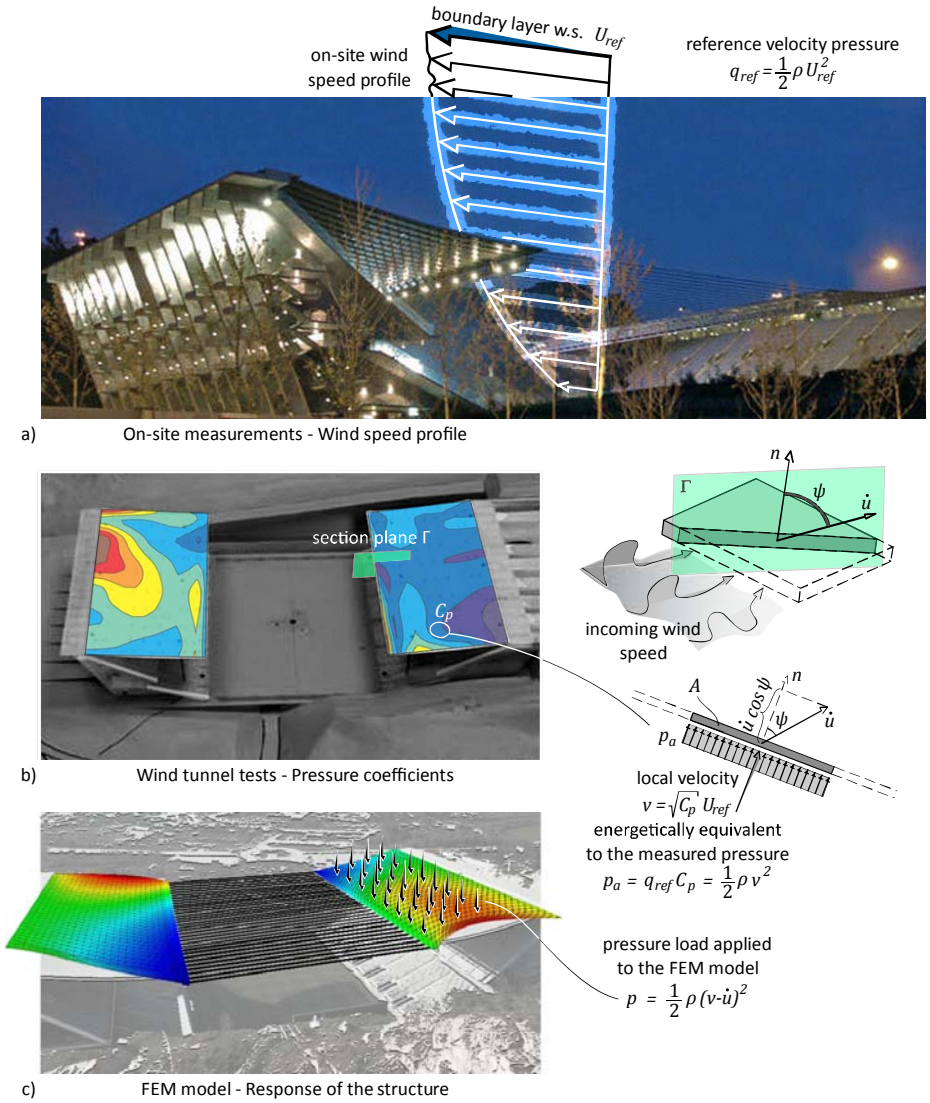

Figure 5.4: Steps of the aeroelastic correction.

In (5.14) the difference of velocities is written in vector form due to the generic lack of alignment of the two components. Moreover, it is worth underling the absence of corrective coefficients, since the two velocities are exactly those acting on the surface.

From (5.14), the two contributions of the fluid-structure interaction force may be identified:

$$\boldsymbol{p_a} = \underbrace{\frac{1}{2}\rho|\boldsymbol{v}|^2}_{aerodynamic} \underbrace{-\frac{1}{2}\rho 2(\boldsymbol{v}\cdot\dot{\boldsymbol{u}}) + \frac{1}{2}\rho|\dot{\boldsymbol{u}}|^2}_{aeroelastic} \tag{5.15}$$

From this operation, it is clear that the first term is the external pressure measured in the aerodynamic tests in the wind tunnel, while the other two terms constitute the *aeroelastic correction*.

The terms of (5.15) have to be additionally corrected, since in the transformation from pressure to force acting on the element, the terms must be multiplied by the area stricken by the flux. This is calculated as the projection of the total area on the plane orthogonal to the velocity direction.

The first term of (5.15) contains the definition of the velocity orthogonal to the element, thus the pressure has to be multiplied by the total area (Figure 5.4b). In the second term, the inner product between the velocities is $(\boldsymbol{v}\cdot\dot{\boldsymbol{u}}) = |v|\cdot|\dot{u}|\cos\psi$, i.e. the product between two components orthogonal to the surface, where ψ is the angle between the element velocity and its normal vector. The reference area is again the total area of the element. The third term is referred to the velocity $\dot{\boldsymbol{u}}$ of arbitrary direction. The force normal to the surface is a function of the normal component $|\dot{u}|\cos\psi$. With this further correction, the fluid-structure interaction force acting on an element of area A may be written as:

$$\boldsymbol{F} = p_a^{\perp}A = \left(\frac{1}{2}\rho|\boldsymbol{v}|^2 - \frac{1}{2}\rho 2(\boldsymbol{v}\cdot\dot{\boldsymbol{u}}) + \frac{1}{2}\rho|\dot{\boldsymbol{u}}|^2\cos^2\psi\right)A \tag{5.16}$$

5.2.3

Application to a single degree of freedom

In this section a schematic single degree of freedom system subjected to a harmonic load condition is investigated. In order to visualize the benefits of this formulation the solutions of the equation of motion without and with aerodynamic correction are compared.

Starting from the general equation of motion (5.9), a simple system reproducing a wind-type load analysis is considered. The system (Figure 5.5) is completed represented by the total mass m of the building, the main circular frequency $\omega = \sqrt{k/m}$ and the structural damping ratio ξ. With the purpose of applying a fluctuating wind-type load (5.11), a harmonic excitation is chosen, simplifying the general $f(t,u,\dot{u},\ddot{u})$, which depend on the dis-

placement and its derivatives, with a harmonic excitation $f = Q \sin \bar{\omega} t$ with frequency $\bar{\omega}$ and amplitude $Q = \rho A U_{ref}^2 \bar{C}_p / 2$ affecting a general area A:

$$f(t) = \frac{1}{2} \rho A U_{ref}^2 C_p(t) = \frac{1}{2} \rho A U_{ref}^2 \bar{C}_p \sin \bar{\omega} t \tag{5.17}$$

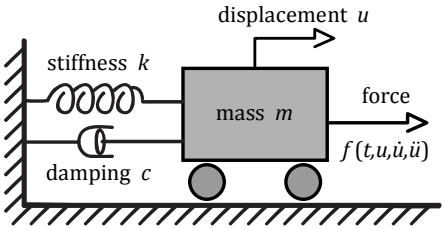

Figure 5.5: Idealized single degree of freedom.

In (5.17) it is assumed to preliminarily know the pressure coefficients time series. These assumptions are consistent with an ideal design process in which the structure is actually well represented by its first mode and a wind tunnel test on rigid model returns harmonic pressure coefficients. Under these hypotheses, the standard equation of motion including the structural viscous damping can be written as a linear second order ordinary differential equation with constant coefficients:

$$\ddot{u}(t) + 2\xi\omega\dot{u}(t) + \omega^2 u(t) = \omega^2 \frac{Q}{k} \sin \bar{\omega} t \tag{5.18}$$

The total response consists of a transient response which damps in accordance to $\exp(-\xi\omega t)$, and the steady-state response which will continue indefinitely (Argyris and Mlejnek 1991). From the engineering point of view the steady-state harmonic response is the more interesting part. The analytical solution is composed by:

$$u_{transient} = (a_1 \cos \omega_D t + a_2 \sin \omega_D t) e^{-\xi \omega t} \tag{5.19}$$

$$u_{steady} = u_{st} \frac{(b_1 \sin \bar{\omega} t - b_2 \cos \bar{\omega} t)}{b_1^2 + b_2^2} \tag{5.20}$$

where the coefficients are $b_1 = 1 - \beta^2$, $b_2 = 2\xi\beta$, while $\beta = \bar{\omega}/\omega$ is the ratio of the applied loading frequency $\bar{\omega}$ and the natural free-vibration frequency ω; ω_D is the free-vibration frequency of the damped system and $u_{st} = Q/k$ is the displacement which would be produced by the loading statically applied. The remaining coefficients in the transient response are given by the imposition of the initial conditions. For example, giving the initial displacement u_0 and velocity $\dot{u}_0$ we have:

$$a_1 = u_0 + u_{st}\frac{b_2}{b_1^2 + b_2^2} \tag{5.21}$$

$$a_2 = \frac{1}{\omega_D}\left(\dot{u}_0 + a_1\xi\omega - \bar{\omega}u_{st}\frac{b_1}{b_1^2 + b_2^2}\right) \tag{5.22}$$

The ratio of the resultant harmonic steady-state response amplitude ρ to the static displacement which would be produced by the force Q is called *dynamic magnification factor DMF* (Clough and Penzien 1993), thus:

$$DMF = \frac{\rho}{u_{st}} = [(1 - \beta^2)^2 + (2\xi\beta)^2]^{-1/2} \tag{5.23}$$

Equations (5.20) and (5.23) are referred to the standard equation of motion (5.18) without any modification due to the fluid-structure interaction. A modified expression of (5.18) can be obtained applying (5.14) on the right-hand-side:

$$m\ddot{u} + c\dot{u} + ku = \frac{1}{2}\rho A(v - \dot{u})^2 \cdot S_{v-\dot{u}} \tag{5.24}$$

using the local wind speed v from (5.13) and extracting the sign of the modified force: $S_{v-\dot{u}} = \text{sign}(v - \dot{u})$. In ordinary analyses the local wind speed is always greater than structure velocity ($v > \dot{u}$); in those cases it can be impose $S_{v-\dot{u}} = \text{sign}(v) \equiv \text{sign}(C_p)$, simplifying the calculation.

Equation (5.24) is written introducing the velocity dependent correction in the force term. An equivalent version of the equation can be obtained modifying the damping coefficient on the left-hand-side. Expanding the force in (5.24) and rearranging the terms, the other version of the equation of motion can be rewritten as:

$$m\ddot{u} + \left(c + \rho A v S_{v-\dot{u}} - \frac{1}{2}\rho A \dot{u} S_{v-\dot{u}}\right)\dot{u} + ku = \frac{1}{2}\rho A v^2 S_{v-\dot{u}} \qquad (5.25)$$

In the latter, the non-linear form of the aerodynamic correction is explicit. The new damping coefficient is no-more constant (containing $v = v(t)$), moreover it includes the unknown terms $\dot{u}$ and $S_{v-\dot{u}}$. A close-form solution of (5.24) or (5.25) is difficult to be achieved, and it will not be of practical interest because it will depend on the exact pressure coefficient function. Besides, (5.24) and (5.25) are quite simple to solve numerically using, for instance, the well-known Newmark algorithm (Newmark 1959).

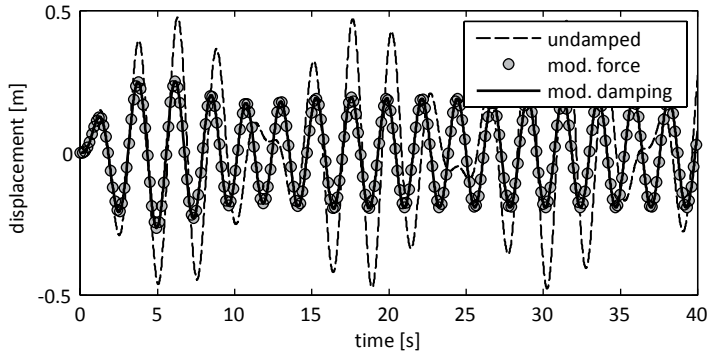

Figure 5.6: Response of a SDOF system. Comparison between the aeroelastic correction formulae.

Figure 5.6 shows an application of the developed method to a SDOF system with the following characteristics: $m = 3\,Kg,\ \omega = 2.24\,rad/s,\ \beta = 1.23,\ \xi_s = 0,\ Q = 1.65\,N$. The dashed line represents the analytical displacement evolution of the un-damped system ((5.19)+(5.20)); the marked and continuous lines represent the displacement of the system including the aerodynamic correction in the two presented forms (5.24) and (5.25) respectively. It appears evident that there are no differences when the modification affects the force or the damping term. By the way, is must be noted that in general multi-degree-of-freedoms system the two equations involve different non-linear solver schemes.

For the sake of simplicity, according to many real application of this approach, if we assume that during all the simulation the peak structural velocity $\dot{u}_{max}$ will remain much smaller than the local wind speed v_{max}, further approximation can be done in (5.25). First of all, $S_{v-\dot{u}}$ can be replaced by $\mathrm{sign}(v)$, than the quadratic term in the damping coefficient may be neglected without losing accuracy. Afterwards, the approximated linear equation

of motion including the structural and aerodynamic damping coefficients can be written following the relation in (5.26).

$$\ddot{u}(t) + 2(\xi_s + \xi_a)\omega\dot{u}(t) + \omega^2 u(t) = \omega^2 \frac{Q}{k} \sin \bar{\omega} t \tag{5.26}$$

where the forces are given by the wind tunnel tests and the aerodynamic damping coefficient is expressed in terms of damping ratio with respect to the critical damping. The aerodynamic damping ratio (5.27) is function of the local velocity, i.e. it is a time-dependent variable:

$$\xi_a(t) = \frac{\rho A v(t)}{2m\omega} \tag{5.27}$$

In the special case of periodic load signal similar to (5.17), ξ_a could be approximated with the mean value in time as expressed in (5.28).

$$\bar{\xi}_a = \frac{\rho A}{2m\omega} \frac{1}{T} \int v(t) = \frac{\alpha Q}{m\omega v_{max}} \tag{5.28}$$

In case of a harmonic excitation, like in (5.17), $\alpha = 0.763$.

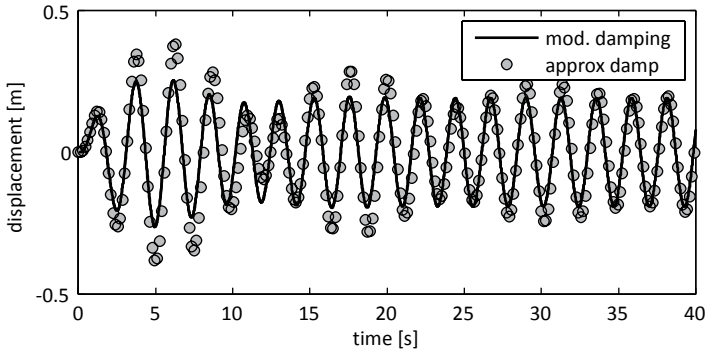

Figure 5.7: Response of a SDOF system. Damping coefficient's approximation.

As a simple view of the magnitude of the latter coefficient, Figure 5.7 shows the different displacement response from the previous example. The continuous line reports the non-linear solution found applying (5.25), the same as in Figure 5.6, while the marked line is

made by (5.26) using the mean aerodynamic damping coefficient ratio $\bar{\xi}_a = 9\%$ from (5.28).

From this comparison appears that the transient responses remain different, while the steady-state part, which appears during the last part of the simulation, is well fitted by the linear solution using the mean aerodynamic damping correction.

Energy estimation

In a dynamic process, the total energy is measured as the sum of the kinetic energy E_{kin} plus the strain energy (or internal force energy) E_{str}:

$$E_{kin}(t) = \frac{1}{2} m\, \dot{u}(t)^2 \tag{5.29}$$

$$E_{str}(t) = \int_{\Omega} \sigma(t)\, \varepsilon(t)\, d\Omega \tag{5.30}$$

while the external work W fed into the system during a certain time is:

$$W(t) = \int_0^t f(\tau)\, du(\tau) \tag{5.31}$$

In the previous expressions σ and ε are the stress and strain defined inside the domain Ω and τ is the time parameter which goes for 0 to t.

In an undamped system lacking in external forces, the total energy remain constantly equal to the energy given from the initial conditions u_0, $\dot{u}_0$. For instance, the initial energy in the single degree of freedom system described in Figure 5.5 is simply:

$$E_0 = \frac{1}{2} m\dot{u}_0^2 + \frac{1}{2} k u_0^2 \tag{5.32}$$

Adding a non-conservative time-dependent external force $f(t)$ the total energy varies according to (5.31). It is strongly pointed out that the external work W depends not only by the external force $f(t)$, but also from the point motion $u(t)$, $\dot{u}(t)$ during the load process.

$$E(t) = \frac{1}{2} m\, \dot{u}(t)^2 + \frac{1}{2} k\, u(t)^2 = E_0 + \int_0^t f(\tau)\, du(\tau) \tag{5.33}$$

Figure 5.8 shows the total energy trend referred to the previous example where the initial energy is set to 0. The dashed line illustrates the external work fed into the system while the continuous and marked lines show the total energy related to the solutions of (5.25) and (5.26) respectively. It can be seen that the equivalent aeroelastic damping coefficient (5.28) well approximates the complete non-linear solution in the steady-state phase, although it underestimates the energy loss in the initial transient phase.

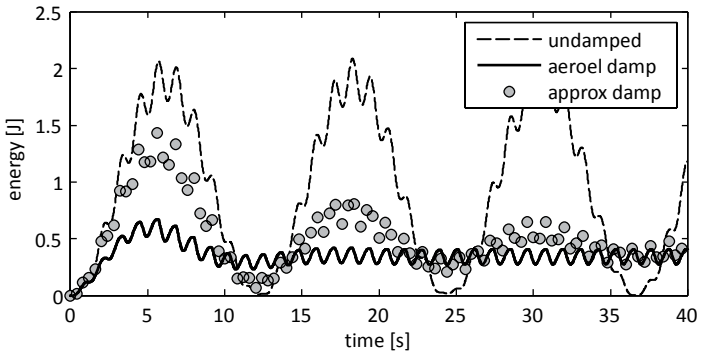

Figure 5.8: Response of a SDOF system: Total energy.

5.2.4

Vortex shedding in a chimney

In this section, the classical experiment of vortex shedding in a chimney subjected to the harmonic lift load due to the cyclic separation of the Von Karman vortices is presented (Figure 5.9a). The test aims to assess the order of magnitude of the additional aerodynamic damping ξ_a usually neglected in standard civil engineering design processes, and to validate the simplified proposed approach in approximating the coefficient through the comparison with a 2D CFD simulation of a physical problem.

The test is set up in two steps. Initially the chimney is kept fixed into an incoming flow and the lift force coefficient is measured. Subsequently, the across-wind translational degree of freedom u is released, Figure 5.9a, maintaining the other boundary conditions unchanged. In this case a complete fluid-structure interaction is considered; thus a direct total response monitoring is available.

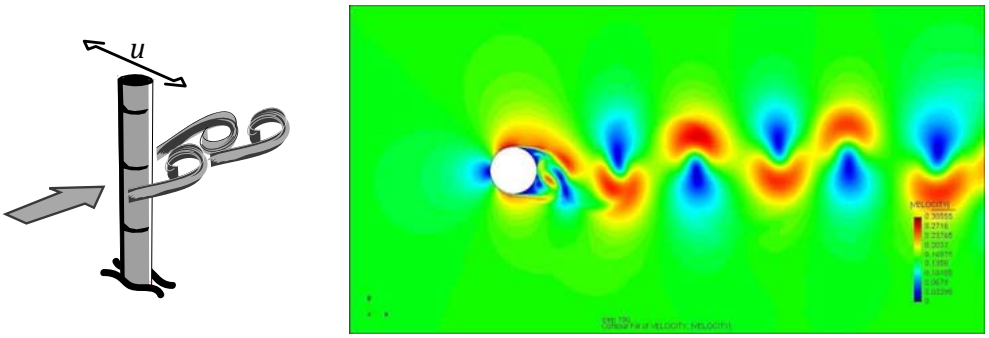

a) b)

Figure 5.9: Vortex shedding in the cylinder wake: a) test sketch; b) CFD visualization of the Von Karman vortexes.

The test aims to assess the order of magnitude of the additional aerodynamic damping ξ_a usually neglected in normal civil engineering design processes, and to validate the simple proposal approach in approximating that coefficient.

The experiment is carried out numerically with the support of the open source code Kratos developed at CIMNE Barcelona. In references (Dadvand 2007), (Larese, et al. 2008) the theoretical aspects of the code and a complete series of benchmarks for the validation of the code for CFD and multi-physics analyses are reported.

It is assumed that the structure is a cylinder with diameter D, $1\ m$ height, and a rigid surface; the incoming flow has uniform mean velocity U; the elastic deflection of the body are the same throughout its length, the body possesses no structural damping in the across-wind direction and is rigidly constrained in the along-wind direction. Under the action of the vortices shed in its wake the cylinder will be driven periodically. Near the vortex frequency, related to the Strouhal number, large displacement occur and the body begins to interact strongly with the flow.

During the first part of the analysis, when the body is fixed, the across-wind force per unit length is measured (see Figure 5.9b). According to standard nomenclature, this is called *lift force* per unit depth and is expressed as:

$$F_L = \frac{1}{2}\rho U^2 D L C_L \sin \bar{\omega} t \tag{5.34}$$

Figure 5.10 shows the resulted lift force that reach the suitable harmonic form after the first stabilizing period, almost $20\ s$. Results of this preliminary test are taken as input parameter for further simulations. In this context, the fix-body CFD test is considered as substituting an eventual wind tunnel test on rigid body. Further free oscillation test will be

explained comparing the results from free-body CFD simulations and the aeroelastic correction approximation (5.25) giving (5.34) as input load. Input data for the simulations are reported in Table 5.2.

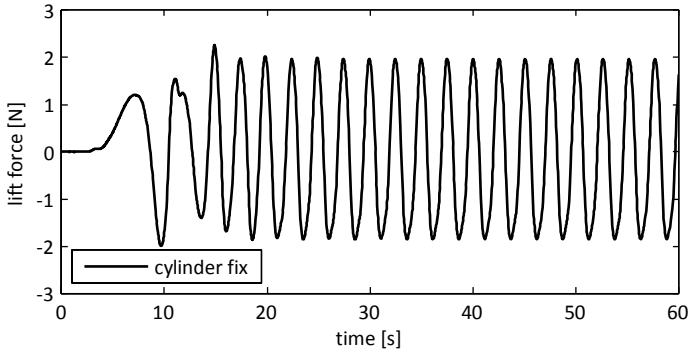

Figure 5.10: Vortex shedding CFD test. Lift force in the fixed body.

Regarding the chimney top section, Figure 5.11 shows the displacement time histories using the present simplified approach, depicted with the continuous line, compared with the CFD results represented by the marked dotted line. Moreover the two horizontal lines, corresponding to a displacement of about $\pm 0.1\ m$, are the maximum amplitude of the response obtained by performing an analysis without taking into account the aeroelastic correction. In such a hypothesis the solution is significantly different from the results of the CFD analysis.

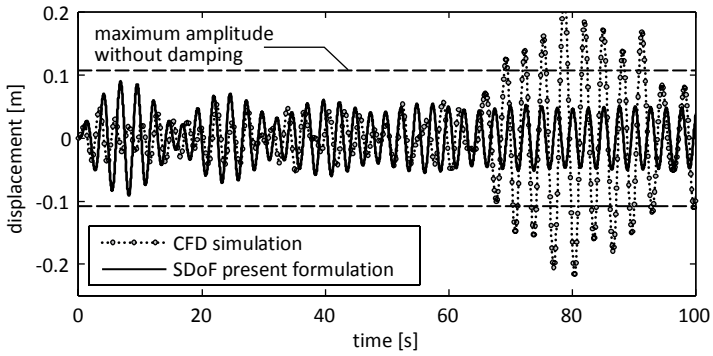

Figure 5.11: SDOF - CFD comparison. Vertical displacement of the cylinder.

On the contrary, it is worth noting a proper fitting of the steady-state response obtained by using the proposed method applying (5.25) with the CFD numerical simulation until about $60\ s$ when the cylinder's motion starts to synchronize with the vortexes. At this

time, the motion adjusts physically the vortexes separation point changing the lift forces. When such aeroelastic instability starts, the required assumption of steady pressure coefficients is not valid anymore (Figure 5.12) and the simplified approach is no more a suitable method.

Table 5.2: Vortex shedding test data.

domain size	40 × 30 *m*			
number of elements	42500			
element type	fluid ASGS			
fluid solver	monolithic solver ALE			
time step	Δt	=	0.025	*s*
duration of the first part of simulation (fixed body)	T_{fix}	=	60.00	*s*
duration of the second part of simulation (free body)	T_{free}	=	200.00	*s*
cross section diameter	*D*	=	1.00	*m*
reference length	*L*	=	1.00	*m*
mass	*m*	=	20.00	*kg*
stiffness	*k*	=	88.28	*N/m*
structural circular frequency	ω	=	2.10	*rad/s*
structural damping ratio	ξ_{st}	=	0.00 %	
wind speed	*U*	=	1.50	*m/s*
air density	ρ	=	1.25	kg/m^3
lift force coefficient	C_L	=	1.35	
vortex circular frequency	$\bar{\omega}$	=	2.49	*rad/s*

A complete treatment of the vortex shedding can be found e.g. in (Vickery and Basu 1983), (Dyrbye and Hansen 1996) or (Simiu and Scanlan 1996).

It is worthy underline that interest of the author in the present work of thesis is to demonstrate the ability of the proposed approach to properly represent the behaviour of such a system before the vortex shedding trigger, which is a phenomenon requiring specific approaches to be treated.

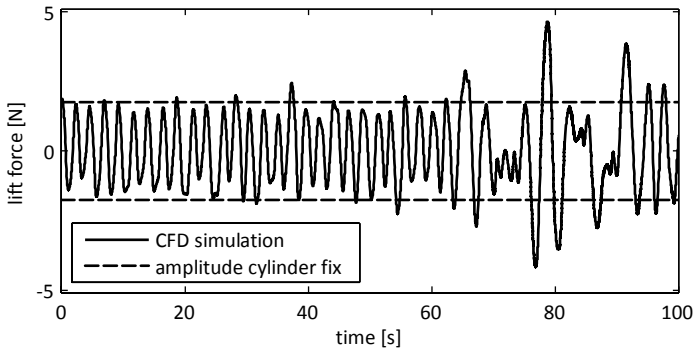

Figure 5.12: SDOF - CFD comparison. Lift forces.

5.2.5

Application to the roof of the stadium of Braga

In the following, four analyses of the present case study are presented. The tests differ in the combination of structural and aeroelastic damping taken into consideration. The structural damping ratio is fixed to 0.5%. This value was experimentally obtained through a harmonic load test carried out on the built-up stadium (Cosentino and Majowiecki 2004). Analyses 2 and 4, which include aeroelastic damping, have been solved by using (5.25). The experimentally measured pressure coefficients are referred to the kinetic pressure calculated with the gradient wind speed. The presented numerical simulations take into consideration the wind blowing from a direction of $220°$ starting from the true North, with gradient wind speed of $30\ m/s$. All the tests information is reported in Table 5.3.

Table 5.3: Braga stadium data.

roof size (2 slab ×)		57.0 × 126.0		*m*
central gap (without slabs)			88.0	*m*
roof height	H_r	=	45.0	*m*
gradient height (estimated)	δ	=	400-600	*m*
roof mass	M	=	10.5×10^3	*t*
principal frequency	ω_1	=	1.70	*rad/s*
structural damping ratio	ξ_{st}	=	0.50 %	
reference wind speed	U	=	30.00	*m/s*
reference wind direction	θ	=	220.00°	*rad/s*

Table 5.4 sums up the damping contributions and the energy distributions between the modes. The modal decomposition has been made using the Proper Orthogonal Decomposition (POD) of the response displacement fluctuations (see section 3.1). It should be noted that the slope of the roof for the rainwater drainage implies the not perfect symmetry of the roof in relation to the middle axis parallel to the cables. This particular geometry justifies the existence of couples of modes with close frequencies and almost symmetrical configurations (see section 4.6). For instance the values of the first two natural frequencies are 0.263 and $0.277\ Hz$ respectively. As reported in Table 5.4, the first two modes incorporates about the 85% of the total fluctuation energy. The following response time histories are referred to the vertical displacement of the roof resulting from the analysis of the first and second proper mode.

Table 5.4: Damping set-up and mode's energy.

simulation	ξ_{st}	ξ_a	λ_1	λ_2	λ_3
1	no	no	59%	26%	6%
2	no	yes	54%	33%	6%
3	0.5 %	no	53%	31%	6%
4	0.5 %	yes	50%	35%	7%

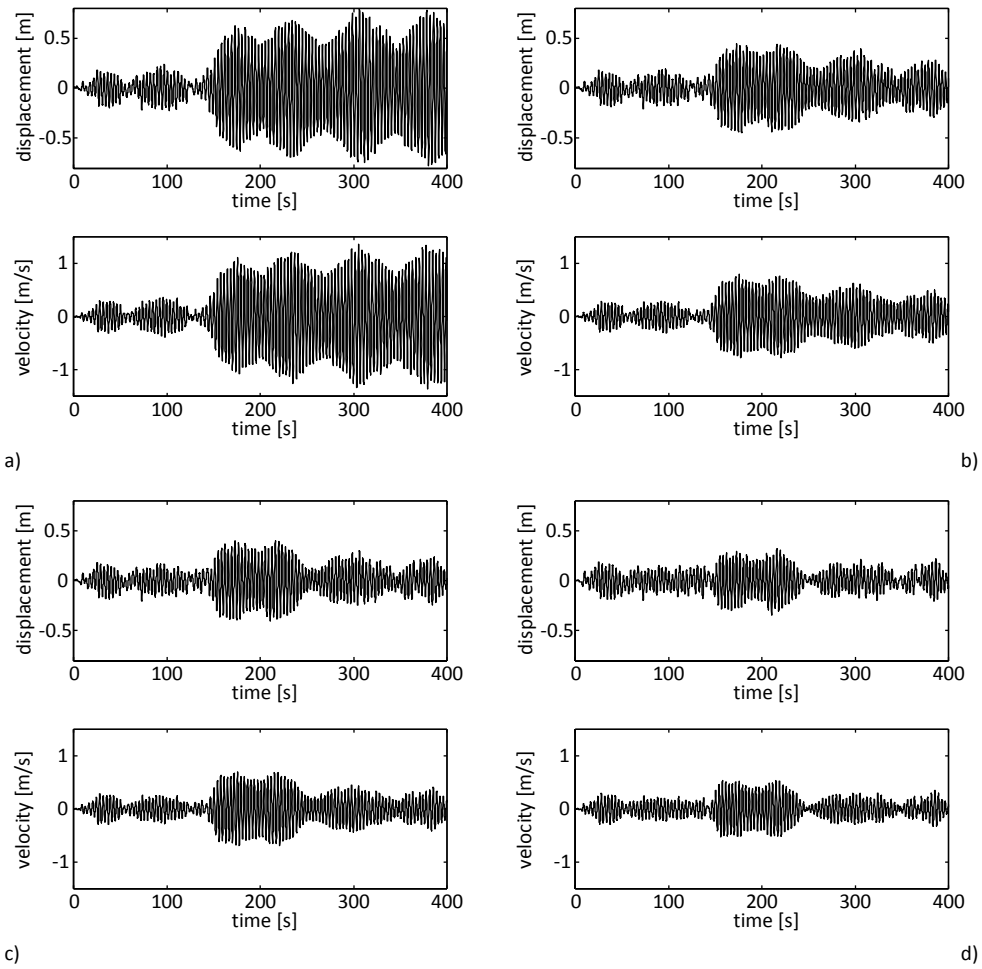

Figure 5.13: Response time history: a) simul.1 (without any damping); b) simul.2 (with aeroelastic damping only); c) simul.3 (with structural damping only); d) simul.4 (with both damping mechanisms).

Figure 5.13a reproduces the vertical displacement and velocity of the roof without any damping coefficient. The increase of magnitude due to resonance effects is clearly shown. In this test the fact that the displacement and velocity does not increase indefinitely, but tends to an asymptote, is the consequence of the geometrical non-linear behaviour of the structure.

By considering damping coefficients, the maximum displacement is reduced until almost 50% with respect to the undamped system. Figure 5.13b includes only the effects of the aeroelastic damping and the resulting values are comparable with those depicted in Figure 5.13c that refers to the case of a constant structural damping $\xi_{st} = 0.5\%$. This means that

the effect of taking into account the aeroelastic damping for this structure with this wind speed can be considered equivalent to the effect of the structural damping.

The last graph, Figure 5.13d, includes both the mechanisms, i.e. structural and aeroelastic damping, but obviously the total amount of dissipation is less than the sum of the considered damping mechanisms taken separately.

Finally, Figure 5.14 shows the comparison in energetic terms between the different simulations. In particular Figure 5.14a highlights the time gap, almost $150\ s$, needed to the structure for synchronizing its motion with the wind load. Simulation 1 in the same graph illustrates the total amount of energy added in the system by the wind excitation. Simulations 2, 3, 4 quantify the dissipation's levels given by different damping hypotheses. In Figure 5.14b, the same dissipation's levels are evidenced in terms of ratios with respect the total energy (simulation 1).

The energy comparison evidences the remarkable increment of dissipation due to aeroelastic component of damping. For the adopted reference wind speed ($30\ m/s$), an increment of roughly 0.3% of damping ratio is available. Further analyses, carried out by applying the ultimate design wind speed $U_{ref}^{ULS} = 55\ m/s$, have provided values of aeroelastic damping ratio of the same magnitude with respect to the structural damping. In those cases the damping coefficients should be considered twice the measured structural value.

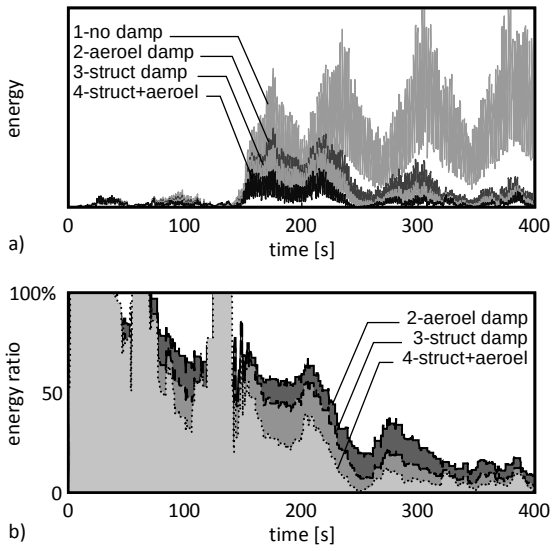

Figure 5.14: Comparison in energetic terms between the different simulations: a) total energy; b) energy ratio with respect to the first simulation.

5.3 FULL SCALE IDENTIFICATION

The intricate nature of different damping mechanisms produces uncertainties even in the interpretation of data obtained from full-scale test in structures. Problems of such investigation are related to the identification and separation of the mechanisms further than their characterizations with the minimum amount of parameters (Li, et al. 2000).

There are two main techniques for determining damping in full-scale structures: free vibration, also referred as ambient excitation, and forced excitation. In the free vibration case, ambient conditions are used to allow the structure to oscillate, usually as result of wind excitation, thus the change of frequency and damping of models oscillating in wind can be observed. This method is mainly used to identify motion-dependent aerodynamic forces in case of bridge aeroelasticity. The force excitation requires active excitation through some form of mechanical device inducing a resonant response. An exhaustive discussion about the theoretical aspects can be found in (Clough and Penzien 1993) while (Littler 1995) reports several results and discussion in an application to tall buildings.

Having been performed a full scale-test with the suitable excitation, and the response of the structure in terms of the motion parameters is available, significant difficulties in predicting damping from that data still remains. The two most common techniques used to find the damping ratio are the autocorrelation decay and the random decrement analysis (Letchford, et al. 2002). The main problem with the autocorrelation decay is the requirement of self-stationary signals which is very difficult to achieve with ambient tests. The random decrement method, instead, overcome the requirement of self-stationarity samples by the superposition of a large number of short samples. On the other side, the force excitation technique surmounts these problems and also has the advantage of allowing the determination of the amplitude dependence in the damping ratio. These feature makes the force excitation the best available technique even if is surely more expensive.

5.3.1 Random decrement method

The *random decrement method* (RDM) was originally developed to extract free-decay response data from the *in-situ* response of a dynamic system subjected to ambient excitations. RDM was empirically developed at first by Cole (1968) (1973) analyzing experimental data for applications in the aerospace industry. The technique aims to determine the damping of a dynamic system extracting the signature from the ensemble averaging of segments of the response of the system (Ku, Cermak and Chou 2007). The requirement of

specific initial condition for each segment in the averaging procedure raises a signature which is filtered from all the signal components except the free vibration of the system from an initial displacement. Damping estimates should then be extracted from this free vibration decay (signature). The originality of the RDM is that the system identification can be obtained knowing only its response. This marks a main improvement between this method and other time-domain methods.

A *randomdec signature* is simply the trace formed by a waveform averaging a number of specially selected segments from an observed time history. Thinking about the dynamic response of a structure as the time-domain signal, at time $t + t_0$, it should consist of three components:

1- the step response from the initial displacements at time t_0;
2- the impulse response function (IRF) yielded from the initial velocity at time t_0;
3- the random response from the excitation applied to the structure in the period between t_0 and $t + t_0$.

These three parts of the response can be denoted in the following equation:

$$x(t + t_0) = x(t + t_0)|_{x(t_0)} + x(t + t_0)|_{\dot{x}(t_0)} + x(t + t_0)|_{f(t)} \qquad (5.35)$$

In the basic idea of the RDM, the previous response is considered as the sum of a deterministic component, which corresponds to the free vibration terms (points 1-2), and a random component, which correspond to the forced vibration (point 3). The objective is to remove the random component in order to obtain the typical free vibration decay curve, from which the damping ratio ξ can be estimated.

With respect to the great variety of possibilities for the resultant signature, the most popular, and the easier, choice is to specify only the initial amplitude for the segments. The RDM is demonstrated in principle in Figure 5.15, where the components of the signal are ensemble averaged separately to illustrate the progression of the signal from a forced vibration to free vibration decay.

If we pick a constant time segment from the response history every time the response amplitude reaches a selected value X_0, we obtain a number of response history segments of equal lengths τ that begin with the trigger amplitude X_0. Figure 5.15 shows some of the segments taken from a response history. The first segment begins at time t_1 and ends at $t_1 + \tau$. The whole segment can be denoted as $X_0(t_1 + \tau)$. The average of N segments is denoted as $\delta_N(\tau)$ and it is given in (5.36).

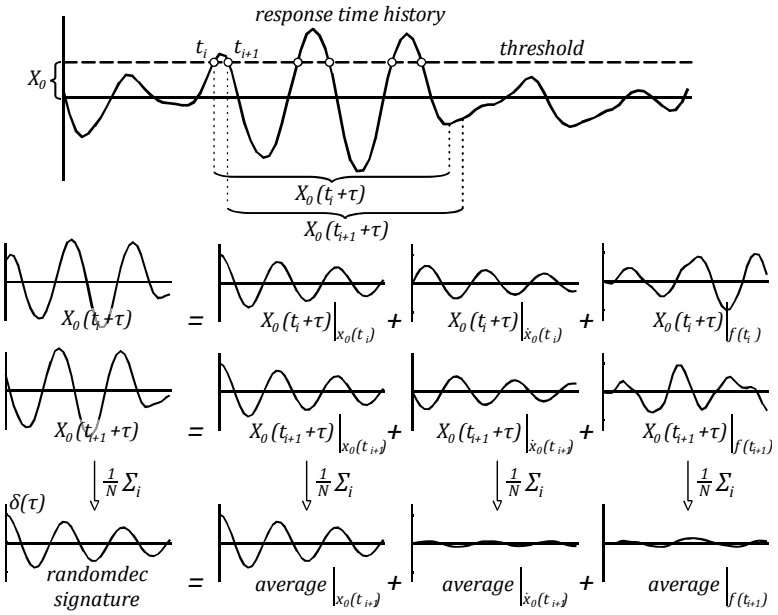

Figure 5.15: Operative scheme of the random decrement method.

$$\delta_N(\tau) = \frac{1}{N}\sum_{i=1}^{N} X_0(t_i + \tau) \tag{5.36}$$

As the number N increases, the part of the responses in each segment that corresponds to the initial velocity (impulse response) will be averaged out since the sign of the initial velocity appears alternatively. The random parts of each segment are also averaged out because of the random nature of the response, as shown in Figure 5.15. This means to assume that the average of the random response is zero (5.38). An assumption often considered acceptable.

$$\sum_{i=1}^{N} X_0(t_i + \tau)\Big|_{\dot{x}(t_0)} \to 0 \tag{5.37}$$

$$\sum_{i=1}^{N} X_0(t_i + \tau)\Big|_{f(t)} \to 0 \tag{5.38}$$

What is left after the average is the response due to the initial displacement step input. This output can be denoted $\delta(\tau)$, known as the *randomdec signature* (He and Fu 2001). It is expected that the random terms will have zero mean when a large number of segments are averaged. These considerations may not be valid for non-linear systems. However, if the system experiences some non-linear behaviour, the signature may still be close to the free vibration decay curve of a linear system.

The above description fits well a single-degree-of-freedom (SDOF) systems or systems in which one mode dominates the response. Even though the idea of the hypothesis is valid, the criteria for selecting the level of the amplitude threshold and window duration of the segments are not well supported and rest on the responsibility of the designer or the data analyst (Huerta, Roesset and Stokoe 1998).

This intuitive explanation is present in the great part of the available literature, and seems to be reasonable for linear systems. The technique has the advantage over the use of autocorrelation or spectral methods in that it is not encumbered by the limitation concerning input amplitude and resolution, respectively. Theoretically the technique should be valid only for a linear single degree of freedom system, permitting the superposition of different segments and with a stationary Gaussian white noise excitation to validate (5.38). However, Jeary (1992) and other researchers have found the method appropriate for nonlinear systems, and He et al. (2001) have extended the application to multi degrees of freedom systems. Nevertheless, the presence of non-linearities, as well as the non stationary external force, requires considerable number of segments, thus a large data set in order to produce suitable results.

Concluding, the damping estimation obtained from the *randomdec signature* as an approximation of the free vibration decay of the system does provide reasonable results in many applications. However, the requirement of a uniform value for the initial condition of each segment prejudices the expected value of the excitation, and the term in (5.38) is not necessarily zero in the average. Mathematically, Vandiver et al. (1982) have demonstrated that the assumption is actually correct only for the case where the excitation is stationary Gaussian white noise. For most applications, random decrement is applied to narrow-banded systems with relatively wide-banded excitation. Fur such cases a white noise approximation is acceptable, and the intuitive explanation is appropriate, through not rigorously correct.

The application of the Random Decrement Method on the simulation of the behaviour of the stadium of Braga roof is shown in Figure 5.16 and Figure 5.17, where the structural damping is considered alone or increased by the aerodynamic part (see section 5.2) respectively.

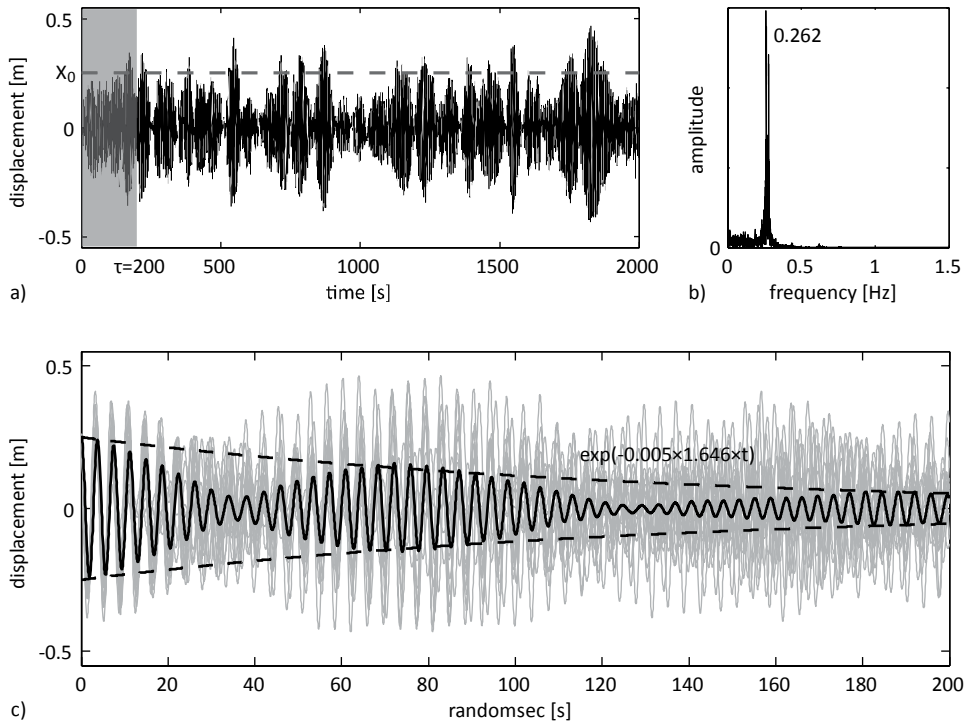

Figure 5.16: RDM analysis on the stadium roof. Simulation with only structural damping: a) vertical deflection time history; b) displacement spectrum; c) average of the randomdec signatures.

The first simulation (Figure 5.16) describe the behaviour of the roof under the effect of a windstorm coming from Southwest ($\theta = 270°$), with the gradient wind speed equal to $30\ m/s$ for more than half an hour continuously. The simulation include only the structural part of the damping mechanism inserted in the model following the relation of Rayleigh damping reported in (5.4), imposing $\xi_{st} = 0.5\%$ on the first and sixth natural frequency. Figure 5.16a reports the evolution of the vertical deflection of the roof corresponding to the first proper mode (see section 3.1) in the time domain, while Figure 5.16b highlights the related first natural frequency. In order to perform the RDM and extract the randomdec signatures, the initial shifted position X_0 and the signal length τ have to be fix. In this case the chosen initial position is $X_0 = 0.25\ m$ and the length is $\tau = 200\ s$ depicted in Figure 5.16a with the dashed line and the grey band respectively. The randomdec signatures $\delta(\tau)$ to be averaged are pieces of the full displacement time history covered by the grey band every time the signal rich the level X_0. Finally, Figure 5.16c shows the superposition of all $\delta(\tau)$, in light grey, and the resulting average plotted with the bold black line. The envelope of the averaged signal indicates the free vibration decay of the structure with usual exponential function which starts from X_0 and damps with the 0.5%.

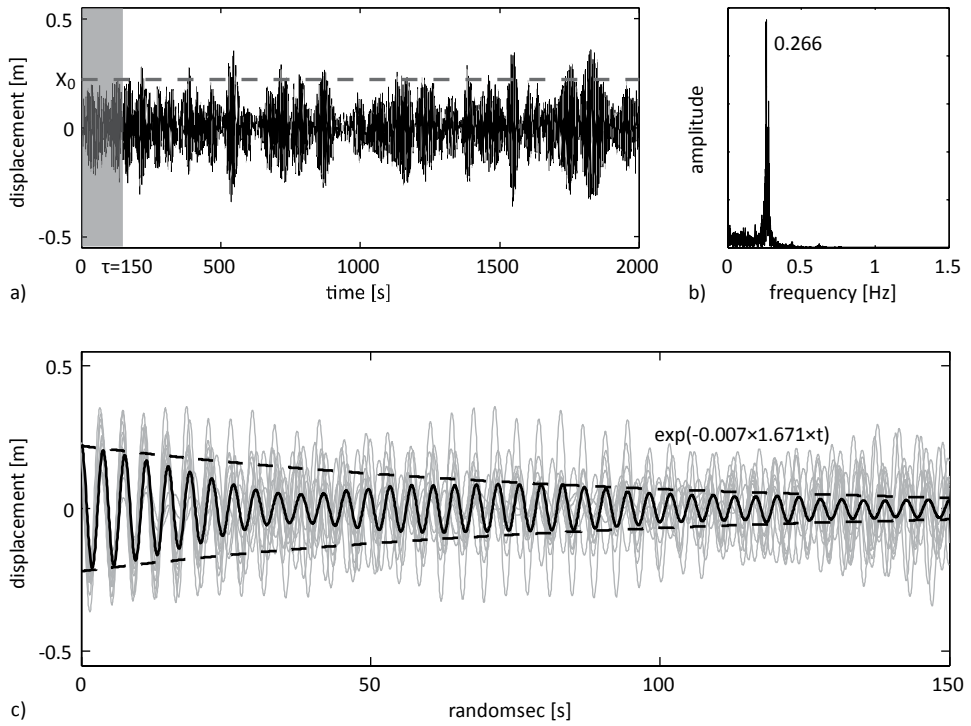

Figure 5.17: RDM analysis on the stadium roof. Simulation with structural and aerodynamic damping: a) vertical deflection time history; b) displacement spectrum; c) average of the randomdec signatures.

The latter simulation (Figure 5.17) runs through the same steps of the previous, just including also the aeroelastic correction on the damping coefficient as described in section 5.2.2. According to the qualitative results shown in Figure 5.13 and Figure 5.14 which reproduce the same test but with shorter period, and referring to the simulations *3-struct damp* and *4-struct+aeroel*, it is expected that the introduction of the aerodynamic damping will increase the damping ratio of almost the 50%. The extrapolation of the free vibration decay by using the RDM highlights a quantitative value of the total damping ratio of 0.7% (Figure 5.17c), which is in line with the expected value.

Concluding, all the tests and simulations presented in this section demonstrate that, when large volumes of air are displaced by the motion of a flexible roof, the increment of damping coefficient including the aeroelastic component is suitable and it can be correctly reproduced by the proposed method.

CHAPTER 6

WIND-INDUCED DAMAGE

Windstorms or gales in general have always been source of severe problems for human beings causing damages to buildings and other structures or infrastructures. In the past century, the preferred solution, and actually the only effective mitigation system, was to build heavy masonry constructions for the major community building, for instance churches and public warehouses, which could offer refuge to the inhabitants during catastrophic events (Holmes 2001). Increasing the self weight is a good way out to resist the wind forces, even though it can generate more problems for the static and also to potential seismic action.

It should be noted that during the last centuries the interest in wind engineering and afterwards the major discoveries and innovations, has always come immediately after an impressive structural failure. A spectacular example is the aeroelastic instabilities such as the *stall flutter* introduced as a topic in civil engineering after the impressive collapse of the Tacoma Narrow bridge (Figure 6.1a) in the Washington State in 1940 (Billah and Scanlan 1991). Other renowned bridge failures are the Tay Bridge in Scotland (1879), and the Brighton Chain Pier in England (1836).

Moving to large structures besides the long-span bridges, on November 1st 1965 a strong wind blew against the cooling towers at the Ferrybridge power station (Figure 6.1b), creating a windward and a leeward of four tower each. As the wind pushed past the towers in the windward row, it was funnelled through the spacing between them onto the second row of towers. The generated pressure created a vibration force that tended to lift the towers off their foundation causing the collapse of three cooling towers (Schlager 1994).

These events together with other major windstorms, which have originated damages in large scale affecting whole countries, are important for their role in promoting investigation and understanding in wind loads on structures. Moreover the increasing interest of many insurance company involved in natural hazards confirms the importance in the crea-

tion of suitable design approach for wind-resistant structures given their crucial potential financial losses in case of their failure.

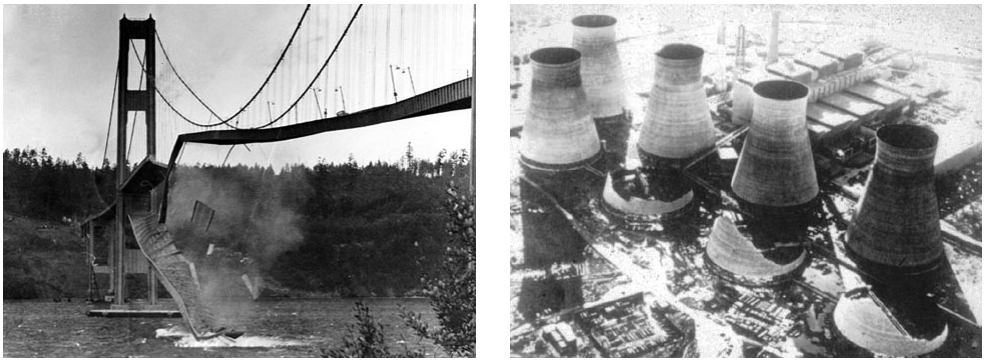

(a) (b)

Figure 6.1: Major structural failures: a) Tacoma Narrow bridge (1940); b) Ferrybridge cooling towers (1965).

Damage estimation is extremely sensitive to the considered of building or the storage contents (Elements of Risk) in relation of the Hazard Intensity (see chapter 1 for definitions), which is the wind speed for the present case study. The description of such relation can be done in several ways, for instance using the *vulnerability curves* like in (Leicester 1981) or (Khandury and Morrow 2003), but in every case it is crucial the definition of a comparison value expressed as *damage index* (*D*). Relations (6.1) and (6.2) give common definitions of the damage index in case it is referred to a building or to the stored contents respectively.

$$D(\text{buildings}) = \frac{\text{repair cost}}{\text{initial value}} \tag{6.1}$$

$$D(\text{goods}) = \frac{\text{insured value}}{\text{replacement cost}} \tag{6.2}$$

For fully-engineered structures, the relation (6.1) should be split firstly counting the number of damaged structural members or components for a given event, and then moving into an economical context estimating the losing in monetary terms. The distinction can be visualized looking at the last two rings of the risk assessment chain proposed in section 1.3 (Figure 1.5).

Looking only at the engineering part, usually the failure of each component is assumed to be independent with respect the others, taking into account that all of them are designed to resist the same wind load. The fractional damage to the entire building is proportional to the failed components. Considering all the components with the same probability dis-

tribution of strength, which is correct if the whole project is designed following the same code's prescriptions, then the vulnerability curve can be simply derived from the cumulative distribution of strength of any element (Holmes 2001).

6.1 STRUCTURAL DAMAGE

The roof of the Stadium of Braga is structurally constituted by a set of load-bearing cables and two concrete slabs. Assessing the effects of wind gales, in this section the thresholds for engineering parameters are defined considering the effects that the overcoming these values will produce in terms of global damage.

The stress distribution of the bearing cables that holds the two covers is statically determine, thus a failure of pairs of cables could not be supported with any kind of redistribution and parts of the roof would collapse. For that reason the cables failure behaviour is considered extremely brittle with few intermediate damage-brackets before the collapse.

On the other side, the slabs are designed as a continuum solidus on many flexible supports that means that exceeding the ultimate bending resistance on some section leads to possible redistributions of loads subjected to the slab stiffness. However the two concrete slabs are slightly reinforced then the bending resistance reserve is quite low. The damage index for this parameter is set not allowing the exceedance of the ultimate design resistance of the slabs and focusing on the roof cracking, as a warning of something not working properly.

6.1.1 Damage on the cables

According to the Italian company (Tensoteci) which has provided the full-locked steel cables, the guaranteed break load is not lower than $7720\ kN$ for each cable (see Table 2.1). However multiplying directly the effective cable's area by the proofed stress and dividing the results by the partial factor for resistance of the cross section $\gamma_M = 1.15$, following the Eurocode prescription, a rather lower design value of the resistance to tension forces $N_{cb,Rd}$ is obtained:

$$N_{Rd}^{1cb} = \frac{A_{eff} \cdot f_{0.2k}}{\gamma_M} = 5410\ kN \tag{6.3}$$

The latter value of resistance of the cables should be also reduced considering a particular aspect of the construction process. As already mentioned in section 2.1, the two slabs lay on a set of cables arranged in pairs (Figure 2.2a), however all the calculations are made modelling only a single rod with a double cross section: that means that total resistance force of the modelled rods should be two times (6.3); the conditional mood implies ideal conditions for all the construction process.

Looking at the anchorage (Figure 2.2b), it appears evident that a non perfect matching into the two tensile processes must be taken into account. A differential initial tensile state in the cables implies a different stiffness between the two cables, meaning that the total axial force will not be shared equally, as the stiffer cable, with higher initial stress, will carry more than half force. Numerical simulations demonstrate that considering a differential initial tensile state of 10%, which is a quite large number almost imputable to a human error, makes a force distribution in the cables of $\pm 3\%$ with respect of half the total force.

Concluding, an imperfection during the construction process of the steel cables can be considered reducing (6.3) by a coefficient $c_{imp} = 1.03$. The axial force resistance of each pair of cables taken as ultimate limit value for the risk analysis is:

$$N_{Rd} = 2\frac{N_{Rd}^{1cb}}{c_{imp}} = 10500\ kN \tag{6.4}$$

Without considering further security design coefficients in the load combinations reported in the standards' prescriptions, the limit value of the axial force on the cables guarantee alone a coefficient $\gamma = 1.5$ with respect the break load tested by the cable supplying firm.

Table 6.1: Steel cables damage-state brackets.

Level n.	Damage	Criteria	Description
0	none	$N_{dm}^{cb} = 0$	no damage
3	extensive	$N_{dm}^{cb} \leq 2$	breaking of a pair of cables
4	complete	$N_{dm}^{cb} > 2$	collapse of the roof

Table 6.1 reports the damage state brackets as described in the *catastrophe model* of section 1.3.1. In this case the damage state is related only to the number of cables N_{dm}^{cb} which exceed the resistance value (6.4). As already mentioned a cable failure is not acceptable for the security of the stadium, as it will lead to the collapse of the roof. The considered damage-state brackets for this parameter include only the possibility of failure of a single pair of cables as an intermediate level before the total collapse, however even this occur-

rence denotes an *extensive* damage of the structures. Levels of *slight* and *moderate* damage are not considered for the cables failure scenario.

6.1.2

Damage on the slabs

The actual covering over the grandstands is made by two concrete slabs supported by the set of steel cables. The slabs supply the functional part of the roof, i.e. protecting the spectators from the sun and from the rain, but also the structural part because the bending resistance of the shells joins together the set of cables and provide a homogeneous dynamic behaviour. Details about the functional and structural features of the concrete slabs are reported in chapter 2 and chapter 4.

The concrete slabs are built with three layers laid one on the top of the other. On the bottom, just over the cables, there is a layer of cold rolled steel sheets without any significant bending stiffness within the global roof, but which guarantees a transversal axial constrain for the cable set even without the concrete filling. Over this layer, $24.5\ cm$ of reinforced concrete slab are placed, while on the top of the covering package there is a waterproof layer. The slabs are realized using concrete type C30/37 according to the European Code EN 206-1 with $1 + 1\phi 12\ /20cm$ reinforced bars in both directions: hence, the designed value of the resistance to bending moments, equal in both in x and y directions, is:

$$M_{Rd} = \pm 46.67\ kNm/m \tag{6.5}$$

As already mentioned, the achievement of the previous value denotes a heavy state of damage in the structure and even if this does not involve the direct collapse of the roof, it means the loss of the bending resistance of the shells. In other words, the threshold (6.5) is fixed as a limit for the effectiveness of the adopted numerical model and then the suitableness of the obtained results. Consequently the lower value indicating the trigger of the cracking state in the concrete layer is taken into account:

$$M_{cr} = \pm 34.14\ kNm/m \tag{6.6}$$

This chapter is focussed on the damages caused by a windstorm of certain intensity on the roof of the Stadium of Braga. The slabs will be considered damaged when the bending moment on a part of the surfaces overload the cracking bending moment (6.6). Clearly the forming of cracks on a small portion of surface, especially around the edges, does not

compromise the covering functionality as a shelter for the spectators; however increasing the damaged area can produce the complete destruction of the concrete, open gaps in the waterproof layer and subsequently the modification of the global behaviour of the roof with undesirable effects. At the end, a wide-ranging cracked area could drive to the collapse.

Mathematically, the definition of the damage index of the bending moment parameter is divided into two levels: *local* and *global*. The local damage index d_i (Figure 6.2) is defined for every infinitesimal piece of area of the two surfaces; it is calculated as a function of the maximum bending moment of the local area following the condition:

$$d_i = \begin{cases} 0 & M \leq M_{cr} \\ \dfrac{M - M_{cr}}{M_{Rd} - M_{cr}} & M_{cr} < M < M_{Rd} \\ 1 & M = M_{Rd} \end{cases} \tag{6.7}$$

While the global index (6.8) is simply the integral over the whole surface A of (6.7).

$$D_{gl} = \frac{1}{A}\int_A d_i \, dA \tag{6.8}$$

Following the same procedure adopted for the cables, Table 6.2 identifies the damage-state brackets defining the type of damage expected for each level. The criteria of subdivision use the total amount of damaged area calculated by (6.8).

Table 6.2: Concrete slabs damage-state brackets.

Level n.	Damage	Criteria	Description
0	none	$D_{gl} = 0\%$	no damage
1	slight	$D_{gl} < 5\%$	cracked zones only along the edges
2	moderate	$5\% \leq D_{gl} < 15\%$	one evident cracked zone than need to be repaired
3	extensive	$15\% \leq D_{gl} < 50\%$	general damage state all over the roof
4	complete	$D_{gl} \geq 50\%$	bending resistance no more effective

It should be noted that only the configurations where the cracked zones are located along the edges of the two slabs are accepted in the lowest damage-state brackets. The choice concerns the operative mechanism of each slab which has to tie the cables and ensure a jointly behaviour of the structure; this is guaranteed even if the borders are harmed but not if the damage condition split one surface into small pieces. For the latter occurrence only the moderate and extensive brackets are indicated, no matter which is the global damage index.

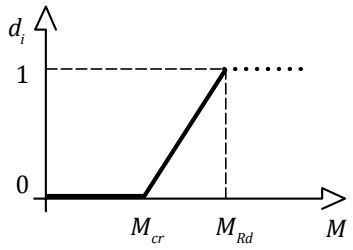

Figure 6.2: Local damage index for the concrete slab resistance.

6.2 PHYSIOLOGICAL DAMAGE

During the planning of a building it is really important to take into account specific parameters about the comfort and the acceptance of its use for the public. In addition to security aspects and limitation of the structural damage due to unpredictable events, the appearance of threats caused by high noise or the sudden movement of the roof, and that can lead to panic, are issued to be managed. This topic that could seem less important than structural design will be fundamental in all the big opera hosting many people.

Considering structural vibrations, the perceptions that such vibrations produce on human beings immediately come to mind. Several national codes and numerous publications attempt to find the best criteria, or at least the most realistic, for the physiological effects due to vibrations. However, this topic is actually too large and there are too many constitutive parameters for an effective common description. Even if an approach should be suitable for pedestrian footbridges, bell towers, chimneys or masts, the details change from case to case especially when focussed the affected people inside the buildings (Bachman, Ammann and Deischl, et al. 1994).

The human reaction to vibrations is strongly related to the surrounding circumstances. Different degrees of personal discomfort arise when influenced by parameters such as the position of the affected person, standing sitting or lying, or the carry out activity, the occurrence in a day and several others (Bachman and Ammann 1987). Obviously, in the same external conditions, the intensity of perception depends also on the objective physical vibration parameters such as the amplitude of the movement, in terms of displacement, velocity or acceleration, the exposure time and the vibration frequency.

In the common practice of the civil engineering, the control about the limitations of the vibrations on any structure is applied on the floor movement where pedestrian walk or

host like for footbridges (Zivanovic, Pavic and Reynolds 2005) or high-rise buildings (Burton, et al. 2006). Similarly, since recent years, specific studies devoted to disorders caused by the wind flow channelled through the buildings have started. In fact such flows in urban environment could be dangerous for pedestrians (Stathopoulos 2009). These concerns enter in the set of the *comfort* issue and the aim is to evaluate the impediments that some situations and events bring in the daily activities of the people.

Another very recent field of study is indeed the valuation of the risk caused by panic situations. In such cases, many people taking part in the same activity stand in the same psychological condition or threat or uneasiness, but these situations do not have objective reasons in the real environment.

In previous sections, mechanical parameters of the structure's resistance have been thoroughly defined. Experimental data show that the roof is so flexible that even in rare and extreme situations it can easily pass resistance tests, notwithstanding the presence of movements in the order of magnitude of one meter. The effect that here it should be considered is if such a movement, with frequencies detectable by the human eye, with frequency in the order of seconds, can generate a feeling of anxiety that may lead to fear and/or panic in the crowd.

Looking for Code's prescription regarding this topic, the second part of Standard DIN 4150 deals with the effects of vibrations from mostly external sources on people in residential building. The frequencies considered range from 1 to 80 Hz. Measured vibration quantity (displacement, velocity, acceleration) serve as input for an empirically derived *intensity of perception*, called KB value and defined as:

$$KB = d\frac{0.8\,f^2}{\sqrt{1 + 0.032\,f^2}} \tag{6.9}$$

where d is the displacement amplitude (mm) and f is the vibration frequency (Hz). Other equations similar to (6.9) relates KB with velocity and acceleration further than the frequency.

Equation (6.9) implies that generally, fixed an intensity of perception value, the relation between displacements and tolerable frequencies assumes the shape of an hyperbola function $KB \propto d \cdot f^{\alpha}$, in which the proportionality coefficient and the exponent are typical for every specific situation. In the previous, the DIN Standard 4150 is focussed on the comfort threshold that persons can stand when the floor under their feet start oscillating.

6.2.1

Visual discomfort due to roof's vibration

Considering the effects that a wind storm should produce during a sporting or cultural event, when case study of the stadium of Braga is full of spectators, it is relevant to evaluate the safety conditions on the stadium. Figure 6.3 and Table 6.3 show the acceptable values of displacement amplitude and vibration frequency of the roof in order to not generate fear or panic in the public.

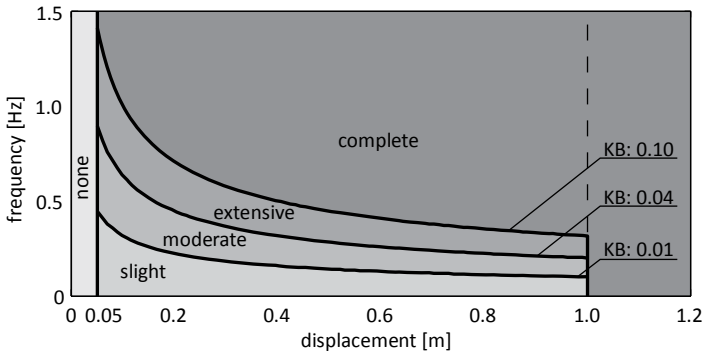

Figure 6.3: Roof vibration damage-state brackets.

The acceptance criteria divide the whole domain into five damage states from 0 to 4. For roof's vibrations with maximum amplitude lower than $5\ cm$ no relevant oscillations are noticed, hence the damage-state level is considered zero. On the other extreme, for oscillations greater than $1\ m$ it is considered that the movement would produce panic on the public with consequent high probability of a dangerous evacuation. The intermediate damage-states follow the definition of the intensity of perception function (6.10) where all the coefficients have been inserted directly in the KB values.

$$KB = df^2 = \begin{cases} 0.01 & \text{slight damage} \\ 0.04 & \text{moderate damage} \\ 0.10 & \text{extensive damage} \end{cases} \tag{6.10}$$

Table 6.3: Roof vibration damage-state brackets.

Level n.	Damage	Criteria	Description
0	none	$d < 0.05\ m$	no relevant oscillations
1	slight	$KB < 0.01$	small oscillation
2	moderate	$KB < 0.04$	visible oscillations: disturbing
3	extensive	$KB < 0.10$	evident oscillations: start fear
4	complete	$d \geq 1.0\ m$	dangerous oscillations: panic in the crowd

6.3 RISK ON THE STADIUM OF BRAGA

Following the definitions given in chapter 1 on the risk analysis, all the steps of the *risk management chain* of Figure 1.5 have been carefully treated in the last chapters of this work allowing to calculate the risk that a certain level of damage in the roof of the stadium of Braga will occur. The complete computation implies the simulation of several events with different annual exceedance probability of occurrence, calculating for each test the damage levels of the roof for both structural and psychological damages. The applied formulae of risk is the simplified version given in (1.2) which does not need the explicit definition of probability density distribution, since all the uncertainties are globally stored into the probability that these events will happen.

Table 6.4: Simulation schedule.

Wind direction	$\theta = 220°$	$\theta = 270°$	$\theta = 310°$	$\theta = 350°$	$\theta = 40°$
100-years wind speed	$55.13\ m/s$	$46.19\ m/s$	$40.74\ m/s$	$39.35\ m/s$	$39.20\ m/s$
Hazard Intensity			Annual Exceedance Probability		
(b.l. wind speed)	p	p	p	p	p
$U = 10\ m/s$	1.0000	1.0000	1.0000	1.0000	1.0000
$U = 20\ m/s$	1.0000	1.0000	1.0000	1.0000	1.0000
$U = 30\ m/s$	0.9998	0.9248	0.5572	0.4286	0.4155
$U = 40\ m/s$	0.6125	0.1050	0.0141	0.0073	0.0068
$U = 50\ m/s$	0.0538	0.0019	0.0001	0.0000	0.0000
$U = 60\ m/s$	0.0017	0.0000	0.0000	0.0000	0.0000

Table 6.4 details the schedule of the set of tests made over the stadium of Braga. Considering five directions of the wind from Southwest to Northeast, namely 220° 270° 310° 350° and 40° with respect the North (Figure 6.4), six simulations with different possible events are run. The events are characterized by gradient wind speed, according to the definitions given in chapter 2, which increase from 10 to $60\ m/s$. For each event the annual exceedance probability is calculated using (2.21) where the reference 100-years event has been taken from Figure 2.10d and written on the second row of the table. Hence the hazard intensity depends only by wind speed, but the probability of the hazard is related also to the direction of the wind.

6.3.1 Computation of the wind-induced damage

In order to better explain the obtained results, one single trial is here extensively described, pointing out how the resulting values have been obtained; afterwards three conclusive tables summarize the risk induced by windstorms events. Usually, in the applied

literature, the risk is expressed in monetary terms, however it is expressed here just as a pure number indicating the sum of several damage level. The correct interpretation of the values is left to the last chapter during the conclusions.

The considered simulation is taken assuming a windstorm coming from the West direction ($\theta = 270°$) and the reference wind speed at the gradient height equal to $30\ m/s$. Looking at Table 6.4, this event has the probability of occurrence of 92.5% every year.

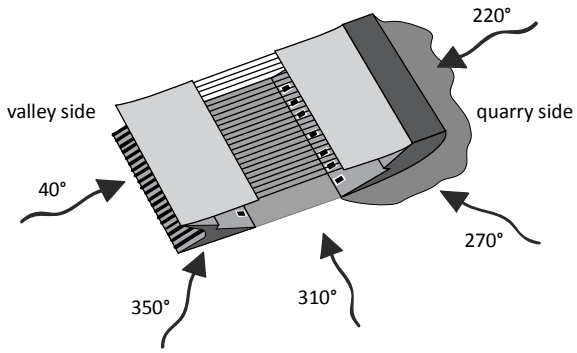

Figure 6.4: Considered wind direction on the simulation events.

Figure 6.5-6.8 show the first four proper modes of the displacement field resulting from the simulation: the theory of the decomposition into proper modes is explained in section 3.1. These graphs highlight the deflection evolution during the event in time and frequency domain. Using this graphic, it appear handy the extrapolation of a limited number of maximum vertical displacement with relative frequency of oscillation in order to compute the intensity of perception (6.10). Figure 6.9 illustrate the damage levels for the visual effects due to the roof motion. The diamond markers indicate the couples of deflection/frequency values related to 15 different modes of which just the first four are visualized. From that graph it can be assessed that the visual damage state for the considered event is 2-*moderate*, since it is the worst level reached by the markers.

From the structural point of view, Figure 6.10 depicts the damage levels on the cables and on the slabs jointly. Regarding the event under exam, the maximum tensile force in a pair of cables is $6693\ kN$, less than the reference value $10500\ kN$ as reported in (6.4), thus none of the steel cables overcome the resistance and, according to the Table 6.1, the damage state is 0-*none*. Differently, the slab conditions show evident zones depicted with light grey where the bending moment exceeds the cracking limit (6.6) and also zones in dark grey where the bending moment exceeds the resistance of the slabs (6.5). According to the definitions in (6.7) and (6.8), the global damage index of the slabs for the events is 45.31% which corresponds to a level 3-*extensive* in Table 6.2.

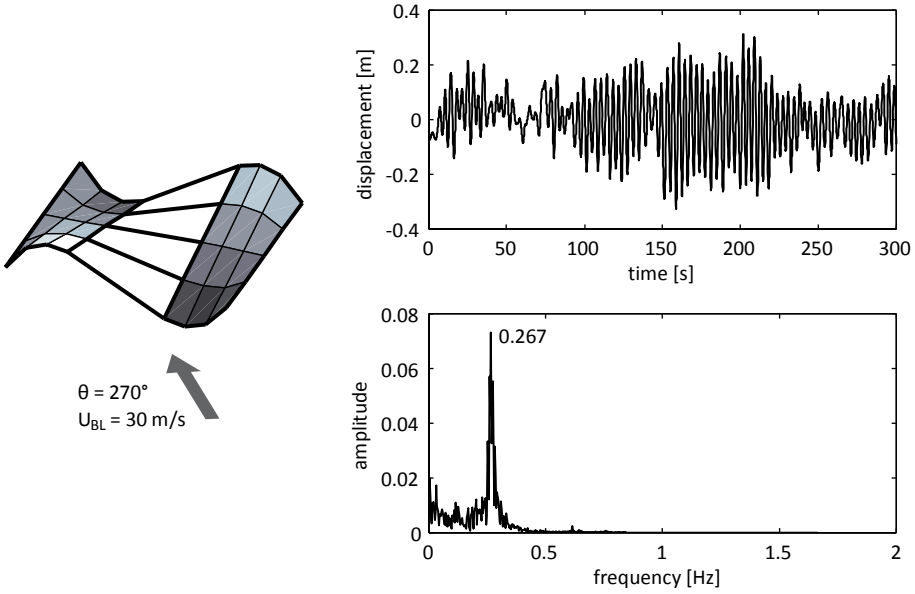

Figure 6.5: Displacement evolution on the stadium's roof. Proper mode number 1.

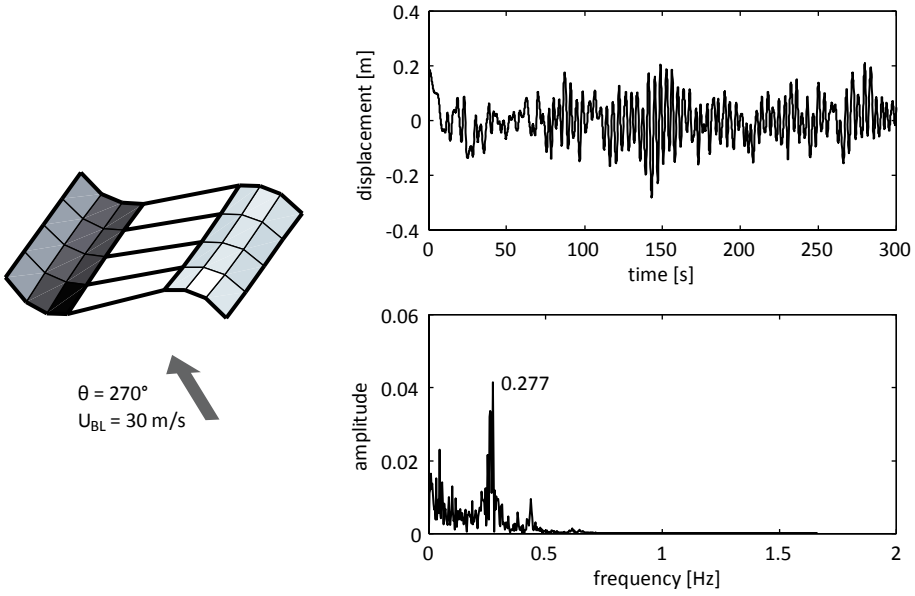

Figure 6.6: Displacement evolution on the stadium's roof. Proper mode number 2.

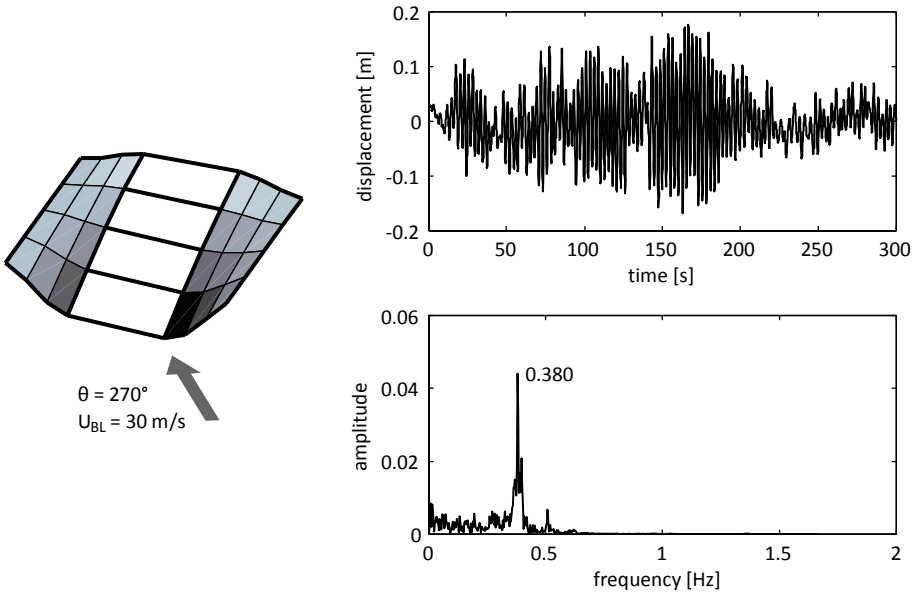

Figure 6.7: Displacement evolution on the stadium's roof. Proper mode number 3.

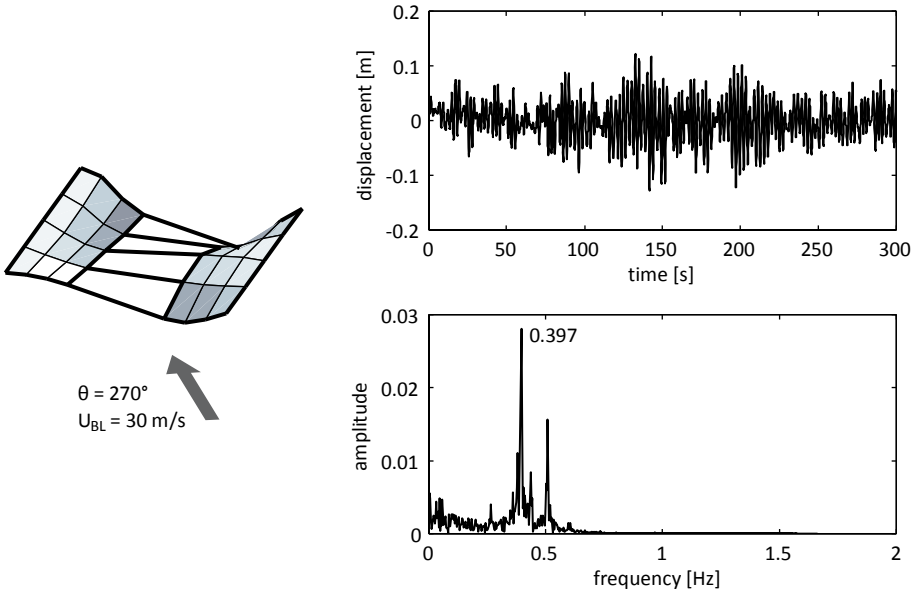

Figure 6.8: Displacement evolution on the stadium's roof. Proper mode number 4.

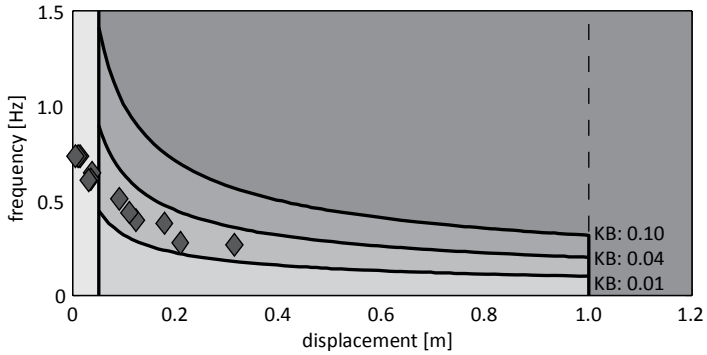

Figure 6.9: Roof vibration damage-state brackets.

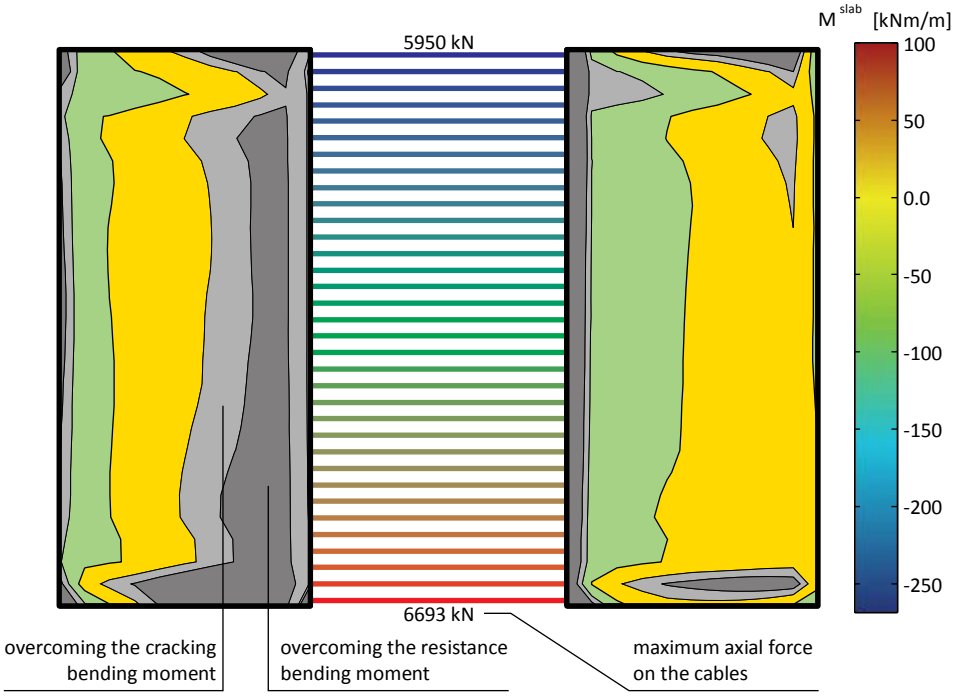

Figure 6.10: Structural damage condition of the roof.

The previous explanation illustrate the way how is has been calculate the three different levels of risk in the stadium's roof. Table 6.5-6.7 resume the results of all the analyses.

Looking deeply at the obtained results some comments can be done. Firstly, Table 6.5 reports that the probability of failure of the steel cables bearing the whole roof is zero. This

data is certainly comforting for the spectators who can watch all the football matches surely that anything will fall to their heads without a clear forewarning. On the other side, a technician is rightly prudent reading that the risk of collapse for every intensity of the gales is zero, especially when he notes that the maximum axial force on the cables does not change of a single kilo Newton during the 30 trials.

Investigating these results, it can be noted that the design process of the roof provides no intermediate constraints on the cables; this choice implies foreseeable huge deflections without an addition of stress in the cables. The first and energetically most important modes of vibration have an antisymmetric shape, thus a vibration through the stable configuration does not imply any relevant elongation leading to an increasing of stress. It should be also noted that the structure satisfies several Code's prescription regarding the safety against the collapse, and even a minimal increase in the resistance cross-sections of the cables knocks down the risk of collapse of some order of magnitude.

A complete different situation appears from Table 6.6. The cracking situation of the two concrete slabs has roused anxiety since the earlier construction processes, because the covering is evidently too big with respect its thickness. The worries find confirmation in the presented results. The flexible supports, given by the set of cables, impose unacceptable deflections for the slabs, therefore an impressive amount of cracks appear even with the weakest live loads and they rise very fast increasing the windstorm intensity. The grey zones depicted in Figure 6.10 illustrate a typical situation with a normal storm.

The extensive cracking damage state, noted for all the normal load conditions, justifies the choice of modelling the structures imposing one-half of the designed concrete elastic modulus. The choice was initially related to the natural frequency comparison between the full-scale test and the simulations (see section 4.6), and it found confirmation in these final results when plotting the bending moment contours.

The serviceability constraints pointed out in section 6.2 are summarized in Table 6.7 where the highest value of intensity of perception KB is highlighted for each event, specifying the maximum deflection amplitude and related frequency of vibration. Differently from the structural components, this damage parameter is highly influenced by the intensity of the windstorms: for every direction the weaker events produce small oscillations, identified with the lower damage states; while increasing the wind speed gives rise to larger oscillation with an almost direct proportionality. The described behaviour is evident, but it is really important to underline that a correct structural design should avoid any problem for the component's resistance caused by wind-induced loads, while specific mitigation devices are suitable in order to limit the displacements in the serviceability limit states.

Table 6.5: Resume of the risk of collapse of the steel cables.

Wind direction: 220°					
Wind speed $[m/s]$	Annual exc. probability	Maximum axial force $[kN]$	N_{dm}^{cb}	Damage level (Table 6.1)	Risk on cables
10.0	1.0000	6693.0	0	0-*none*	0.0000
20.0	1.0000	6693.0	0	0-*none*	0.0000
30.0	0.9998	6693.0	0	0-*none*	0.0000
40.0	0.6125	6693.0	0	0-*none*	0.0000
50.0	0.0538	6693.0	0	0-*none*	0.0000
60.0	0.0017	6693.0	0	0-*none*	0.0000
Wind direction: 270°					
Wind speed $[m/s]$	Annual exc. probability	Maximum axial force $[kN]$	N_{dm}^{cb}	Damage level (Table 6.1)	Risk on cables
10.0	1.0000	6693.0	0	0-*none*	0.0000
20.0	1.0000	6693.0	0	0-*none*	0.0000
30.0	0.9248	6693.0	0	0-*none*	0.0000
40.0	0.1050	6693.0	0	0-*none*	0.0000
50.0	0.0019	6693.0	0	0-*none*	0.0000
60.0	0.0000	-	-	-	-
Wind direction: 310°					
Wind speed $[m/s]$	Annual exc. probability	Maximum axial force $[kN]$	N_{dm}^{cb}	Damage level (Table 6.1)	Risk on cables
10.0	1.0000	6693.0	0	0-*none*	0.0000
20.0	1.0000	6693.0	0	0-*none*	0.0000
30.0	0.5572	6693.0	0	0-*none*	0.0000
40.0	0.0141	6693.0	0	0-*none*	0.0000
50.0	0.0001	6693.0	0	0-*none*	0.0000
60.0	0.0000	-	-	-	-
Wind direction: 350°					
Wind speed $[m/s]$	Annual exc. probability	Maximum axial force $[kN]$	N_{dm}^{cb}	Damage level (Table 6.1)	Risk on cables
10.0	1.0000	6693.0	0	0-*none*	0.0000
20.0	1.0000	6693.0	0	0-*none*	0.0000
30.0	0.4286	6693.0	0	0-*none*	0.0000
40.0	0.0073	6693.0	0	0-*none*	0.0000
50.0	0.0000	-	-	-	-
60.0	0.0000	-	-	-	-
Wind direction: 40°					
Wind speed $[m/s]$	Annual exc. probability	Maximum axial force $[kN]$	N_{dm}^{cb}	Damage level (Table 6.1)	Risk on cables
10.0	1.0000	6693.0	0	0-*none*	0.0000
20.0	1.0000	6693.0	0	0-*none*	0.0000
30.0	0.4155	6693.0	0	0-*none*	0.0000
40.0	0.0068	6693.0	0	0-*none*	0.0000
50.0	0.0000	-	-	-	-
60.0	0.0000	-	-	-	-
				Total wind-induced risk on the steel cables:	0.0000

Table 6.6: Resume of the risk of cracking of the concrete slabs.

Wind direction: 220°					
Wind speed $[m/s]$	Annual exc. probability	Global damage index east slab	Global damage index west slab	Damage level (Table 6.2)	Risk on slabs
10.0	1.0000	31.86%	18.62%	3-*extensive*	3.0000
20.0	1.0000	30.77%	18.69%	3-*extensive*	3.0000
30.0	0.9998	34.84%	21.63%	3-*extensive*	2.9994
40.0	0.6125	61.20%	30.13%	4-*complete*	2.4500
50.0	0.0538	87.08%	55.76%	4-*complete*	0.2152
60.0	0.0017	91.08%	70.98%	4-*complete*	0.0068
Wind direction: 270°					
Wind speed $[m/s]$	Annual exc. probability	Global damage index east slab	Global damage index west slab	Damage level (Table 6.2)	Risk on slabs
10.0	1.0000	32.70%	18.49%	3-*extensive*	3.0000
20.0	1.0000	37.23%	17.93%	3-*extensive*	3.0000
30.0	0.9248	45.31%	15.50%	3-*extensive*	2.7744
40.0	0.1050	49.88%	26.62%	3-*extensive*	0.3150
50.0	0.0019	54.12%	47.06%	4-*complete*	0.0076
60.0	0.0000	-	-	-	-
Wind direction: 310°					
Wind speed $[m/s]$	Annual exc. probability	Global damage index east slab	Global damage index west slab	Damage level (Table 6.2)	Risk on slabs
10.0	1.0000	32.20%	18.58%	3-*extensive*	3.0000
20.0	1.0000	34.13%	18.17%	3-*extensive*	3.0000
30.0	0.5572	39.30%	20.04%	3-*extensive*	1.6716
40.0	0.0141	52.41%	43.99%	4-*complete*	0.0564
50.0	0.0001	68.31%	62.55%	4-*complete*	0.0004
60.0	0.0000	-	-	-	-
Wind direction: 350°					
Wind speed $[m/s]$	Annual exc. probability	Global damage index east slab	Global damage index west slab	Damage level (Table 6.2)	Risk on slabs
10.0	1.0000	31.57%	18.62%	3-*extensive*	3.0000
20.0	1.0000	31.56%	19.78%	3-*extensive*	3.0000
30.0	0.4286	32.46%	36.34%	3-*extensive*	1.2858
40.0	0.0073	51.66%	60.23%	4-*complete*	0.0292
50.0	0.0000	-	-	-	-
60.0	0.0000	-	-	-	-
Wind direction: 40°					
Wind speed $[m/s]$	Annual exc. probability	Global damage index east slab	Global damage index west slab	Damage level (Table 6.2)	Risk on slabs
10.0	1.0000	31.74%	18.59%	3-*extensive*	3.0000
20.0	1.0000	32.22%	18.56%	3-*extensive*	3.0000
30.0	0.4155	31.17%	22.35%	3-*extensive*	1.2465
40.0	0.0068	72.01%	41.00%	4-*complete*	0.0272
50.0	0.0000	-	-	-	-
60.0	0.0000	-	-	-	-
			Total wind-induced risk on the concrete slabs:		43.0855

Table 6.7: Resume of the risk for induced fear due to the roof's vibration.

Wind direction: 220°						
Wind speed $[m/s]$	Annual exc. probability	Maximum intensity of perception $d\ [m]$	$f\ [Hz]$	KB	Damage level (Table 6.3)	Risk for vibrations
10.0	1.0000	0.016	0.510	0.004	0-*none*	0.0000
20.0	1.0000	0.041	0.380	0.006	0-*none*	0.0000
30.0	0.9998	0.323	0.277	0.025	2-*moderate*	1.9996
40.0	0.6125	0.379	0.383	0.056	3-*extensive*	1.8375
50.0	0.0538	0.703	0.397	0.111	4-*complete*	0.2152
60.0	0.0017	0.692	0.390	0.105	4-*complete*	0.0068
Wind direction: 270°						
Wind speed $[m/s]$	Annual exc. probability	Maximum intensity of perception $d\ [m]$	$f\ [Hz]$	KB	Damage level (Table 6.3)	Risk for vibrations
10.0	1.0000	0.019	0.510	0.005	0-*none*	0.0000
20.0	1.0000	0.126	0.280	0.010	1-*slight*	1.0000
30.0	0.9248	0.313	0.267	0.022	2-*moderate*	1.8496
40.0	0.1050	0.861	0.273	0.064	3-*extensive*	0.3150
50.0	0.0019	1.121	0.283	0.090	3-*extensive*	0.0057
60.0	0.0000	-	-	-	-	-
Wind direction: 310°						
Wind speed $[m/s]$	Annual exc. probability	Maximum intensity of perception $d\ [m]$	$f\ [Hz]$	KB	Damage level (Table 6.3)	Risk for vibrations
10.0	1.0000	0.020	0.510	0.005	0-*none*	0.0000
20.0	1.0000	0.115	0.277	0.009	1-*slight*	1.0000
30.0	0.5572	0.241	0.380	0.035	2-*moderate*	1.1144
40.0	0.0141	1.087	0.273	0.081	3-*extensive*	0.0423
50.0	0.0001	1.702	0.273	0.127	4-*complete*	0.0004
60.0	0.0000	-	-	-	-	-
Wind direction: 350°						
Wind speed $[m/s]$	Annual exc. probability	Maximum intensity of perception $d\ [m]$	$f\ [Hz]$	KB	Damage level (Table 6.3)	Risk for vibrations
10.0	1.0000	0.020	0.510	0.005	0-*none*	0.0000
20.0	1.0000	0.113	0.380	0.016	2-*moderate*	2.0000
30.0	0.4286	0.245	0.380	0.035	2-*moderate*	0.8572
40.0	0.0073	0.998	0.273	0.075	3-*extensive*	0.0219
50.0	0.0000	-	-	-	-	-
60.0	0.0000	-	-	-	-	-
Wind direction: 40°						
Wind speed $[m/s]$	Annual exc. probability	Maximum intensity of perception $d\ [m]$	$f\ [Hz]$	KB	Damage level (Table 6.3)	Risk for vibrations
10.0	1.0000	0.021	0.510	0.005	0-*none*	0.0000
20.0	1.0000	0.116	0.273	0.009	1-*slight*	1.0000
30.0	0.4155	0.391	0.263	0.027	2-*moderate*	0.8310
40.0	0.0068	0.789	0.263	0.055	3-*extensive*	0.0204
50.0	0.0000	-	-	-	-	-
60.0	0.0000	-	-	-	-	-
					Total wind-induced risk for the roof's vibration:	14.1170

6.4

MITIGATION DEVICE

The results obtained in the previous set of simulations point out the impact of the wind action on the safety of all the structural components of the roof. On balance, it appears that the structure is so flexible to avoid any increment of stress caused by the dynamic wind loads. Actually the tensile force on the cables does not change in any simulated event (Table 6.5); while the slabs are in an extensive state of cracking even under the permanent load conditions and just a slight dynamic wind pressure enlarge the damaged zone until covering all the surfaces (Table 6.6). The last comment brings through the acceptance of the actual situation as a design input thus a structural model should simply include a reduction in the bending stiffness of the concrete slabs.

Hypotheses to restore a suitable non-cracking state on the concrete layers, or at least limiting the extension, should include large modification in the original project applying an additional load bearing stiffer structure to support or substitute the set of steel cables. Otherwise it can be considered to considerably increase the slab thickness which will produce also an increasing of permanent loads; the latter suggestion implies the complete demolition and rebuilding of the whole covering. These kinds of variations cannot be considered as risk reduction on the stadium's roof, because they completely change the original system and this is not provided in the present work.

Looking at the serviceability load conditions, Table 6.7 shows the true limitations of the roof of the stadium of Braga as a result of dynamic actions. Under an increasing wind pressure, the produced oscillations start easily to synchronize themselves with the wind fluctuation amplifying dangerously the deflections. The effect could compromise the reliability of technological devices hanged up to the roof, spotlights and loud speakers, besides the possibility of creating fear on the spectators.

Differently from the stress limitation on the concrete slabs, the reduction of oscillation amplitude is easily achievable and attractive. The mitigation system can be composed by a set of external damping devices which avoids any resonance effect by limiting the oscillation amplitude starting from the very beginning of the phenomenon. The devices should be installed at the very end of the two slabs in the nearness of the truss-beams where the deflections are greater and thus the damping effect will be enhanced.

More in detail, the external damping devices have to apply a vertical visco-elastic force to the roof central span keeping one end anchored to the ground floor (Figure 6.11). Considering the dimensions of the stadium and the maintenance service needed for this kind of devices, it appear suitable to install the damping devices under the ground level and link

them with the covering by using a set of ropes almost 40 meters long. There are two comments to do on the proposed devices. Firstly, it can be assumed that the ropes will be not always fixed to the devices but installed with electric hoists on the roof; the ropes should be unrolled and linked to the damping devices only when necessary. In this way, the usual aspect of the stadium will be not modified from the original idea chosen by the architect, without any connection in the middle of the span. As a drawback, it must be noted that linking the damping devices with flexible ropes halves the efficiency of the external damping forces, which could work only when the ropes are stretched that is when the oscillation drives the roof to going up. Moreover, in order to let the devices working properly during several cycles, a set of torsion spring have to be inserted to maintain the ropes perfectly straights during the compression phases, that means when the roof is going down; without these mechanisms the breaking force will not be ready for the change of direction.

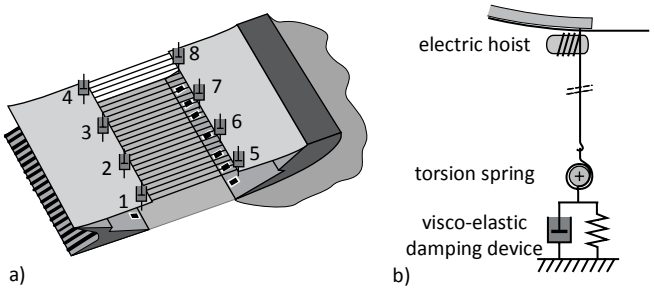

Figure 6.11: External damping device: a) position of the devices; b) scheme of one mechanism.

6.4.1

Design of the suitable damping force

The design of the damping device is made as a function of the maximum force it should be able to apply. In order to define the required value, the complete structure is globally simplified with a single degree of freedom which oscillates vertically under the dynamic wind action. The process of simplification leads to apply all the mass of the roof to the first natural frequency calculating the equivalent stiffness related to the first modal shape.

Table 6.8 reports all the dynamic characteristics of the single degree of freedom which globally replace the stadium roof, moreover, the maximum expected motion parameters, namely displacement velocity and acceleration, obtained from the simulations in section 6.3, are reported. By using these data, it is possible an estimation of the maximum internal force of the system:

Table 6.8: Dynamic characteristics of the roof: single degree of freedom.

mass	M	=	10.50×10^6	*kg*
structural circular frequency	ω	=	1.74	*rad/s*
stiffness	K	=	31.80×10^6	*N/m*
structural damping ratio	ξ_{st}	=	0.50 %	
damping coefficient	C	=	0.18×10^6	*N·s/m*
maximum deflection	z_{max}	=	1.00	*m*
maximum velocity	$\dot{z}_{max}$	=	0.50	*m/s*
maximum acceleration	$\ddot{z}_{max}$	=	1.50	m/s^2

$$M\ddot{z}_{max} + C\dot{z}_{max} + Kz_{max} \cong 48000\ kN \tag{6.11}$$

Starting from the previous reference value, it has been decided to design the visco-elastic damping devices which apply a maximum damping force of $10000\ kN$ globally: almost 1/5 of the internal force of the system. Following the indications of a producer company (FIP) for non-linear viscous damper, the total force could be split into elastic and viscous components assigning the 90% to the latter part.

$$F_{dd} = \underbrace{k_{dd} \cdot z}_{10\%} + \underbrace{c_{dd} \cdot \dot{z}^{\alpha}}_{90\%} \tag{6.12}$$

Sharing the total force into 8 points (see Figure 6.11a), Table 6.9 reports the attributes of a single device (Figure 6.11b):

Table 6.9: Characteristics of a single damping device.

Maximum force	F_{dd}	=	1.25×10^3	*kN*
Elastic constant	k_{dd}	=	1.25×10^2	*kN/m*
Viscous damping coefficient	c_{dd}	=	1.25×10^3	*kN·s/m*
exponent	α	=	0.15	

6.4.2

Results after the mitigation device

The mitigation device system formerly described is designed with the purpose of limiting the oscillation amplitude without modifying the global behaviour of the roof: modal shapes and natural frequencies. Consequently, it has been chosen to relate the braking forces mainly on the velocity of the structure by using the viscous damping, and to share the total force into middle span points further than the four corners. The obtained results are in line with the intentions confirming a significant reduction in the motion vibration maintaining unaffected the global dynamic performance of the roof, i.e. without any in-

creasing of stress in the steel cables but also without a considerable reduction of the cracking state in the two slabs.

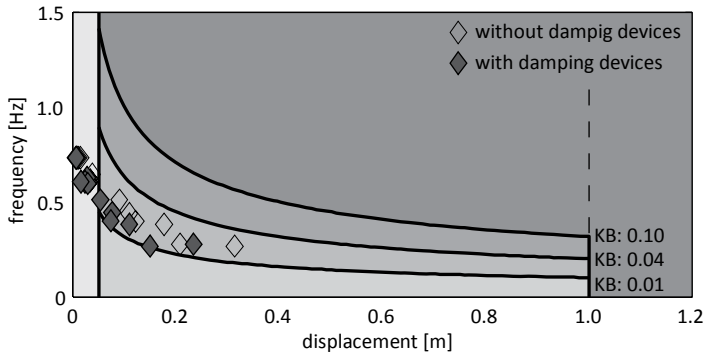

Figure 6.12: Roof vibration damage-state brackets after mitigation.

Figure 6.12 reports the damage levels for visual comfort. The simulation follows the same input used for Figure 6.9 with the addition of the set of damping devices (Figure 6.11). The dark markers are referred to the mitigated results, while the light ones are taken from Figure 6.9. It can be noted that all the markers maintain the same frequency but they are shifted to the left, toward lower deflection amplitude. In the depicted case ($\theta = 270°$, $U_{BL} = 30\ m/s$), the lowering of the damage curve is not big enough for a jump into the lower brackets; however in several other trials the mitigation system drives to jumps of one or even two damage levels.

Filling Table 6.1 with the values of intensity of perception KB reduced by the effects of the damping devices, the new value of total wind induced risk for the roof's vibration equal to 9.3300 is obtained. Comparing the two quantities it can be assessed that the designed mitigation system produces a risk reduction for visual comfort of the 33%. It is stressed that the two pure values of risk: 14.1170 and 9.3300 are meaningless without a suitable quantification in physical or monetary terms of the damage levels. Nevertheless, imposing the same conditions and criteria for the two set of simulations, these values are certainly comparable, giving significance to the efforts accomplished for the risk reduction.

CHAPTER 7

DISCUSSION AND CONCLUSIONS

All scientific disciplines, including civil engineering, have recently risen the consciousness that any activity performed to achieve benefits involves a certain degree of risk. Given that it is difficult, rather than impossible, a reliable prediction of the perils with a considerable advance, a general formulation of the risk management provides the best executive tool supporting the decision-making process defining the order of precedence. The crucial step is the intrinsic multidisciplinary character of the topic, which involves actors from several different fields and backgrounds; this feature drives to a fast growth of misunderstandings and confusion both in relationships and in the substance.

In the present dissertation a wide review of several schemes of risk assessment has been made. It has been shown how a direct entry of the risk management chain provides clearer results, mostly because the chain rings represent specific physical quantities which have to be calculated in sequence from different technicians. A great advantage is that, in a single step, the technician should worry only about the connectors between the previous and the following steps, input and output, without bearing in mind the whole context. This feature means modularity, reliability, and rapidity of execution. The complete risk management process is clarified by an application to a real building appropriate for an extensive structural investigation.

The case study aims to assess the effects of wind actions on the covering of the stadium of Braga, Portugal. The attention is focussed on severe windstorms, hence identifying the *Nature* as promoter of the catastrophes, and investigating the exposure of the stadium to harmful wind events. The procedure demands the definition of physical quantities which explain how much the system is affected by the hazard, no matter how. In the case study, wind loads on the stadium's roof, expressed in terms of pressure on the two slabs, are computed by using a combination of true meteorological data and wind tunnel tests carried out during the real design process.

Particular emphasis is given to the introduction of some preliminary concepts about data analysis and data storing, explaining the attractive features of the *proper orthogonal decomposition* (POD), extensively adopted both in pre- and post-processing. POD technique is successfully used for the manipulation of the wind tunnel pressure fluctuations achieving a versatile data set for the finite element analyses. Moreover, the same orthogonal decomposition is used to show the structural motion highlighting the modal shapes and the evolution of the motion in time and frequency domain.

The central part of the thesis is the development and the set-up of a complete numerical model of the roof. The model uses the subroutines of the research code *Kratos* in which a couple of finite elements have been implemented, namely a truss and a shell element. In particular, the shell element includes a good consistency of important results of the last twenty years in the computational research, like the *DKT theory* and the *ANDES template*, merging the components with the *direct fabrication approach* and projecting everything in a *corotational formulation*. It has been proofed that the numerical model is able to perfectly reproduce the dynamic behaviour of the roof with a simple adjustment of the concrete elastic modulus in order to take into account the cracking state of the slabs. The mentioned dynamic characteristics are compared with the full-scale tests carried out by two teams on the built-up stadium.

Furthermore, the thesis addresses a consistent and operative procedure aimed at assessing the aerodynamic damping on the stadium's roof. The assessment consists in a linearised truncation of the damping coefficient, which provides good results in flexible covering structures when the incoming flow remains much bigger than the structural motion. The enhancement provides an increment of 50% to 100% of damping ratio respect to the original value, which takes into account only the structural damping mechanisms. The bigger values are related to greater wind speeds; this means that neglecting the whole phenomenon implies a considerable over-design of load bearing components especially in flexible coverings. The reliability of the obtained results has been successfully tested with a specific patch test, where the estimation of the motion of a cylindrical chimney subjected to a constant wind speed is compared with results from a CFD analysis. In the latter test, the main goal is to demonstrate the ability of the proposed damping linearization to properly represent the behaviour of the system before the vortex shedding starts, which is a phenomenon that does not involve long-span roofs.

The last developed step of the risk management chain is the definition and the quantification of the damage states on the roof. Three different scenarios have been considered, namely: failure of the steel cable, failure of the concrete slabs and severe oscillations of the whole roof. The different damage scenarios are used to quantify the risk levels separately, because it is not possible to fulfil the complete risk quantification without the defi-

nition and the computation of the losses. In fact, it is the last chain ring, named *Losses*, that converts and joins all the separated damage states into a unique monetary value which, when related to a period of occurrence, returns the *Risk*. The monetary aspects are left to future investigation and not treated within the present work; on the contrary, the risk is quantified with pure values requiring a conversion table to be used by the decision maker. Another prospect for the obtained values is considering an alternative scenario, for instance a modification of the system, in order to mitigate the resulting risk of failure. Maintaining unchanged all the boundary conditions, a comparison of resulting risk values in terms of percentage fractals is suitable even without the conversion into monetary terms.

The results show completely different behaviours of the first two damage scenarios, related to ultimate resistance of structural components, and the third scenario related to problems of serviceability. In particular, it can be noted that an appropriate over dimensioning of the steel cables, following the European Standards' prescriptions, makes any detailed risk investigation fruitless because the usual safety coefficients for loads and materials pull down the risk values of several order of magnitude. The situation of the concrete slabs' damage is slightly different because the constant damage state is the consequence of a precise design choice and it is not properly related to the wind action.

More interesting results are obtained looking for the mitigation of oscillations which can cause fear or panic to the public. Simulation outcomes clarify the period of occurrence of different intensity of perception, making clearer the definition of acceptance criteria. Moreover, the design of a suitable set of damping devices has proved its reliability into a reduction of oscillation in global terms of about one third. The quantification of the effects of the proposed mitigation systems has been possible by applying the risk approach, which turns out to be an interesting method for complete costs-benefits analyses.

Concluding, it should be remarked that the calculation of risk proposed in this study remains at a stage of structural risk, missing the computation of the possible consequences caused by windstorms. A desirable improvement consists in integrating the procedure with socio-economic aspects, in order to conclude the risk management chain producing a complete result.

APPENDIX

BAYES' RULE A

In the Bayesian interpretation the probability P(A) of the event A is formulated as a *degree of belief* that A will occur. The degree of belief is a reflection of the state of mind of the individual person in terms of experience and preferences. The Bayesian statistical interpretation of probability is personal-dependent but the subjectivity should be based on experience from previous trials, like in the frequentistic definition of P(A), as well as considering the objective nature of the problem, like in the classical definition (Faber 2006).

Given two sets A and B with assigned probabilities P(A) and P(B) respectively, the conditional probability of B given A is defined as:

$$P(B|A) = \frac{P(A \cap B)}{P(A)} \tag{A.1}$$

where $A \cap B$ is the intersection sets that proves $P(A)$ is greater than zero.

Considering that the whole set $\Omega = A_1 \cup A_2 \cup \dots A_n$ composed by n mutually exclusive subsets A_i, and let X be an arbitrary se; the *total probability* theorem provides:

$$\begin{aligned} P(X) &= P(X \cap A_1) + P(X \cap A_2) + \cdots P(X \cap A_n) \\ &= P(X|A_1)P(A_1) + P(X|A_2)P(A_2) + \cdots P(X|A_n)P(A_n) \end{aligned} \tag{A.2}$$

From (A.1) it is $P(X|A_i)P(A_i) = P(X \cap A_i) = P(A_i|X)P(X)$, implying that:

$$P(A_1|X) = \frac{P(X|A_i)}{P(X)} P(A_i) \tag{A.3}$$

The above formula presents the denominator for the Bayes' rule:

$$P(A_i|X) = \frac{P(X|A_i)P(A_i)}{\sum_j P(X|A_j)P(A_j)} \tag{A.4}$$

showing how one conditional probability depends on its inverse. In other terms, it is derived how the probability $P(A_i|X)$ of an event A_i given observed evidence X is related to the probability of that evidence given the event $P(X|A_i)$.

Using (A.4), the *priory probability* of an event $P(A_i)$ is updated by the observation of the evidence X defining the *posteriori probability* $P(A_i|X)$.

APPENDIX B

GUMBEL DISTRIBUTION

The Gumbel distribution, also known as the extreme value Type 1 distribution, is the most widely applied statistical distribution for problems in civil engineering. Applications of the distribution includes the frequency analysis of the most important natural hazards, i.e. floods windstorms earthquake, joint with other risk-based engineering like offshore structures and nuclear power plants, but also totally different fields, for instance queues in supermarkets, horse racing, etc. (Kotz and Nadarajah 2000).

The distribution, named after the German mathematician E.J. Gumbel, is used to determine the distribution of the maximum values of samples from different other distributions. Its major application area is in forecasting that extreme natural disasters will occur, given maximum events intensity of the past years.

The *cumulative distribution function* is expressed in reference of two parameters: the location parameter α and the scale parameter β:

$$P(x) = \exp\left[-\exp\left(-\frac{x-\alpha}{\beta}\right)\right] \tag{B.1}$$

while its *probability density function* is:

$$f(x) = \frac{1}{\beta}\exp\left[-\frac{x-\alpha}{\beta} - \exp\left(-\frac{x-\alpha}{\beta}\right)\right] \tag{B.2}$$

Other typical statistics that summarize a statistical distribution are the *mean* value, *variance*, *skewness* and *kurtosis*, defined in the Gumbel distribution as:

$$\mu = \alpha - \gamma\beta \tag{B.3}$$

$$\sigma^2 = \frac{\pi^2}{6}\beta^2 \tag{B.4}$$

$$\gamma_1 = -\frac{12\sqrt{6}\,\zeta(3)}{\pi^3} \tag{B.5}$$

$$\gamma_2 = \frac{12}{5} \tag{B.6}$$

where γ is the Euler-Mascheroni constant equal to 0.5772 and $\zeta(3)$ is the Apéry constant equal to 1.2020569.

Defining the random variable x as the *annual extreme value*, (B.3) and (B.4) return the annual mean and variance values. An extension of the extreme value distribution allows the calculation of these statistics referred to a general N-years extreme values following:

$$\mu_N = \mu + \beta \ln(N) \tag{B.7}$$

$$\sigma_N^2 = \sigma^2 \tag{B.8}$$

The Gumbel distribution is just the first of Fisher-Tippet extreme value distribution: the others are the Fréchet (or Type 2) and Weibull (or Type 3) distribution.

APPENDIX C

PRESSURE ON A MOVING PLATE

A small plane element placed on a Cartesian reference system is now considered. The element is loaded by a pressure field due to a wind action with wind speed $\boldsymbol{u}$ and the vertical velocity of the plate $\dot{\boldsymbol{h}}$: the resultant of the two velocities is called *effective wind speed* $\boldsymbol{u} - \dot{\boldsymbol{h}}$ with intensity *w* and direction $\boldsymbol{n}$. For simplicity, it is considered valid the approximation that reduce the degrees of freedom from 6 to 3: just the vertical displacement and the 2 rotation with respect the horizontal axis $\{\boldsymbol{h}, \boldsymbol{h}_{3,\alpha}\}$ for the static part; besides the dynamic variables of the position are also considered $\{\dot{\boldsymbol{h}}, \ddot{\boldsymbol{h}}\}$.

In this context two frames are taken into account (Figure C.1): the global frame $\{\boldsymbol{e^1}, \boldsymbol{e^2}, \boldsymbol{e^3}\}$ with $\boldsymbol{e^3}$ the vertical direction apposite to the gravity and the local frame system $\{\boldsymbol{t^1}, \boldsymbol{t^2}, \boldsymbol{t}\}$ with $\boldsymbol{t}$ the unit vector normal to the surface.

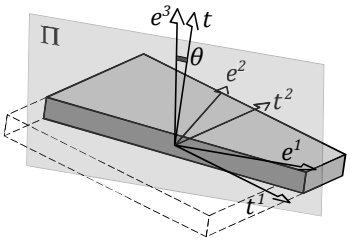

Π: slice plane including $\boldsymbol{e}^3$ and $\boldsymbol{t}$

angles between the unit vectors:
$\widehat{\boldsymbol{e^1 t^1}} = \theta_1$
$\widehat{\boldsymbol{e^2 t^2}} = \theta_2$
$\widehat{\boldsymbol{e^3 t}} = \theta$

Figure C.1: Reference systems considered in the element.

Imaging that the wind blows from a general direction $\boldsymbol{n}$, it is possible to write the wind velocity $\boldsymbol{u}$ with reference to the global frame as the simple decomposition into the three directions:

$$\boldsymbol{u} = u_1 \boldsymbol{e}^1 + u_2 \boldsymbol{e}^2 + u_3 \boldsymbol{e}^3 \tag{C.1}$$

Moreover, it is also possible coupling the two horizontal components u_1 and u_2 by placing on the plane with basis $\boldsymbol{e}^{12}, \boldsymbol{e}^3$ (Figure C.2).

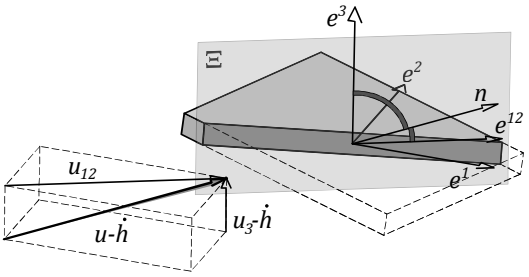

Ξ: slice plane including $\boldsymbol{e}^3$ and $\boldsymbol{n}$

$$\boldsymbol{u} = u_{12}\boldsymbol{e}^{12} + u_3\boldsymbol{e}^3$$
$$u_{12} = \sqrt{u_1^2 + u_2^2}$$
$$\boldsymbol{e}^{12} = \frac{u_1}{u_{12}}\boldsymbol{e}^1 + \frac{u_2}{u_{12}}\boldsymbol{e}^2$$

Figure C.2: Wind speed approaching the surface.

The resulting pressure force of the wind action $\boldsymbol{F}(\boldsymbol{u} - \dot{\boldsymbol{h}})$ can be projected into the orthogonal and parallel the plate directions (Figure C.3). In this case the force is thought lying on the Γ surface that includes the unit vectors $\boldsymbol{s}, \boldsymbol{t}$ which are the orthogonal basis and $\boldsymbol{n}$ the effective wind direction.

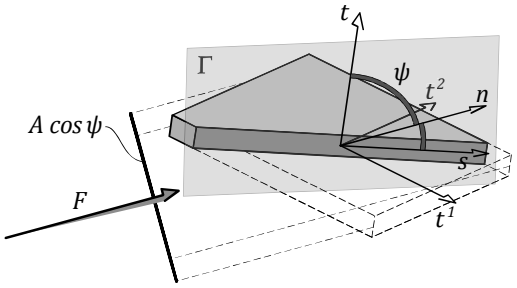

Γ: slice plane including $\boldsymbol{t}$ and $\boldsymbol{n}$

angle between the unit vectors:
$\widehat{\boldsymbol{t}\,\boldsymbol{n}} = \psi$

A: plate's area

Figure C.3: Velocity pressure resultant on the surface.

In order to compute the resultant pressure on the plate, a visual simplification of the 3D sketches can be done by align the Π and Γ surfaces on more simple 2D sketches (Figure C.4), having in mind that the definition of the directions and the relatives angles remain the previous and they have to be treated with the vector algebra.

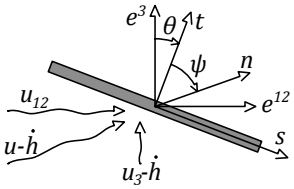

angles between the unit vectors:
$\boldsymbol{e}^{12} \cdot \boldsymbol{t} = \sin\theta$
$\boldsymbol{e}^3 \cdot \boldsymbol{t} = \cos\theta$
$\boldsymbol{n} \cdot \boldsymbol{t} = \cos\psi$

Figure C.4: View of the Γ slice section.

The *effective wind speed* $\boldsymbol{u} - \dot{\boldsymbol{h}}$ is now computed as:

$$\boldsymbol{u} - \dot{\boldsymbol{h}} = u_{12}\boldsymbol{e}^{12} + \left(u_3 - \dot{h}\right)\boldsymbol{e}^3 \tag{C.2}$$

$$w = \left\|\boldsymbol{u} - \dot{\boldsymbol{h}}\right\| = \sqrt{u_{12}^2 + \left(u_3 - \dot{h}\right)^2} \tag{C.3}$$

$$\boldsymbol{n} = \frac{u_{12}}{w}\boldsymbol{e}^{12} + \frac{u_3 - \dot{h}}{w}\boldsymbol{e}^3 \tag{C.4}$$

The velocity pressure of the flux due to the effective wind speed is q and acts on the projection of the plate surface with area A along the direction $\boldsymbol{n}$ (Figure C.5).

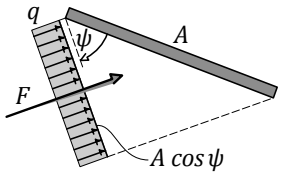

kinetic pressure: $q = \frac{1}{2}\rho w^2$

projected area: $A\cos\psi$

Figure C.5: Velocity pressure acting on the surface's projection.

$$F = q \cdot A(\boldsymbol{n} \cdot \boldsymbol{t}) = qA\cos\psi \tag{C.5}$$

It is now possible to split the resultant force into the *along the plane* and *orthogonal the plane* direction (Figure C.6). As a first assumption it is not considered any friction on the plate, hence the parallel component of the aerodynamic force is neglected when computing the resultant force on the plate.

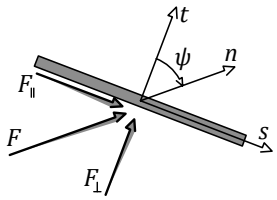

$F\,\boldsymbol{n} = F_{\parallel}\boldsymbol{s} + F_{\perp}\boldsymbol{t}$
$F_{\parallel} = F\sin\psi = F\ (\boldsymbol{n} \cdot \boldsymbol{s}) \rightarrow$ negl.
$F_{\perp} = F\cos\psi = F\ (\boldsymbol{n} \cdot \boldsymbol{t})$

Figure C.6: Pressure resultant decomposition.

Finally the resultant force acting on the plate which corresponds to the aerodynamic pressure is written as:

$$F_{\perp} = \frac{1}{2}\rho w^2 \, A \, (\boldsymbol{n} \cdot \boldsymbol{t})^2 \tag{C.6}$$

$$p = \frac{F_{\perp}}{A} = \frac{1}{2}\rho w^2 \, (\boldsymbol{n} \cdot \boldsymbol{t})^2 \tag{C.7}$$

$$\begin{aligned} p = \frac{1}{2}\rho w^2 \left[\frac{u_{12}}{w}(\boldsymbol{e}^{12} \cdot \boldsymbol{t}) + \frac{u_3 - \dot{h}}{w}(\boldsymbol{e}^{3} \cdot \boldsymbol{t})\right]^2 \\ = \frac{1}{2}\rho w^2 \left[\frac{u_{12}}{w}\sin\theta + \frac{u_3 - \dot{h}}{w}\cos\theta\right]^2 \end{aligned} \tag{C.8}$$

$$\begin{aligned} p = \frac{1}{2}\rho u_{12}^2 \sin^2\theta + \frac{1}{2}\rho 2 u_{12}\left(u_3 - \dot{h}\right)\sin\theta\cos\theta \\ + \frac{1}{2}\rho\left(u_3 - \dot{h}\right)^2 \cos^2\theta \end{aligned} \tag{C.9}$$

Following the Maclaurin Series of the trigonometric functions around the position $\theta \to 0$:

$$\sin^2\theta = \theta^2 - \frac{1}{3}\theta^4 + \frac{2}{45}\theta^6 + \cdots \tag{C.10}$$

$$\cos^2\theta = 1 - \theta^2 + \frac{1}{3}\theta^4 - \frac{2}{45}\theta^6 + \cdots \tag{C.11}$$

$$\sin\theta\cos\theta = \theta - \frac{2}{3}\theta^3 + \frac{2}{15}\theta^5 + \cdots \tag{C.12}$$

it is possible rewrite (C.9) as:

$$p \simeq \frac{1}{2}\rho u_{12}^2 \theta^2 + \frac{1}{2}\rho 2 u_{12}\left(u_3 - \dot{h}\right)\theta + \frac{1}{2}\rho\left(u_3 - \dot{h}\right)^2(1 - \theta^2) \tag{C.13}$$

$$p \simeq \frac{1}{2}\rho u_{12}^2 \left(\theta + 2\frac{u_3 - \dot{h}}{u_{12}}\right)\theta + \frac{1}{2}\rho\left(u_3 - \dot{h}\right)^2(1 - \theta^2) \tag{C.14}$$

$$\begin{aligned} p \simeq \quad & \frac{1}{2}\rho u_{12}^2\,\theta \cdot \theta \quad + \quad \frac{1}{2}\rho u_{12}^2\, 2\frac{u_3 - \dot{h}}{u_{12}} \cdot \theta \\ & + \quad \frac{1}{2}\rho\left(u_3 - \dot{h}\right)^2 \quad - \quad \frac{1}{2}\rho\left(u_3 - \dot{h}\right)^2\theta^2 \end{aligned} \tag{C.15}$$

Further approximation induces to neglect the terms depending on θ^2, moreover assuming that in normal condition the wind speed has only the horizontal component, that means $u_3 = 0$, the approximated pressure is:

$$p \simeq \frac{1}{2}\rho\dot{h}^2 - \rho u_{12}\dot{h}\theta \tag{C.16}$$

REFERENCES

Afassociados. “Empreitada de Construção do Novo Estádio de Braga.” Techinical Report, 2001.

Ahmad, S., B.M. Irons, and O.C. Zienkiewicz. “Analysis of thick and thin shell structures by curved finite elements.” *International Journal for Numerical Methods in Engineering* 2 (1970): 419-451.

American National Standard A58.1. “Minimum design loads for buildings and other structures.” New York: American National Standards Institute, Inc., 1982.

Argyris, J., and H.P. Mlejnek. *Dynamics of structures.* Amsterdam: North-Holland, 1991.

Armitt, J. “Eigenvector analysis of pressure fluctuation on the West Burton instrumented cooling tower.” *Central Electricity Research Laboratories (UK)*, 1968.

ASCE 7-02, Standard. “Minimum design loads for buildings and other structures.” New York: American Society of Civil Engineers, 2002.

Bachman, H., and W.J. Ammann. *Vibration in structures induced by man and Machines.* Zürich: IABSE – AIPC – IVBH, 1987.

Bachman, H., W.J. Ammann, F. Deischl, and J. Eisenmann. *Vibration problems in structures: practical guidelines.* Basel, 1994.

Baker, J.W., and C.A. Cornell. *Uncertainty specification and propagation for loss estimation using FOSM methods.* PEER Report 2003/07, Berkeley: University of California, 2003.

Bathe, K.J. *Finite element procedures.* New Jersey: Prentice-Hall, 1996.

Batoz, J.L. “An explicit formulation for an efficient triangular plate-bending element.” *International Journal for Numerical Methods in Engineering* 15 (1982): 1771-1812.

Batoz, J.L., K.J. Bathe, and L.W. Ho. “A study of three-node triangular plate bending elements.” *International Journal for Numerical Methods in Engineering* 15 (1980): 1771-1812.

Bazeley, G.P., Y.K. Cheung, B.M. Irons, and O.C. Zienkiewicz. “Triangular elements in plate bending - conforming and non-conforming solutions.” *Proc. Conf. on Matrix Methods in Structural Mechanics, WPAFB.* Ohio, 1965. 547-576.

Belytschko, T., W.K Liu, and B. Moran. *Nonlinear Finite Elements for Continua and Structures.* New York: Wiley, 2000.

Bergan, P.G., and C.A. Felippa. “A triangular membrane element with rotational degrees of freedom.” *Computer Methods in Applied Mechanics and Engineering* 50 (1985): 25-69.

Bergan, P.G., and M.K. Nygård. “Finite elements with increased freedom in choosing shape functions.” *International Journal for Numerical Methods in Engineering* 20 (1984): 643-664.

Best, R.J., and J.D. Holmes. “Use of eigenvalues in the covariance integration method for determination of wind load effects.” *Journal of Wind Engineering and Industrial Aerodynamics* 13 (1983): 359-370.

Billah, K., and R. Scanlan. “Resonance, Tacoma Narrows bridge failure, and undergraduate physics textbooks.” *American Journal of Physics* 59, no. 2 (1991): 118-124.

Brincker, R., P. Andersen, and N. Moller. “An indicator for separation of structural and harmonic modes in output-only modal testing.” *IMAC 18.* San Antonio, Texas, 2000. 1649-1654.

BS 6399-2, Standard. “Loading for buildings. Part 2: Code of practice for wind loads.” British Standard Institution, 1997.

Burton, M.D., K.C.S. Kwok, P.A. Hitchcock, and R.O. Denoon. “Frequency dependence of human response to wind-induced building motion.” *Journal of Structural Engineering, ASCE* 132, no. 2 (2006): 296-303.

Caetano, E., A. Cunha, and F. Magalhães. “Numerical and experimental studies of Braga sports stadium suspended roof.” *Journal of Structure and Infrastructure Engineering*, 2008.

Caetano, E., and A. Cunha. “Numerical modeling of the structural behavior of the new Braga Stadium roof.” Technical Report FEUP/VIBEST (in Portuguese), 2001.

Castellari, A., M. Lazzari, and A. Saetta. *Effect of geometric non linearity on the natualr frequency evaluation of prestressed cable system.* Internal report, DIC, University of Padua, 2004.

CIMNE, Barcelona. *International Center for Numerical Methods in Engineering.* http://www.cimne.upc.es/cdl1/itshome/start.aspx.

Clough, J., and R.W. Penzien. *Dynamics of structures.* New York: McGraw Hill, 1993.

CNR-DT_207-08. “Guidelines on Actions end Effects of Wind on Structures.” C.N.R. (Italian National Research Council) (Italian version), 2008.

Cole, H.A. “On-line failure detection and damping measurement of aerospace structures by random decrement signatures.” NASA CR-2205, 1973.

—. “On-the-line Analysis of Random Vibrations.” *Structural Dynamics and Material Conference.* Palm Springs: AIAA, 1968.

Coleman, H.W., and S. Stern. “Uncertainties and CFD Validation.” Edited by ASME. *Journal of Fluids Engineering* 119 (1997): 795-803.

Cook, R.D. “Improved two-dimensional finite element.” Edited by ASCE. *Journal of the Structural Division*, 1974: 1851-1863.

Cosentino, N., and M. Majowiecki. “Analysis and mitigation of the wind induced response of large span suspended roofs: the case of the new Braga Stadium.” *IN-VENTO.* Reggio Calabria, Italy, 2004.

Cosserat, E., and F. Cosserat. “Théorie des corps déformables.” In *Traité de Physique*, 953-1173. Paris, 1909.

CRED. *Thirty Years of Natural Disasters 1974-2003: The Numbers.* Centre for Research on the Epidemiology of Disasters, UCL Presses, 2004.

Crisfield, M.A. *Non-Linear Finite Element Analysis of Solids and Structures. Volume 1: Essentials.* John Wiley and Sons, 1991.

—. *Non-linear finite element analysis of solids and structures. Volume 2: Advanced topics.* John Wiley and Sons, 1997.

Dadvand, P. “A framework for developing finite element codes for multi-disciplinary applications.” *doctoral thesis.* UPC Barcelona, 2007.

Davenport, A.G. «How can we simplify and generalize wind loads?» *Journal of Wind Engineering and Industrial Aerodynamics* 54/55 (1995): 657-669.

Davenport, A.G. “Note on the distribution of the largest value of a random function with application to gust loading.” *Proceeding of the Institution Civil Engineers* 24 (1964): 187–196.

Davenport, A.G. “Past, present and future of wind engineering.” *Journal of Wind Engineering and In-dustrial Aerodynamics* 90 (2002): 1371-1380.

—. “The relationship of wind structure to wind loading.” *Symposium on wind effects on buildings and structures.* London, 1965. 53-102.

Dyrbye, C., and S.O. Hansen. *Wind Loads on Structures.* John Wiley and Sons, 1996.

EM-DAT. “Emergency Events Database.” http://www.emdat.be/.

Eurocode_1-1-4. “Action on structures. General actions – Wind actions.” C.E.N. (European Committee for Standardization), 2005.

Faber, M.H. *Risk and safety in civil engineering – Lecture Notes.* ETH Zürich, 2007.

—. *Statistics and probability theory – Lecture Notes.* ETH Zürich, 2006.

Faber, M.H., and M.G. Stewart. “Risk assessment for civil engineering facilities: critical overview and discussion.” *Reliability Engineering & System Safety* 80 (2003): 173-184.

Felippa, C.A. “A study of optimal membrane triangles with drilling freedoms.” *Computer Methods in Applied Mechanics and Engineering* 192 (2003): 2125-2168.

—. “Recent advances in finite element templates.” *Computational Mechanics for the Twenty-First Century.* Edinburgh: Saxe-Coburn Publication, 2000. 71-98.

Felippa, C.A., and B. Haugen. “A unified formulation of small-strain corotational finite elements: I. Theory.” *Computer Methods in Applied Mechanics and Engineering* 194 (2005): 2285-2335.

Felippa, C.A., and P.G. Bergan. “A triangular bending element based on an energy-orthogonal free formulation.” *Computer Methods in Applied Mechanics and Engineering* 61 (1987): 129-160.

FIP. *FIP Industriale.* http://www.fip-group.it/fip_ind/prodotti.html.

Franke, J., et al. “Recommendations on the use of CFD in wind engineering.” *Proceedings of the International Conference on Urban Wind Engineering and Building Aerodynamics.* Saint-Genesius-Rode, Belgium, 2004.

Fung, Y.C., and E.E. Sechler. *Thin-shell structures: theory, experiments and design.* Englewood Cliffs, N.J: Prentice-Hall, 1974.

Furtado, R., C. Quinaz, and R. Bastos. “New Braga Municipal Stadium, Braga.” *AFAssociados Structural Engineer Internationl*, 2005.

Gallagher, R.H. *Finite Element Analysis: Fundamentals.* Englewood Cliffs, N.J.: Prentice-Hall, 1975.

Gaul, L., and R. Nitsche. “The role of friction in mechanical joints.” *Applied Mechanics Reviews* 54 (2001): 93-105.

Gazetas, G., and G. Mylonakis. “Seismic soil-structure interaction: new evidence and emerging issues.” *Geotechnical Earthquake Engineering and Soil Dynamics, ASCE* (ASCE) 2 (1998): 1119-1174.

Gilliam, X., J.P. Dunyak, D.A. Smith, e F. Wu. «Using projection pursuit and proper orthogonal decomposition to identify independent flow mechanisms.» *Journal of Wind Engineering and Industrial Aerodynamics* 92 (2004): 53-69.

Grossi, P., and H. Kunreuther. *Catastrophe modelling: a new approach to managing risk.* Springer, 2005.

He, J., and Z. Fu. *Modal Analysis.* London: Butterworth-Heinemann Press, 2001.

Holmes, J.D. “Analysis and synthesis of pressure fluctuation on bluff bodies using eigenvectors.” *Journal of Wind Engineering and Industrial Aerodynamics* 33 (1990): 219-230.

—. *Wind Loading of Structures.* London: Spon Press, 2001.

Holmes, J.D., R. Sankaran, K.C.S. Kwok, and M.J. Syme. “Eigenvectors modes of fluctuating pressure on low-rise building models.” *Journal of Wind Engineering and Industrial Aerodynamics* 69-71 (1997): 687-707.

Huerta, C.I., J.M. Roesset, and K.H. Stokoe. “Evaluation of the random decrement method for in-situ soil properties estimation.” *Proceedings of second international symposium on*

the effects of surface geology on seismic motion, vol. II. Recent progress and new horizon on ESG study. Yokohama, 1998. 749-756.

Hughes, T.J.R., and W.K. Liu. "Nonlinear finite element analysis of shells: Part I. Three-dimensional shells." *Computer Methods in Applied Mechanics and Engineering* 26 (1981): 331-362.

Inaudi, J.A., and J.M. Kelly. "Linear hysteretic damping and Hilbert transform." *Journal of Engineering Mechanics* 121 (1995): 626-632.

Jeary, A.P. "Establishing non-linear damping characteristics of structures from non-stationary response time-histories." *Structural Engineer* 70 (1992): 61-66.

Jolliffe, I.T. *Principal Component Analysis.* NY: Springer, 2002.

Jonkman, S.N. "Global Perspectives on Loss of Human Life Caused by Floods." *Natural Hazards* 34 (2005): 151-175.

Joseph, K.T., and K.S. Rao. "A fast algorithm for triangular plate bending element." *International Journal for Numerical Methods in Engineering* 14 (1979): 1100-1104.

Kareem, A., and J.E. Cermak. "Pressure fluctuation on a square building model in boundary-layer flows." *Journal of Wind Engineering and Industrial Aerodynamics* 16 (1984): 17-41.

Kareem, A., and K. Gurley. "Damping in structures: its evaluation and treatment of uncertainty." *Journal of Wind Engineering & Industrial Aerodynamics* 59 (1996): 131-157.

Khandury, A.C., and G.C. Morrow. "Vulnerability of buildings to windstorms and insur-ance loss estimation." *Journal of Wind Engineering and Industrial Aerodynamics* 91 (2003): 455-467.

Khosravi, P, R. Ganesan, and R. Sedaghati. "Corotational non-linear analysis of thin plates and shells using a new shell element." *International Journal for Numerical Methods in Engineering* 69 (2007): 859-885.

Korhonen, J., I. Savolainen, and M. Ohlstrom. "Applications of the industrial ecology concept in a research project: Technology and Climate Change (CLIMTECH) Research in Finland." *Journal of Cleaner Production* 12 (2004): 1087-1097.

Kotz, S., and S. Nadarajah. *Extreme Value Distributions. Theory and Applications.* London: Imperial College Press, 2000.

KRATOS, Multi-Physics. *Free multiphysic finite element method C++ open source code.* http://kratos.cimne.upc.es/kratoswiki/index.php/Main_Page.

Ku, C.J., J.E. Cermak, and L.S. Chou. "Random decrement based method for modal parameter identification of a dynamic system using acceleration responses." *Journal of Wind Engineering and Industrial Aerodynamics* 95 (2007): 389-410.

Kwan, A.S.K. "A simple technique for calculating natural frequencies of geometrical non-linear prestressed cable structures." *Computers and Structures* 74 (2000): 41-50.

Larese, A., R. Rossi, E. Oñate, and S.R. Idelsohn. "Validation of the Particle Finite Element Method (PFEM) for simulation of free surface flows." *Engineering Computations* 25 (2008): 385-425.

Lee, B.E. "The effects of turbulence on the surface pressure field of a square prism." *Journal of Fluid Mechanics* 69 (1975): 17-41.

Leicester, R.H. "A risk model for cyclone damage to dwellings." *in Proceeding of the 3rd International Conference on Structural Safety and Reliability.* Trondheim, Norway, 1981. 761-771.

Letchford, C.W., R.O. Denoon, G. Johnson, and A. Mallman. "Dynamic characteristics of cantilever grandstand roofs." *Engineering Structures* 24 (2002): 1085-1090.

Li, Q.S., D.K. Liu, J.Q. Fang, A.P. Jeary, and C.K. Wong. "Damping in buildings: its neural network model and AR model." *Engineering Structures* 22 (2000): 1216-1223.

Littler, J.D. "An assessment of some of the different methods for estimating damping from full-scale testing." *Journal of Wind Engineering & Industrial Aerodynamics* 57 (1995): 179-189.

Ljung, L. *System identification: Theory for the user.* Englewood Cliffs, N.J.: Prentice-Hall, 1987.

Loève, M. *Probability Theory: Foundations. Random Sequences.* D. Van Nostrand, 1955.

Magalhães, F., E. Caetano, e A. Cunha. «Operational modal analysis of the Braga Sports Stadium suspended roof.» *International Modal Analysis Conference, IMAC-XXIV.* St. Louis, Missuri, USA, 2006.

Majowiecky, M., M. Marini, and N. Cosentino. *New Braga Stadium roof. Experimental investigation for structural dynamic characterisation.* Technical Report, Studio Tecnico Majowicky, 2004.

Maldonado, P., and M. Márquez. “Renewable energies: An energy option for sustainable development.” *Renewable Energy* 9 (1996): 1072-1075.

Militello, C., and C.A. Felippa. “The first ANDES elements: 9-dof plate bending triangle.” *Computer Methods in Applied Mechanics and Engineering* 93 (1991): 217-246.

Newmark, N.M. “A method of computation for structural dynamics.” *Journal of the Engineering Mechanics Division* (ASCE) 85 (1959): 67-94.

Olivato, G., L. Baro, M. Lazzari, and A. Saetta. “Global approach for wind load response analyses: POD techniques.” *International Conference IABSE-fib.* Dubrovnik, Croatia, 2010.

Oñate, E. *Cálculo de estructuras por el Método de Elementos Finitos. Análisis estático lineal.* Barcelona, 1995.

Oñate, E., and F.G. Flores. “Advances in the formulation of the rotation-free basic shell triangle.” *Computer Methods in Applied Mechanic and Engineering* 194 (2005): 2406-2443.

Park, K.C., and G.M. Stanley. “A curved C0 shell element based on assumed natural-coordinate strains.” *Journal of Applied Mechanics* 53 (1986): 278-290.

Paulotto, C., M. Ciampoli, and G. Augusti. "Some proposals for a first step towards a Performance Based Wind Engineering." *IFED International Forum in Engineering Decision Making: First Forum.* Stoos, Switzerland, 2004.

Pearson, K. “On lines and planes of closest fit to systems of points in space.” *Phlosophical Magazine2* 6 (1901): 559-572.

Pekcan, G., G.B. Mander, and S.S. Chen. “Fundamental considerations for the design of non-linear viscous dampers.” *Earthquake Engineering & Structural Dynamics* 28 (1999): 1405-1425.

Peterson, B. *Identification and damage detection in civil engineering.* Belgium: PhD thesis, Katholieke Universiteit Leuven, 2000.

Pian, T., and P. Tong. "Basis of finite element methods for solid continua." *International Journal for Numerical Methods in Engineering* 1 (1969): 3-28.

Piegl, L., and W. Tiller. *The NURBS book.* 2nd. Springer, 1997.

Pliefke, T., S.T. Sperbeck, and M. Urban. “The probabilistic risk management chain - general concept and definitions.” Internal Discussion Paper, International Graduate College 802, 2006.

Pliefke, T., S.T. Sperbeck, M. Urban, U. Peil, and H. Budelmann. “A standardized methodology for managing disaster risk – An attempt to remove ambiguity.” *5th International Probabilistic Workshop.* Ghent, Belgium, 2007.

Robinson, J. “Element evaluation. A set of assessment points and standard tests.” *Proc. F.E.M. in the Commercial Environment.* 1978. 217-248.

Rossi, R., M. Lazzari, and R. Vitaliani. “Wind field simulation for structural engineering purposes.” *International Journal for Numerical Method in Engineering* 61 (2004): 738-763.

RWDI. *Consulting Engineers.* http://www.rwdi.com/.

RWDI. “Wind tunnel study of a roof wind pressures, Braga Stadium.” Internal report 01-327, 2001.

Schlager, N. *When Technology Fails: significant technological disasters, accidents, and failures of the twentieth century.* Thomson Gale, 1994.

Shaw, P.J.A. *Multivariate statistics for the Environmental Sciences.* Hodder-Arnold, 2003.

Shinozuka, M., and C.M. Jan. “Digital simulation of random processes.” *Journal of Sound and Vibration* 25 (1972): 111-128.

Shlens, J. «A tutorial on Principal Component Analysis.» *datet December 10, 2005; Version 2*, 2005: http://www.snl.salk.edu/~shlens/pub/notes/pca.pdf.

Simiu, E., and R.H. Scanlan. *Wind effects on structures.* New York: John Wiley and Sons, Inc., 1996.

Simo, J.C., and D.D. Fox. “On a stress resultant geometrically exact shell model. Part I: Formulation and optimal parametrization.” *Computer Methods in Applied Mechanics and Engineering* 72 (1989): 267-304.

Simo, J.C., D.D. Fox, and M.S. Rifai. “On a stress resultant geometrically exact shell model. Part II: The linear theory; Computational aspects.” *Computer Methods in Applied Mechanics and Engineering* 73 (1989): 53-92.

Simo, J.C., D.D. Fox, and M.S. Rifai. “On a stress resultant geometrically exact shell model. Part III: Computational aspects of the nonlinear theory.” *Computer Methods in Applied Mechanics and Engineering* 79 (1990): 21-70.

Solari, G. “A generalized definition of gust factor.” *Journal of Wind Engineering and Industrial Aerodynamics* 36 (1990): 539-548.

Stathopoulos, T. “Wind and Comfort.” *Proceeding of the 5th European and African Conference on Wind Engineering.* Florence, Italy, 2009. K67-K82.

Stoltman, J.P., J. Lidstone, and L.M. Dechano. *International Perspectives on Natural Disasters: Occurrence, Mitigation, and Consequences.* Springer, 2008.

Tamura, Y., S. Suganuma, H. Kikuchi, and K. Hibi. “Proper orthogonal decomposition on random wind pressure field.” *Journal of Fluid and Structures* 13 (1999): 1069-1095.

Tensoteci. *Redaelli Tensoteci Engineering.* http://www.redaellitensoteci.com/index.asp.

Vandiver, J.K., R.B. Dunwoody, R.B. Campbell, and M.F. Cook. “A mathematical basis for the random decrement vibration signature analysis technique.” *Journal of Mechanical Design*, 1982: 307-331.

Vickery, B.J. «Wind loads on the Olympic Stadium: Orthogonal Decomposition and Dynamic (Resonant) Effects.» *Report BLWT-SS28A*, 1993.

Vickery, B.J., and R.I Basu. “Across-wind vibrations of structures of circular cross-section. Part 1: Development of a two dimensional model for two dimensional conditions.” *Journal of Wind Engineering and Industrial Aerodynamic* 12 (1983): 49-73.

Von Kármán, T. “Progress in the statistical theory of turbulence.” *Proceedings of the National Academy of Sciences* 34 (1948): 530-539.

Wikipedia. *Principal component analysis - Wikipedia, the free encyclopedia.* PCA. http://en.wikipedia.org/wiki/Principal_component_analysis.

Woo, G. *The mathematics of natural catastrophes.* London: Imperial College Press, 1999.

Yuan, H. *Numerical Assessments of Cracks in Elastic-Plastic Materials.* Kindle Edition, 2002.

Zienkiewicz, O.C., and R.L. Taylor. *The finite element method for solid and structural mechanics.* 6th. Butterworth-Heinemann, 2005.

Zivanovic, S., A. Pavic, and P. Reynolds. “Vibration serviceability of footbridges under human-induced excitation: a literature review.” *Journal of Sound and Vibration* 279 (2005): 1-74.